# Development of a new cathode material for intermediate temperature solid oxide fuel cells

Seonhye park

Department of Energy Engineering

Graduate School of UNIST

2014

# Development of a new cathode material for intermediate temperature solid oxide fuel cells

A thesis
Submitted to the Graduate School of UNIST
in partial fulfillment of the
requirements for the degree of
Master of Science

Seonhye park

01.27.2014
Approved by

Major Advisor
Prof. Guntae Kim

# Development of a new cathode material for intermediate temperature solid oxide fuel cells

Seonhye park

This certifies that the thesis of Seonhye Park is approved.

01.27.2014

Signature

_____

Thesis Supervisor: Guntae Kim

Signature

_____

Soojin Park

Signature

_____

Jin Young Kim

# Abstract

Solid oxide fuel cells (SOFCs) are electrochemical energy conversion devices that directly convert the chemical energy to electricity with high conversion efficiency and no pollution emissions. Despite their excellent advantages, the high operating temperature of a conventional SOFC leads to some challenges, such as material compatibility challenges and high costs. As a resolution, intermediate temperature (IT) SOFCs have been introduced, operating from 500 to 700 $^{o}$C. The main obstacles toward IT-SOFC commercialization, however, are poor oxide-ion conductivity of an electrolyte and low catalytic activity of a conventional cathode, stemming from the reduction of operating temperature. Therefore, considerable efforts have been dedicated in the two areas for the successful performance of IT-SOFCs: improving the ionic conductivity of electrolytes and reducing the polarization resistance of cathodes.

This thesis mainly focuses on the latter one with the aim to develop a novel cathode material with high performance for IT-SOFC applications. The systematic studies for achieving high electrochemical performances and stable thermal properties are presented in the thesis as following,

1. Investigate strontium effects on the electrochemical performances for a simple perovskite oxide, $Pr_{1-x}Sr_xCoO_{3-\delta}$ ($x$ = 0.1, 0.3, 0.5, and 0.7).
2. Compare the oxygen transport kinetics between simple and double perovskite oxides in $PrBa_{1-x}Sr_xCo_2O_{5+\delta}$ ($x$ = 0, 0.25, 0.5, 0.75, and 1.0) systems.
3. Study on sintering and composite effects in for $PrBa_{0.5}Sr_{0.5}Co_{1.5}Fe_{0.5}O_{5+\delta}$ cathode material for IT-SOFCs.
4. Stabilize thermal expansion of Co-based cathode material by Cu-doping in $PrBa_{0.5}Sr_{0.5}Co_2O_{5+\delta}$.

# Table of Contents

**3. Results**

**List of figures**

**Fig. 15.** XRD pattern, calculated profile, peak position and the difference between observed and calculated profiles for the $PrBa_{0.5}Sr_{0.5}Co_2O_{5+\delta}$.

**Fig. 16.** X-ray diffraction patterns of $PrBa_{1-x}Sr_xCo_2O_{5+\delta}$-GDC($x$ = 0, 0.25, 0.5, 0.75, and 1.0) sintered at 1000°C for 4h.

**Fig. 17.** The cross sectional SEM images $PrBa_{1-x}Sr_xCo_2O_{5+\delta}$-GDC cathodes/GDC electrolyte interface: (a) $x$ = 0, (b) $x$ = 0.25, (c) $x$ = 0.5, (d) $x$ = 0.75, (e) $x$ = 1.0, and (f) the cross-section of a single cell with approximately 20μm-thick GDC membrane.

**Fig. 18.** Thermogravimetric data of $PrBa_{1-x}Sr_xCo_2O_{5+\delta}$ ($x$ = 0, 0.25, 0.5, 0.75, and 1.0) showing the variation of oxygen content as a function of temperature in air.

**Fig. 19.** Electrical conductivities of $PrBa_{1-x}Sr_xCo_2O_{5+\delta}$ ($x$ = 0, 0.25, 0.5, 0.75, and 1.0) in air as a function of temperature.

**Fig. 20.** (a) Impedance spectra of $PrBa_{1-x}Sr_xCo_2O_{5+\delta}$ ($x$ = 0, 0.25, 0.5, 0.75, and 1.0)-GDC composite cathodes on GDC symmetrical cells measured at 600 °C under OCV. (b) Temperature dependence of the $PrBa_{1-x}Sr_xCo_2O_{5+\delta}$ ($x$ = 0, 0.25, 0.5, 0.75, and 1.0)-GDC composite cathodes polarization conductance by Arrhenius plots. (c) ASRs of $PrBa_{1-x}Sr_xCo_2O_{5+\delta}$ ($x$ = 0, 0.25, 0.5, 0.75, and 1.0)-GDC composite cathodes on GDC electrolyte in symmetrical cells measured at 600°C in air.

**Fig. 21.** *I-V* curves and corresponding power density curves of a single cell ($PrBa_{1-x}Sr_xCo_2O_{5+\delta}$-GDC /GDC/Ni-GDC) under various temperatures: (a) $x$ = 0, (b) $x$ = 0.25, (c) $x$ = 0.5, (d) $x$ = 0.75, and (e) $x$ = 1.0.

**Fig. 22.** X-ray diffraction patterns of (a) $PrBa_{0.5}Sr_{0.5}Co_{1.5}Fe_{0.5}O_{5+\delta}$ sintered at 1150 °C for 12 h, (b) $Ce_{0.9}Gd_{0.1}O_{1.95}$ (GDC) sintered at 1350 °C for 4 h, and $PrBa_{0.5}Sr_{0.5}Co_{1.5}Fe_{0.5}O_{5+\delta}$-GDC50 sintered at (c) 900 °C, (d) 950 °C, (e) 1000 °C, and (f) 1050 °C for 4h.

**Fig. 23.** Cross-sectional SEM images of $PrBa_{0.5}Sr_{0.5}Co_{1.5}Fe_{0.5}O_{5+\delta}$-GDC50 cathode/GDC electrolyte interface sintered at (a) 900 °C, (b) 950 °C, (c) 1000 °C, and (d) 1050 °C.

**Fig. 24.** (a) Impedance spectra of $PrBa_{0.5}Sr_{0.5}Co_{1.5}Fe_{0.5}O_{5+\delta}$-GDC50 composite cathodes on GDC symmetrical cells sintered at various temperatures and measured at 600 °C under OCV. (b) Temperature dependence of polarization resistance for $PrBa_{0.5}Sr_{0.5}Co_{1.5}Fe_{0.5}O_{5+\delta}$-GDC50 composite cathodes on GDC electrolyte sintered at various temperatures by Arrhenius plots.

**Fig. 25.** SEM images of $PrBa_{0.5}Sr_{0.5}Co_{2-x}Fe_xO_{5+\delta}$–GDC$x$/GDC/Ni-GDC: (a) $x$ = 0 wt%, (b) $x$ = 20 wt%, (c) $x$ = 40 wt%, (d) $x$ = 50 wt%, (e) $x$ = 60 wt%, and (f) the cross-section of a single cell with an approximately 15 μm-thick GDC membrane.

**Fig. 26.** (a) Experimental and simulated impedance plots of $PrBa_{0.5}Sr_{0.5}Co_{1.5}Fe_{0.5}O_{5+\delta}$–GDC$x$/GDC/Ni-GDC by the equivalent circuit shown as an inset. (b) Comparison of $R_2$ and $R_3$ for $PrBa_{0.5}Sr_{0.55}Co_{1.5}Fe_{0.5}O_{5+\delta}$–GDC$x$/GDC/Ni-GDC. (c) Temperature dependence of polarization

resistance for $PrBa_{0.5}Sr_{0.5}Co_{1.5}Fe_{0.5}O_{5+\delta}$-GDC$x$ ($x$ = 0, 20, 40, 50, and 60 wt%) composite cathodes on GDC electrolyte sintered at 950 $^{o}$C for 4 h by Arrhenius plots.

**Fig. 27.** *I-V* curves and corresponding power density curves of a single cell ($PrBa_{0.5}Sr_{0.5}Co_{1.5}Fe_{0.5}O_{5+\delta}$-GDC$x$/GDC/Ni-GDC) under various temperatures: (a) $x$ = 0, (b) $x$ = 20, (c) $x$ = 40, (d) $x$ = 50, and (e) $x$ = 60 wt%.

**Fig. 28.** XRD patterns, calculated profiles, peak positions and the differences between observed and calculated profiles for $PrBa_{0.5}Sr_{0.5}Co_{2-x}Cu_xO_{5+\delta}$ ($x$ = 0, 0.5, and 1.0) from 2 θ = 20 to 100 $^{o}$.

**Fig. 29.** In situ XRD patterns of $PrBa_{0.5}Sr_{0.5}Co_{2-x}Cu_xO_{5+\delta}$ for (a) $x$ = 0, (b) 0.5, and (c) 1.0 in the temperature range between room temperature and 800 $^{o}$C in air.

**Fig. 30.** X-ray diffraction patterns of $PrBa_{0.5}Sr_{0.5}Co_{2-x}Cu_xO_{5+\delta}$–GDC ($x$ = 0, 0.5, and 1.0) sintered at 1000 $^{o}$C for 4 h.

**Fig. 31.** The cross sectional SEM images $PrBa_{0.5}Sr_{0.5}Co_{2-x}Cu_xO_{5+\delta}$–GDC cathodes/GDC electrolyte interface: (a) $x$ = 0, (b) $x$ = 0.5, (c) $x$ = 1.0, and (d) the cross-section of a single cell with approximately 20μm-thick GDC membrane.

**Fig. 32.** Thermogravimetric analysis of $PrBa_{0.5}Sr_{0.5}Co_{2-x}Cu_xO_{5+\delta}$ ($x$ = 0, 0.5, and 1.0) showing the weigh change (%) as a function of temperature in air.

**Fig. 33.** Thermal expansion ($\Delta L/L_0$) curves of the $PrBa_{0.5}Sr_{0.5}Co_{2-x}Cu_xO_{5+\delta}$ ($x$ = 0, 0.5, and 1.0) specimens in the temperature range of 100 ~ 800 $^{o}$C.

**Fig. 34.** (a) Oxygen non-stoichiometry of $PrBa_{0.5}Sr_{0.5}Co_{2-x}Cu_xO_{5+\delta}$ ($x$ = 0, 0.5, and 1.0) as a function of $pO_2$ at 700 $^{o}$C. (b) The $pO_2$ dependence of the electrical conductivity of $PrBa_{0.5}Sr_{0.5}Co_{2-x}Cu_xO_{5+\delta}$ ($x$ = 0, 0.5, and 1.0) at 700 $^{o}$C.

**Fig. 39.** Electrical conductivities of $PrBa_{0.5}Sr_{0.5}Co_{2-x}Cu_xO_{5+\delta}$ ($x$ = 0, 0.5, and 1.0) in air as a function of temperature.

**Fig. 40.** (a) Impedance spectra of $PrBa_{0.5}Sr_{0.5}Co_{2-x}Cu_xO_{5+\delta}$ ($x$ = 0, 0.5, and 1.0)-GDC composite cathodes on GDC symmetrical cells measured at 600 $^{o}$C under OCV condition. (b) Temperature dependence of the $PrBa_{0.5}Sr_{0.5}Co_{2-x}Cu_xO_{5+\delta}$ ($x$ = 0, 0.5, and 1.0)-GDC composite cathodes polarization conductance by Arrhenius plots.

**Fig. 41.** *I-V* curves and corresponding power density curves of a single cell ($PrBa_{0.5}Sr_{0.5}Co_{2-x}Cu_xO_{5+\delta}$-GDC /GDC/Ni-GDC) under various temperatures: (a) $x$ = 0, (b) $x$ = 0.5, and (c) $x$ = 1.0.

**List of tables**

## 1. Introduction

This section includes the objectives and scope of the dissertation. From this starting point, the following subsections will provide a fundamental understanding of solid oxide fuel cell (SOFC) principles, what they are, how they work, what significant advantages and drawbacks they present, and as well as supporting theoretical background.

### 1.1. Research objectives

There are two main drawbacks of IT-SOFCs, stemming from the reduction of operating temperature, which include poor ionic conductivity of an electrolyte and low catalytic activity of a conventional cathode. This research mainly focuses on the latter one with the aim to explore a new cathode material to overcome the drawbacks of a conventional cathode for IT-SOFCs.

1. To develop a new cathode material for IT-SOFC to overcome the main drawback of low electro-catalytic activity of cathodes stemming from the reduction of operating temperature.
2. To compare the oxygen transport kinetics between simple and double perovskite oxide structures.
3. To identify the improved ORR mechanisms by two phase mixed conductor.
4. To figure out the tradeoffs between electrochemical performances and thermal expansion coefficient to alternate Co-rich material.

### 1.2. Scope of the thesis

Introduction section provides fundamentals for understanding how SOFCs work with state art of the art technologies. The three types of conductors, determining different oxygen reduction reaction mechanisms at cathodes, and theoretical fundamentals of charge and mass transport in mixed conductor that is one of the three conductors are described in this section.

In the experimental section, synthesis process for base materials and the experimental techniques to evaluate electrical conductivity, electrochemical performances, and redox behavior of the materials are provided.

The result sections are divided into four subsections, focusing on the actual output. The strontium effect on electrochemical performances in $ABO_3$-type simple perovskite of $Pr_{1-x}Sr_xCoO_{3-\delta}$ with various doping ratio of strontium as intermediate temperature (IT)-SOFC cathodes is reported in the first section of the results.

In the second section of the results, systematic investigation of strontium effect on ABB'O5-type layered perovskite of $PrBa_{1-x}Sr_xCo_2O_{5+\delta}$. $PrBa_{1-x}Sr_xCo_2O_{5+\delta}$ series are modified version of $Pr_{1-}$

$_{x}Sr_{x}CoO_{3-\delta}$ by substituting larger barium for strontium, which is the key factor to establish structural transition from simple to double perovskites. From the first and the second points, the differences in electrical transport properties between simple and double perovskites by varying partial substitution of strontium for each element are well compared.

The composite effects on oxygen reduction reaction (ORR) rate for $PrBa_{0.5}Sr_{0.5}Co_{1.5}Fe_{0.5}O_{5+\delta}$ with different amounts of ionic conducting phase GDC are reported based on the preliminary study to optimize the sintering process for this sample in the third section.

In the final section of the results, the tradeoff relationship between electrochemical performance and thermal expansion is identified by substituting Co by Cu in $PrBa_{1-x}Sr_{x}Co_{2}O_{5+\delta}$.

### 1.3. Solid oxide fuel cells

The developments of hydrogen technologies as an alternative energy source to fossil fuels have been accelerated. A fuel cell has been intensively investigated as a hydrogen-based renewable energy with the distinguishable benefits of no greenhouse gases or other pollutant. A fuel cell is a device which directly converts the chemical energy into electrical energy from continuous supplies of fuel and oxidant. The two streams are completely separated and produce electricity through electrochemical reactions similar to a conventional battery.[1] The details of the chemical reactions depend on the types of fuel cells, but in all types an electrically charged ion is transferred through an electrolyte that physically separates the fuel and oxidant streams. There are several types of fuel cells, differentiated from one another by their electrolyte,[2] and the details are provided in Table 1. Solid oxide fuel cells (SOFCs) are one of the fuel cells whose electrolyte is a hard and dense ceramic compound.[3] The subsequent subsections will provide more specifics of SOFC relevant properties.

**Table 1. Types of fuel cells** [2,4]

| | Alkaline Fuel Cell (AFC) | Phosphoric Acid Fuel Cell (PAFC) | Molten Carbonate Fuel Cell (MCFC) | Solid Oxide Fuel Cell (SOFC) | Polymer Electrolyte Membrane Fuel Cell (PEMFC) | Direct Methanol Fuel Cell (DMFC) |
|---|---|---|---|---|---|---|
| Electrolyte | Alkali | Phosphoric acid | Carbonate | Ceramic | Polymer membrane (ionomer) | Polymer membrane (ionomer) |
| Operational temperature ($^{o}$C) | 50 - 200 | 150 - 200 | 600 - 700 | 700 - 1000 | 50 - 100 | 50 - 110 |
| Efficiency | 45-60 % | 35-40 % | 45-60 % | 50-65 % | 45-60 % | 40 % |
| Fuel | Hydrogen | Hydrogen | Hydrogen or methane | Hydrogen or methane | Hydrogen | Methanol |
| Possible applications | Military, Space | Distributed generation | Electric utility, Distributed generation | Auxiliary power, Electric utility, Distributed generation, Transportation | Backup power, Portable power, Distributed generation, vehicles | Portable electronic systems, mobile consumer electronics |

### 1.3.1. Basic operating principles of SOFCs

SOFCs essentially consist of three components of cathode, electrolyte, and anode. The fuel electrode must be able to endure the highly reducing environment of the anode, while the air electrode must be able to withstand the highly oxidizing environment of the cathode under a high-operating temperature.[5] The hydrogen oxidation reaction (HOR) at the anode and the oxygen reduction reaction (ORR) at the cathode occur at the triple phase boundary (TPB) zone where the electrode (electronic phase), electrolyte (ionic phase), and gas phase (hydrogen, air) are in contact. Fig. 1 shows the general layout of SOFCs based on the hydrogen combustion reaction split into two electrochemical half reactions:[6]

$$H_2 \rightarrow 2H^+ + 2e^- \qquad (1.3.1.1)$$

$$\frac{1}{2}O_2 + 2H^+ + 2e^- \rightarrow H_2O \qquad (1.3.1.2)$$

$$H_2 + \frac{1}{2}O_2 \rightarrow H_2O \qquad (1.3.1.3)$$

A hydrogen gas is supplied to the anode where it may lose electrons and thereby form $H^+$ ions. These H+ ions are capable of diffusing across the electrolyte while the electrons flow through the external circuit. Note that the resulting current, as it is traditionally defined, is in the opposite direction the electron flow and the involved splitting of hydrogen molecules into protons and electrons can be speeded up by adopting a catalyst. A reaction of the form given in the equation (1.3.1.1) thus takes place at the anode, where suitable catalyst choices may make it proceed at an enhanced rate. Meanwhile, gaseous oxygen is supplied to the cathode, where a more complex reaction takes place with the net reaction shown in the equation (1.3.1.2). This reaction is likely built up by simpler reactions, which could involve oxygen reduction by electrons or hydrogen oxidation into $H^+$. Like in a biological material, SOFC may utilize membranes allowing $H^+$ ions to diffuse through, but not $H_2$ molecules. Oxygen and hydrogen, when mixed together with enough activation energy, have a natural tendency to react and form water because the Gibbs free energy of $H_2O$ is smaller than that of the summation of $H_2$ and $1/2O_2$ added together. The net reaction of the two half reactions thus becomes like the equation (1.3.1.3).

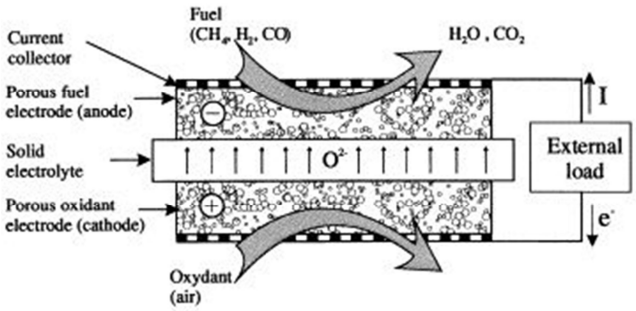


**Fig. 1. Schematic illustration of SOFC operation.**[7]

### 1.3.2. Advantages and drawbacks of SOFCs

The high operating temperature of the SOFCs ranging from 700 to 1000 $^{o}$C provides both challenges and advantages. The advantages include fuel flexibility, high efficiency, and the ability to employ cogeneration schemes using the high quality waste heat that is generated. The electrical efficiency of the SOFCs is about 50 – 60 %; in combined heat and power applications, efficiencies could reach up to 90 %.

Notwithstanding these advantages, the high operating temperature of conventional SOFCs (~ 1000 $^{o}$C) leads to some problems. It results in a slow start-up and requires the thermal shielding to protect personnel and retain heat, which may be acceptable for utility applications but not for transportation and small portable applications. The high operating temperatures also place the requirements stringent durability on materials.[8-10]

The development of low-cost materials with high durability at cell operating temperatures or the reduction of the operating temperature can be the key technical challenge facing this technology. In this respect, recent research has been aimed at developing intermediate temperature SOFCs (IT-SOFCs) operating from 500 to 700 $^{o}$C. IT-SOFC design could resolve most of the drawback stemming from the high-temperature operation while keeping the most significant benefits of the SOFCs.[11-13] The major obstacles of IT-SOFCs, however, also exist to the practical use of IT-SOFCs, including poor oxide-ion conductivity and inadequate catalytic activity of the conventional cathodes associated with the reduction of the operating temperature.[14]

## 1.4. Theoretical basics

### 1.4.1. The chemical thermodynamics of SOFCs

A SOFC is an electrochemical device which converts the Gibbs free enthalpy of the combustion reaction by a fuel and an oxidant gas directly into electricity. The first and the second law of thermodynamics allow the description of a reversible fuel cell, whereas in particular the second low governs the reversibility of the transport processes. The first law of the thermodynamics gives[15]

$$q + w = \Delta H \qquad (1.4.1)$$

The molar reaction enthalpy $\Delta H$ of the oxidation consists of work and heat energy. The second law of thermodynamics applied on reversible processes yields

$$\oint \Delta S = 0 \rightarrow q = q_{rev} = T\,\Delta S \qquad (1.4.2)$$

where the reversible heat exchange with the environment equalizes the generated reaction entropy, and we get

$$q_{rev} + w_{rev} = \Delta H \qquad (1.4.3)$$

The reaction entropy is a result of the different opportunities of the species to save thermal

energy between the absolute zero level of temperature and temperature level of the reactor.

Equations (1.4.2) and (1.4.3) give the molar reversible work, $w_{rev}$

$$w_{rev} = \Delta H - T\,\Delta S \qquad (1.4.4)$$

Using the ambient temperature as a reference for the calculation of the Gibbs free energy $\Delta G$, the reversible work of the reaction is equal to the Gibbs free energy of the reaction

$$w_{rev} = \Delta G = \Delta H - T\,\Delta S \qquad (1.4.5)$$

Based on the first and second laws of thermodynamics, the energy transfer from one form to another can be identified using thermodynamic potentials. From the first and the second laws of thermodynamics, an equation for internal energy ($U$) that is based on the variation of two independent variables of entropy $S$ and volume $V$ is derived where $p$ is the pressure and $T$ is temperature:[16]

$$dU = T\,dS - p\,dV \qquad (1.4.6)$$

Note that $T\,dS$ represents the reversible heat transfer and $p\,dV$ is the mechanical work. The following equations show how the dependent variables ($T$ and $p$) are related to variations in the independent variables ($S$ and $V$):

$$\left(\frac{dU}{dS}\right)_v = T \qquad (1.4.7)$$

$$\left(\frac{dU}{dV}\right)_s = -p \qquad (1.4.8)$$

A conversion of $U$ using a Legendre transform begins with defining the new thermodynamic potential $G\,(T, p)$ as follows:

$$G = U - \left(\frac{dU}{dS}\right)_v S - \left(\frac{dU}{dV}\right)_s V \qquad (1.4.9)$$

From (1.4.7) and (1.4.8), we obtain

$$G = U - TS + pV \qquad (1.4.10)$$

The variation of $G$ results in

$$dG = dU - TdS - SdT + pdV + Vdp \qquad (1.4.11)$$

Since $dU = T\,dS - p\,dV$,

$$dG = -SdT + Vdp \qquad (1.4.12)$$

Analogously to eqn (1.4.9), the new thermodynamic potential $H$ can be defined as

$$H = U - \left(\frac{dU}{dV}\right)_v \qquad (1.4.13)$$

From (1.4.8), we obtain

$$H = U + pV \qquad (1.4.14)$$

where $H$ stands for enthalpy. Through differentiation, it is revealed that $H$ is a function of $S$ and $p$:

$$dH = dU + pdV + Vdp \qquad (1.4.15)$$

$$dH = TdS + Vdp \qquad (1.4.16)$$

Considering the overall reaction of SOFCs,

$$H_2 + \frac{1}{2}O_2 \rightarrow H_2O$$

the difference in Gibbs free energy of formation of $\Delta G$ during the reaction can be given as

$$\Delta G = \Delta G_{H_2O} - \Delta G_{H_2} - \frac{1}{2}\Delta G_{O_2} \qquad (1.4.17)$$

If all the Gibbs free energy is consumed to electrical work, then

$$\Delta G = -nFE \qquad (1.4.18)$$

where $n$ and $F$ represent number of electrons involved in the chemical reaction and the Faraday constant, respectively.

If the reactant and products are all in their standard conditions, the reversible standard potential $E^0$ of the electrochemical reaction is defined as[17]

$$E^0 = -\frac{\Delta G^0}{nF} \qquad (1.4.19)$$

Here, the Gibbs free energy is dependent on the temperature by the relation

$$\Delta G = \Delta H - T\,\Delta S \qquad (1.4.20)$$

Substitution of the standard condition values ($T$ = 273.15 K, $p$ = 1 atm) into (1.4.19) gives the standard electrode potential $E^0$

$$E^0 = (237900\ J\ mol^{-1})/(2 * 96485\ C\ mol^{-1}) = 1.23\ \text{V}$$

Beyond the standard condition, the theoretical reversible potential $E_{th}$ can be derived by the Nernst equation as

$$E_{th} = E^0 - \left(\frac{RT}{2F}\right)\ln\left(\frac{p_{H_2O}}{p_{H_2}p_{O_2}^{\frac{1}{2}}}\right) \qquad (1.4.21)$$

where $R$ is the gas constant, $T$ is the absolute temperature, $p$ is the partial pressure of each gas.

### 1.4.2. Perovskite-type oxide structures as cathodes

In this sector, the relevant properties of perovskite-type oxides as SOFC cathodes, such as a simple and a double perovskite oxide, having general formula of $ABO_3$ and $AA'B_2O_5$, respectively, will be introduced.

#### 1.4.2.1. A simple perovskite oxide

Most of the $ABO_3$-type simple perovskite oxide crystallizes in the relatively simple structure of the mineral perovskite $CaTiO_3$ or in a structure closely related to it. Such oxides are known to exist with a wide range of A and B ions, having different sizes. The unit cell of the $ABO_3$ pervskite structure is shown in Fig. 2.[18] The ideal perovskite structure has a cubic unit cell of side about 3.9 Å with a space group of P*m*3*m* and contains one formula unit. The B cation has an 6-fold coordination, surrounded by an octahedron of anions, and the A cation has 12-fold coordination. The oxygen ions are linked to six cations (4A + 2B). The structure can be usefully described in other ways. First, it can be described as a ccp array of A and O atoms with the B atoms occupying the octahedral holes. Second, perovskite has the same octahedral framework as $ReO_3$ based on $BO_6$ octahedra with an A atom added in at the center of the cell. Compounds adopting this structure include $SrTiO_3$, $SrZrO_3$, $SrHfO_3$, $SrSnO_3$, and $BaSnO_3$.[19,20]

It is well known that the ionic radii of the component ions play important roles in determining the crystal structure of compounds. The criterion called "tolerance factor *t*" can be used as a measure of the deviation of the $ABO_3$ perovskite structure from the ideal cubic symmetry. The Goldschmidt tolerance factor *t* is described as the following equation:[21]

$$t = \frac{(r_A + r_O)}{\sqrt{2}(r_B + r_O)} \qquad (1.4.2.1.1)$$

where $r_A$, $r_B$ and $r_O$ are the ionic radius of A, B, and O ions, respectively. A decrease in A cation size causes a lowering to the crystal symmetry and an increasing bending of the O-B-O bond angle from the ideal value of 180°. The closer to cubic, the closer the value of the tolerance factor is to unity because the constant, *t*, can be used as a measure of the degree of distortion of a perovskite from ideal cubic. In perovskite-type compounds, the value of t lies between about 0.80 and 1.10.[22] Limiting values for the tolerance factor have been determined through experiment. For example, it is reported that the perovskite sustains cubic if $0.9 < t < 1.0$, and orthorhombic if $0.75 < t < 0.9$. If the value of *t* drops below 0.75, the compound might adopt an hexagonal ilmenite structure ($FeTiO_3$).[18,20]

The simple perovskite oxides, particularly mixed ionic/electronic conductors (MIECs) containing Mn, Fe, Co, and/or Ni, have been extensively investigated as IT-SOFC cathode materials. Cobalt containing oxides, such as $Ba_{0.5}Sr_{0.5}Co_{0.8}Fe_{0.2}O_{3-\delta}$, $Pr_{1-x}Sr_xCoO_3$, $Sm_{0.5}Sr_{0.5}CoO_3$, $La_{1-x}Sr_xCo_{1-y}Fe_yO_{3-\delta}$, and $Ba_{0.6}La_{0.4}CoO_3$, have attracted much interest due to their high electro-catalytic activity

for the oxygen reduction reaction (ORR) at the cathode.[23-26] Unfortunately, the challenge with respect to which spin state transition of Co in Co-based material causes high thermal expansion coefficient (TEC) still remains. Finding good compromise between conductivity and TEC by a partial substitution of Co by other elements, such as Fe, Mn, and Ni, may be one of the strategies to solve the problem arising from use of Co-rich materials.[27,28]

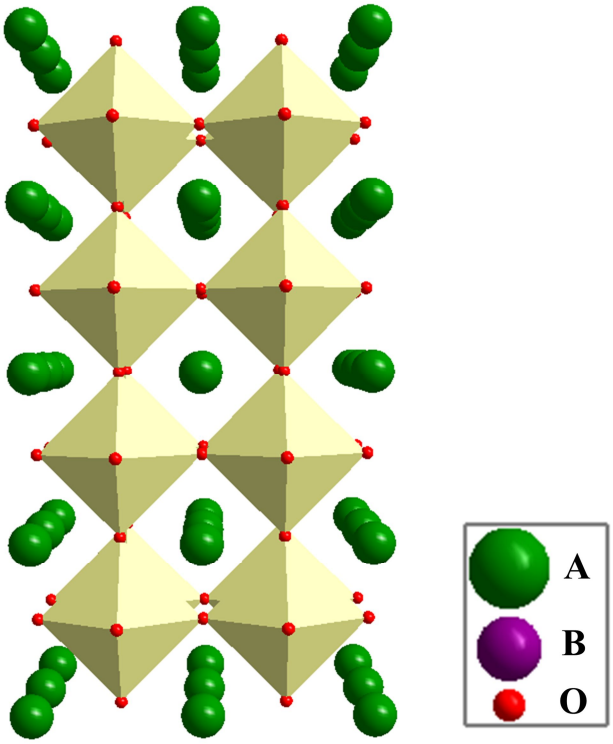


**Fig. 2.** Crystal structure of a simple perovskite oxide.

### 1.4.2.2. A double perovskite oxide

The double perovskite structure is named because the unit cell of is twice that of perovskite. It has the same architecture of 12 coordinate A sites and 6 coordinate B site, but two cations are ordered on the B site as shown in Fig. 3. This structure can be described with the general formula $AA'B_2O_{5+\delta}$, consisting of sequential layers $[BO_2]$-[AO]-$[BO_2]$-[A′O] stacked along the *c*-axis, where A = rare earth, A' = alkaline earth, and B = transition metal.[29] This layered structure reduces the oxygen bonding strength in the [AO] layer and provides a disorder-free channel for ion motion, which enhances oxygen diffusivity.[30]

Based on these promising properties, many groups have intensively focused on the double perovskite oxides because they offer much higher chemical diffusion and a high surface exchange coefficient relative to those of $ABO_{3-\delta}$-type simple perovskite oxides. $LnBaCo_2O_{5+\delta}$ (Ln = La, Pr, Nd,

Sm, and Gd) compounds are well known layered perovskite oxides with high mixed ionic and electronic conductivity and faster oxygen transport, even at the temperatures below 500 $^{o}$C, which give rise to their high catalytic activity for ORR. The vacant sites are arranged so that the coordination number for A cation is eight when $\delta = 0$. All oxygen vacancies are confined only to the Ln-O plane, and so is oxygen migration.[31]

For example, Kim et al. have revealed that the chemical diffusion coefficient ($D$) and the surface exchange coefficient ($k$) in the layered perovskite $PrBaCo_2O_{5+\delta}$ are much higher than that of a simple $ABO_3$-type perovskite. Moreover, the bulk diffusion in $PrBaCo_2O_{5+\delta}$ is larger than that in $GdBaCo_2O_{5+\delta}$, implying that the former may have a higher ionic conductivity than the latter under the same conditions.[32,33]

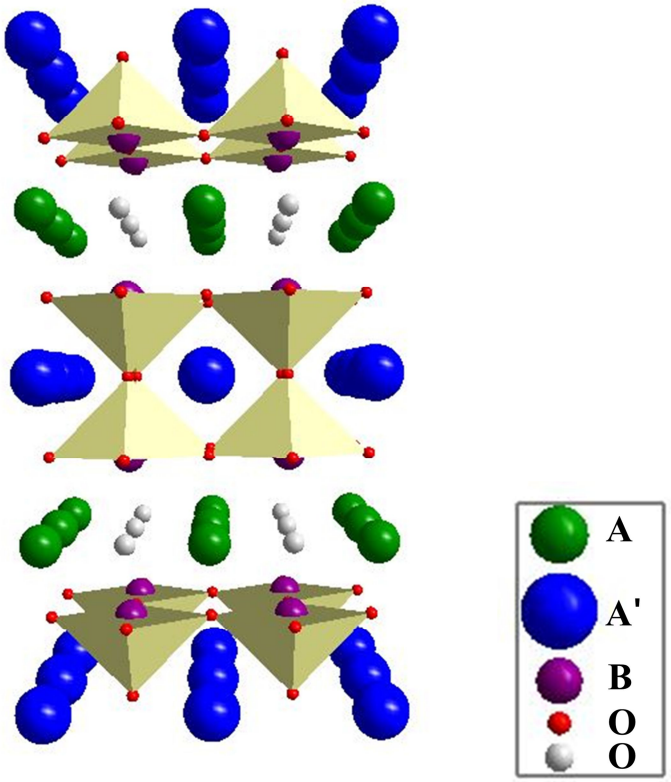


**Fig. 3.** Crystal structure of a double perovskite oxide.

### 1.4.3. Oxygen reduction reaction mechanisms in SOFC cathode materials

At the cathode side, the electrochemical reduction of the molecular oxygen as seen in (1.4.3.1) takes place in a series of elementary electrochemical steps, which include adsorption, dissociation, surface diffusion, and charge transfer, resulting in the formation of oxygen ions.[34]

$$\frac{1}{2}O_{2,gas} + V_O^{\bullet\bullet} + 2e' \rightarrow O_O^x \qquad (1.4.3.1)$$

The cathode material therefore should possess a high catalytic activity for the oxygen reduction, a high electronic conductivity, chemical and structural stability at high temperatures and in oxidizing atmospheres, and compatibility with the other cell components. SOFC cathode materials can be divided into 3 main groups: (1) a electronic conductor, (2) a mixed ionic and electronic conductor, and (3) two-phase composite mixed conductor.

For understanding of oxygen reduction reaction (ORR) at a cathode, it should be noted that ORR occurs only at electrochemical reaction zone, typically called triple phase boundary (TPB) where electronic conductor, ionic conductor, and gas are in contact. Fig. 4 illustrates the phenomenological role of the cathode, electrolyte, and gas in accomplishing the reaction in the equation (1.4.3.1). A common feature of all cathodes is that the cathode material itself, $\alpha$, (an electronic conductor) makes intimate contact with an electrolyte phase, $\gamma$, (an oxygen-ion conductor) along an interface, this interface also being exposed at its edge to the gas phase, $\beta$. Phase α is connected at some point away from the interface to a source of electronic current, providing a conduction path for electrons to the interface. Likewise, the electrolyte phase $\gamma$ is either itself the electrolyte membrane or connected by a continuous ionic path to the electrolyte membrane, providing a sink for the oxygen ions produced in the reaction. The oxygen gas (which diffuses from outside the electrode through interconnected pores or channels) is reduced somewhere in the vicinity of this $\alpha/\beta/\gamma$ interface.[35]

Fig. 5 outlines some of the mechanisms either known or theorized in the literature to be important in determining the rate of the oxygen reduction at the cathodes. Oxygen molecules are generally thought to adsorb somewhere onto one or more solid surfaces, where they undergo catalytic and/or electro-catalytic reduction steps to form partially reduced ionic/atomic species called electro-active species.[35] Before, after, or between partial reduction steps, these species must be transported along surfaces, interfaces, or inside the bulk of the electrode materials to the electrolyte, where they are fully and formally incorporated as electrolytic $O_2^-$. If, how, and where any of these processes happen and what steps are rate determining for a particular electrode is often only partially understood. Which steps are rate determining, and thus which factors are important for cathode performance, depends strongly on the materials, microstructure, and processing of the electrode as well as the conditions under which electrode is tested, including temperature, atmosphere, polarization, and time.[35]

The simplified schematics of the TPB at a cathode are shown in Fig. 4. The reaction kinetics (especially the ORR kinetics) often present a significant limitation to fuel cell performance. Therefore, understanding, characterizing, and optimizing the TPB content in SOFCs provides excellent opportunities for performance enhancement.

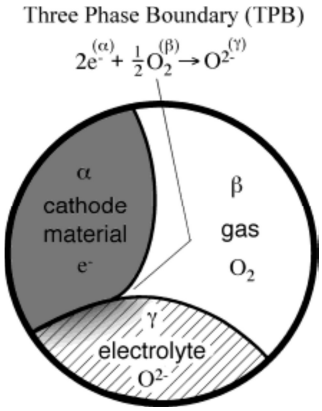


**Fig. 4.** Phenomenological roles of the electronically conducting (electronic) phase ($\alpha$), gas phase ($\beta$), and ionically conducting (ionic) phase ($\gamma$) in accomplishing oxygen reduction.[35]

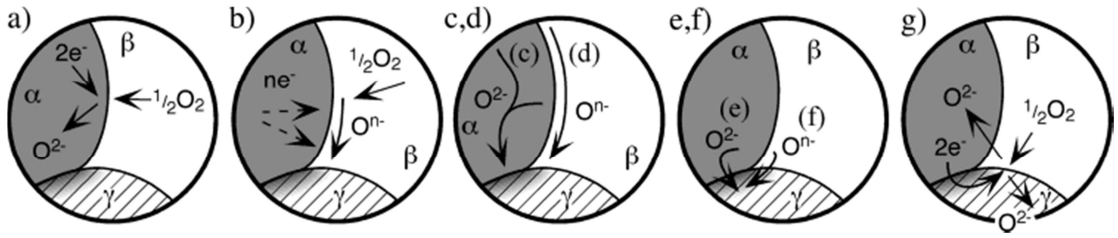


**Fig. 5.** Some mechanisms thought to govern oxygen reduction in SOFC cathodes. Phases $\alpha$, $\beta$, and $\gamma$ refer to the electronic phase, gas phase, and ionic phase, respectively: (a) Incorporation of oxygen into the bulk of the electronic phase (if mixed conducting); (b) adsorption and/or partial reduction of oxygen on the surface of the electronic phase; (c) bulk or (d) surface transport of $O^{2-}$ or $O^{n-}$, respectively, to the $\alpha/\gamma$ interface, (e) Electrochemical charge transfer of $O^{2-}$ or (f) combinations of $O^{n-}$ and $e^-$, respectively, across the $\alpha/\gamma$ interface, and (g) rates of one or more of these mechanisms wherein the electrolyte itself is active for generation and transport of electro-active oxygen species.[35]

#### 1.4.3.1. Electronic conductor

In purely electronic conducting materials, such as (La, Sr)$MnO_3$ (LSM),[36] the oxygen has to be transported in the gas phase (gas diffusion) or as an adsorbed species along the surface (surface diffusion) of a porous cathode structure. The incorporation of oxygen into the purely ionic-conducting electrolyte is restricted to the three phase boundaries (TPBs) between cathode, electrolyte, and gas phase. Only here do electrons (from the cathode), oxygen (from the gas phase), and oxygen vacancies (from the electrolyte) meet, thus enabling the incorporation reaction. Therefore, the cathode performance is linked to the electrode microstructure, *i. e.*, the geometrical arrangement of the TPB. Fig. 6 (a) presents the possible reaction zones for ORR on a pure electronic conductor with ionic conductor of electrolyte.

#### 1.4.3.2. A single phase mixed ionic and electronic conductor (MIEC)

Mixed ionic and electronic conductors (MIECs) have been received significant attention as candidate materials for SOFC components, such as permeation membranes, oxygen storage capacitors, electrochemical sensors, and active catalyst support.[35,38-40] As a fuel cell electrode, MIECs have the potential to extend the electrochemical reaction zone beyond the triple-phase boundary at which electrode, electrolyte and gas phase are simultaneously in contact. The use of a MIEC material as a cathode can extend the electrochemical reaction zone over the entire surface because oxygen anions can transport through the MIEC bulk, e.g. $La_{0.6}Sr_{0.4}Co_{0.2}Fe_{0.8}O_{3-\delta}$.[41] The electrochemically active region can be extended, because the ORRs can also take place on the two phase boundary (2PB) where the gas and mixed conductor meet as illustrated in Fig. 6 (b).[42] Recognition of this inherent advantage of MIECs has driven efforts to develop oxides with both high ionic and high electronic conductivity as a SOFC cathode material. It is further recognized that, in addition to high bulk diffusion rates, high surface activity is also essential for high performance from an oxide electrode. What remains unclear are the relative contributions of reaction and diffusion kinetics to the overall interfacial impedance associated with MIECs, and the role that microstructure may play in balancing these factors.

#### 1.4.3.3. Two-phase composite mixed conductor

To effectively improve the electrochemical performance of SOFCs, one effective approach has been adopted by adding a secondary phase of higher ionic conductivity, such as GDC and YSZ, in MIEC cathode material to extend the active area which the oxygen reduction reaction can occur. The combination of an ionically conducting phase and MIEC electrode may boost the electrochemical reaction by providing additional TPB sites for the ORR. Such electrodes are referred to as composite cathodes and have showed significant enhancements in electrochemical performances. As illustrated in Fig. 6 (c), the electrochemically active areas of composite cathodes can be divided into three pathways: the TPB point where the electrolyte, cathode, and gas are in contact, the 2PB point on the surface of the pure MIEC cathode, and the extended TPB point by the addition of ionic conducting phase into the cathode.[37,43]

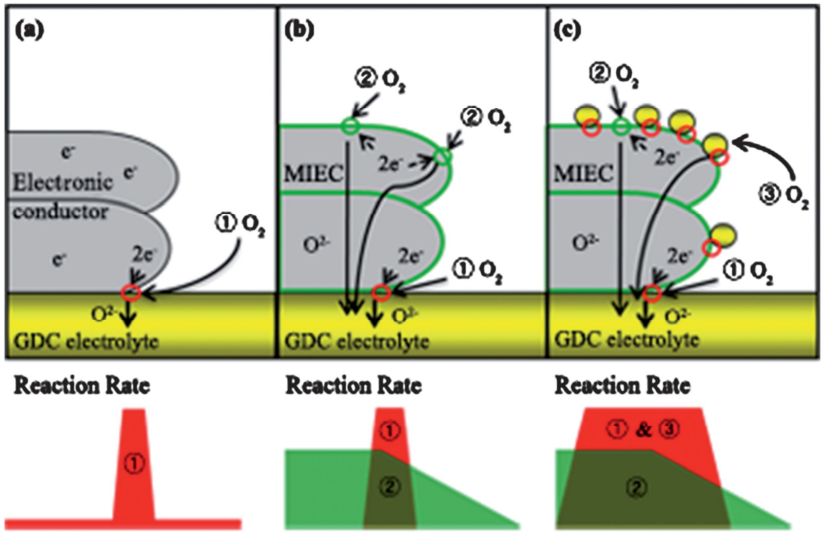


**Fig. 6.** Schematics of the oxygen reduction reaction at (a) electronic conductor (TPB concept), (b) MIEC (TPB + 2PB), and (c) MIEC-ionic conductor, GDC (enlarged TPB + 2PB) (path①; TPB point between the electrolyte and cathode, path②; 2PB point on the surface of NBSCO, and path ③; enhanced TPB point by addition of GDC).[43]

### 1.4.5. Transport processes in SOFC

There are representative transfer processes of charge, heat and mass transfer occurring in SOFCs. The strong interactions are the consequence of the high degree of integration of different processes (chemical/electrochemical reactions, diffusion, heat and mass transfer) within SOFCs.[44] The understanding of these interactions can be a key for the future development and application of SOFCs.

#### 1.4.5.1. Charge transport

Charge transport completes the circuit in an electrochemical system, moving charges from the electrode where they are produced to the electrode where they are consumed. There are two major types of charge species: electrons and ions. The transport of electrons versus ions is fundamentally different, primarily due to the large difference in mass between the two. In most SOFCs, ion charge transport is far more difficult than electron charge transport. The resistance to charge transport results in a voltage loss because this voltage loss obeys Ohm's law, called an ohmic or *IR* loss. The reduction in voltage is called "*ohmic* loss," and includes the electronic ($R_{\text{elec}}$) and ionic ($R_{\text{ionic}}$) contributions, written as:[17]

$$v_{\text{ohmic}} = iR_{\text{ohmic}} = i(R_{\text{elec}} + R_{\text{ionic}}) \qquad (1.4.5.1.1)$$

These losses can be minimized by making electrolytes as thin as possible and employing high-conductivity materials.

The rate at which charges move through a material is quantified in terms of flux ($J$). Flux

measures how much of given quantity flows through a material per unit are per unit of time. Charge flux ($j$) measures the amount of the charges that flow through a material per unit area per unit of time with typical units:

$$\frac{C}{cm^2 s} = \frac{A}{cm^2} \qquad (1.4.5.1.2)$$

The quantity $z_i F$ is required to convert from molar flux $J$ to charge flux $j$, where $z_i$ is the charge number for the carrier and $F$ is Faraday's constant:

$$j = z_i F J \qquad (1.4.5.1.3)$$

If there is no force acting on the charge carriers, there is no reason for them to move. The governing equation for transport can be generalized as

$$J_i = \sum_k M_{ik} F_k \qquad (1.4.5.1.4)$$

where $J_i$ represents a flux of species $i$, $F_k$represents the $k$ different forces acting on $i$ and the $M_{ik}$ is the coupling coefficients which reflect the relative ability of species to respond to a given force with movement as well as the effective strength of the driving force itself.

For the case where charge transport is dominated by electrical driving forces, equation (1.4.5.1.3) can be rewritten as

$$j = \sigma \frac{dV}{dx} \qquad (1.4.5.1.5)$$

where $j$ stands for the charge flux, *dV*/*dx* is the electric field providing the driving force for charge transport, and $\sigma$ is the conductivity, which measures the propensity of a material to permit charge flow in response to an electric field. The conductivity quantifies the ability of a material to permit the flow of charge when driven by an electric field. The conductivity of a material is influenced by two major factors: how many carriers are available to transport charge and the mobility of those carriers within the material. The following equation defined $\sigma$ in those terms:

$$\sigma_i = (|z_i|F) c_i u_i \qquad (1.4.5.1.6)$$

where $c_i$ represents the molar concentration of charge carriers and $u_i$ is the mobility of the charge carriers within the material.

Table 2 shows the summary of transport processes relevant to charge transport. It gives the driving force, coupling coefficient and equation for conduction, diffusion, and convection.

For operating SOFCs, the penalty for charge transport is a loss in cell voltage due to the presence of an intrinsic resistance to charge flow. The voltage loss associated with charge transport can be given by the equation:

$$\eta_{\text{ohmic}} = j(\text{ASR}_{\text{ohmic}}) \qquad (1.4.5.1.7)$$

where ASR stands for area-specific resistance and carries unit of Ω $cm^2$. ASR accounts for the fact that fuel cell resistance scales with area, thus allowing fuel cells of different sizes to be compared. It is

calculated by multiplying ohmic resistance $R_{\text{ohmic}}$ by its area:

$$\text{ASR}_{\text{ohmic}} = A_{\text{cell}} R_{\text{ohmic}} \qquad (1.4.5.1.8)$$

**Table 2. Summary of Transport processes relevant to charge transport**[6]

| Transport Process | Driving Force | Coupling Coefficient | Equation |
|---|---|---|---|
| Conduction | $\frac{dV}{dx}$ | Conductivity $\sigma$ | $J = \frac{\sigma}{\lvert z_i \rvert F} \frac{dV}{dx}$ |
| Diffusion | $\frac{dc}{dx}$ | Diffusivity $D$ | $J = -D \frac{dc}{dx}$ |
| Convection | $\frac{dp}{dx}$ | Viscosity $\mu$ | $J = \frac{Gc}{\mu} \frac{dp}{dx}$ |

### 1.4.5.2. Mass transport

To produce electricity, fuel an-d oxidant must be supplied continuously. At the same time, products must be continuously removed so as to avoid "strangling" the cell. The process of supplying reactants and removing products is termed mass transport. We now deal with the transport of uncharged species, which thus are unaffected by voltage gradients and so must instead rely on convective and diffusive forces for movement mostly concerned with gas-phase transport. For the case of SOFC, mass transfer mainly refers to diffusion of gas species and transport in porous layer.

Diffusion is a spontaneous process that is a result of the second law of thermodynamics, which requires thermodynamic processes proceed in away, maximizing entropy. Fick's law of diffusion is written as:[17]

$$\dot{n}_{j,i} = -D_{j,i} A \frac{\partial c_j}{\partial x_i} \qquad (1.4.5.2.1)$$

where $D_{j,i}$ is the diffusion coefficient of species $j$ with units of cubic meters per second, $A$ is the area through which diffusion occurs, $c_j$ is the molar concentration of $j$, $x_i$ is the direction of transport ($x$, $y$, or $z$ direction), and $n_{j,i}$ is the molar rate of transport of $j$ in the $i$ direction.

For 1-dimension, therefore, it can be written as:

$$\dot{n}_{j,} = -D_j A \frac{dc_j}{dx} \qquad (1.4.5.2.2)$$

where $D_j$ = 0.1 cm$^2$ s$^{-1}$ for gases.

From the concentration variations, we calculate how much the Nernst potential changes (the incremental voltage loss ($\eta_{conc}$) when using $c_R^*$ values instead of $c_R^0$ values ($c_R^*$ = catalyst layer reactant concentration and $c_R^0$ = bulk reactant concentration) :

$$\eta_{conc} = E^0_{Nernst} - E^*_{Nernst}$$
$$= \left(E^0 - \frac{RT}{nF}\ln\frac{1}{c^0_R}\right) - \left(E^0 - \frac{RT}{nF}\ln\frac{1}{c^*_R}\right)$$
$$= \frac{RT}{nF}\ln\frac{c^0_R}{c^*_R}$$

where $E^0_{\text{Nernst}}$ is the Nernst voltage using $c^0$ values and $C^*_{\text{Nernst}}$ is the Nernst voltage using $c^*$ values. $c^0_R$ can be described in terms of the limiting current density ($j_L$).

The concentration also affects reaction rate that plays an important role to determine cell performances. We are concerned primarily with the high-current-density region and thus the reaction kinetics may be described by the simplified expression of Butler-Volmer equation:

$$j = j^0_0\left(\frac{c^*_R}{c^{0*}_R}e^{\alpha nF\eta_{\text{act}}/(RT)}\right) \qquad (1.4.5.2.3)$$

where $j^0_0$ represents the exchange current density at a standard concentration, $c^*_R$ and $c^{0*}_R$ are arbitrary and reference reactant concentration values, respectively, $\eta_{\text{act}}$ is the activation loss, and $\alpha$ is the transfer coefficient which expresses how the change in the electrical potential across the reaction interface changes the sizes of the forward versus reverse activation barrier ($0 < \alpha < 1.0$).

Written in terms of the activation overvoltage, it becomes

$$\eta_{\text{act}} = \frac{RT}{\alpha nF}\ln\frac{jc^{0*}_R}{j^0_0 c^*_R} \qquad (1.4.5.2.4)$$

How much the activation overvoltage is charged can be calculated using $c^*_R$ values.

$$\eta_{\text{conc}} = \eta^*_{\text{act}} - \eta^0_{\text{act}} = \left(\frac{\text{RT}}{\alpha\text{nF}}\ln\frac{jc^{0*}_R}{j^0_0 c^*_R}\right) - \left(\frac{\text{RT}}{\alpha\text{nF}}\ln\frac{jc^{0*}_R}{j^0_0 c^0_R}\right)$$
$$= \frac{\text{RT}}{\alpha\text{nF}}\ln\frac{\text{c}^0_\text{R}}{\text{c}^*_\text{R}}$$

The ratio $c^{0*}_R/c^*_R$ equals $(j_L/(j_L - j))$ which provides the expression for $\eta_{\text{conc}}$ as:

$$\eta_{\text{conc}} = \frac{RT}{\alpha nF}\ln\frac{j_L}{j_L - j} \qquad (1.4.5.2.5)$$

**References**


1. H. Rickert, *Electrochemistry of Solids*, Berlin, Germany: Springer-Verlag (1982) pp 1 ~ 5.
2. N. Q. Minh, T. Takahshi, *Science and Technology of Ceramic Fuel Cells*, Elsevier Science B. V., Amsterdam, Netherlands (1995) pp 4 ~ 6.
3. S. C. Singhal, K. Kendall, *High temperature solid oxide fuel cells: fundamentals, design, and applications* Oxford: Elsevier Science Ltd. (2003) pp 1 ~ 8.
4. F. Alcaide, P. -L. Cabot, E. Brillas, *J. Power Sources* **153** (2006) 47.
5. S. P. S. Badwal, *Solid State Ionics* **143** (2001) 39.
6. R. O'Hayre, S. W. Cha, W. Colella, F. B. Prinz, *Fuel Cell Fundamentals* Hoboken: John Wiley & Sons, Inc. (2009) 3 ~ 16.
7. J. P. P Huijsmans, F. P. F van Berkel, G. M Christie, *J. Power Sources* **71** (1998) 107.
8. B. C. H. Steele, A. Heinzel, *Nature* **414** (2001) 345.
9. S. D. Park, J. M. Vohs, R. J. Gorte, *Nature* **404** (2000) 265.
10. N. P. Brandon, S. Skinner, B. C. H. Steele, *Ann. Rev. Mater. Res.* **33** (2003) 183.
11. Z. P. Shao, S. M. Haile, J. Ahn, P. D. Ronney, Z. L. Zhan, S. A. Barnett, *Nature* **435** (2005) 795.
12. A. Lashtabeg, S. J. Skinner, *J. Mater. Chem* **16** (2006) 3161.
13. E. V. Tsipis, V. V. Kharton, *J. Solid State Electrochem.***12** (2008) 1367.
14. A. Aguadero, L. Fawcett, S. Taub, R. Wooley, K. T. Wu, N, Xu, *J. Mater. Sci.***47** (2012) 3925.
15. R. Bove, S. Ubertini, *Modeling Solid Oxide Fuel Cells: Chapter 2. Thermodynamics of Fuel Cells*, Springer (2008) pp 15 ~ 24.
16. C. M. A. Brett, A. M. O. Brett, *Electrochemistry: Principles, Methods, and Applications*, Oxford University Press Inc., New York, USA (1993) pp 14.
17. A. J. Bard, L. R. Faulkner, *Electrochemical Methods: Fundamentals and Applications*, New York, Jogn Wiley & Sons, New York (2000).
18. F. Galasso, *Structure and Properties of Inorganic Solids*, Pergamon, New York (1970).
19. K. Miura, M. Azuma, H. Funakubo, *Material* **4** (2011) 260.
20. D. D. Khalyavin, A. N. Salak, N. P. Vyshatko, A. B. Lopes, N. M. Olekhnovich, A. V. Pushkarev, I. I. Maroz, T. V. Radyush, *Chem. Mater.* **18** (2006) 5104.
21. V. M. goldshmidt, *Skr. Nor. Vidensk. Akad. Oslo*, **2** (1926) 79.
22. O. Fukunga and T. Fujita, *J. Solid State Chem.* **8** (1973) 331.
23. S. Park, S. H. Choi, J. Y. Shin, G. Kim, *J. Power Sources* **210** (2012) 172.
24. T. Ishihara, S. Fukui, H.Nishiguchi, Y.Takita, *J.Electrochem. Soc.* **149** (2002) A823.
25. J. H. Kim, M. Cassidy, J. T. S. Irvine, J. Bae, *Chem.Mater.* **22** (2010) 883.
26. S. H. Choi, J. Y. Shin, K. M. Ok, G. Kim, *Electrochim. Acta* **81** (2012) 217.
27. H. H. Wang, C. Tablet, A. Feldhoff, J. Caro, *Adv. Mater.* **17** (2005) 1785.

28. O. Yamamoto, Y. Takeda, R. Kanno, N. Noda, *Solid State Ionics* **22** (1987) 241.
29. D .J. Chen, R. Ran, K. Zhang, J. Wang, Z. P. Shao, *J. Power Sources* **188** (2009) 96.
30. A. A.Taskin, A. N. Lavrov, Y. Ando, *Progress in Solid State Chemistry* **35** (2007) 481.
31. K. Zhang, L. Ge, R. Ran, Z. Shao, S. Liu, *Acta Materialia* **56** (2008) 4876.
32. G. Kim, S. Wang, A. J. Jacobson, L. Reimus, P. Brodersen, C.A. Mims, *J. Mater. Chem.* **17** (2007) 2500.
33. B. Lin, S. Zhang, L. Zhang, L. Bi, H. Ding, X. Liu, J. Gao, G. Meng, *J. Power Sources* **177** (2008) 330.
34. C. K. Dyer, P. T. Moseley, Z. Ogumi, D. A. J. Rand, B. Scrosati, *Newnes*, Encyclopedia of Electrochemical Power Sources (2013)
35. S. B. Adler, *Chem. Rev.* **104** (2004) 4791.
36. Kleitz, M.; Kloidt, T.; Dessemond, L. *High-Temperature Electrochemical Behavior of Fast Ion and Mixed Conductors*; Roskilde: Denmark (1993) pp 89.
37. C. Zhu, X. Liu, D. Xu, D. Wang, D. Yan, L. Pei, T. Lu, W. Su, *J. Power Sources* **185** (2008) 212.
38. S. P. Jiang, S. H. Chan, *J. Mater. Sci.* **39** (2004) 4405.
39. A. Trovarelli, *Catal. Rev. Sci. Eng.* **38** (1996) 439.
40. A. J. Jacobson, *Chem. Mater.* **22** (2010) 660.
41. J. A. Lane, S. J. Benson, D. Waller, J. A. Kilner, *Solid State Ionics* **121** (1999) 201.
42. Q. Zhou, W. Wang, T. Wei, X. Qi, Y. Li, Y. Zou, Y. Liu, Z. Li, Y. Wu, *Ceram. Int.* **38** (2010) 1529.
43. J. Y. Kim, W. Y. Seo, J. Y. Shin, M. Liu, G. Kim, *J. Mater. Chem. A* **1** (2013) 515.
44. J. Maier, *Solid State Ionics* **112** (1998) 197.

## 2. Experimental

### 2.1. Material synthesis

The materials were synthesized by the Pechini process using the chemicals, such as $Pr(NO_3)_3 \cdot 6H_2O$ (Aldrich, 99.9%, metal basis), $Ba(NO_3)_2$ (Aldrich, 99+%),$Sr(NO_3)_2$ (Aldrich, 99+%), $Co(NO_3)_2 \cdot 6H_2O$ (Aldrich, 98+%), $Cu(NO_3)_2 \cdot 2.5H_2O$ (Aldrich, 98%), and $Fe(NO_3)_3 \cdot 6H_2O$ (Aldrich, 98%), with the addition of ethylene glycol and citric acid as heterogeneous agents in distilled water, followed by a self-combustion process to form submicron p

owder particles. These powders were pre-calcined at 600 $^oC$ for 4h and then ball-milled in acetone for 24 h. The calcined powders were then dry-pressed into pellets at 5 MPa and sintered at 1100 ~ 1150 $^oC$ for 12h in air. For measurement of the cell performances of the materials, slurries consisting of powders, GDC, and an organic binder (Heraeus V006) were used.

### 2.2. Cell fabrication

Ni-GDC anode-supported cells were fabricated to measure the electrochemical performances of the materials. A Ni-GDC cermet anode was prepared by a mixture of nickel oxide, GDC, and starch prepared via ball-milling in ethanol for 24 h. After drying process, the NiO-GDC mixture was pressed into pellets (~ 0.6 mm in thickness and 15 mm in diameter). Thin GDC electrolyte membranes were prepared by a refined particle suspension coating technique or co-pressing GDC powders synthesized using glycine nitrate process (GNP) method over a pelletized disk of a Ni-GDC cermet anode. A GDC suspension was prepared by dispersing GDC powder (Aldrich) in ethanol with a small amount of binder (polyvinyl Butyral, B-98) and dispersant (Triethanolamine, Alfa Aesar) at a ratio of 1:10. The GDC suspension was applied to a NiO-GDC anode support by drop-coating, followed by drying in air and subsequent co-sintering at 1400 $^oC$ for 5 h. The electrode slurries were then screen-printed onto the GDC electrolyte layer. The single cell consisting of 3 layers (Ni-GDC as an anode, GDC as an electrolyte, and a cathode) were sintered under an air atmosphere with an active electrode area of 0.36 $cm^2$.

### 2.3. Characterization

#### 2.3.1. Structural analysis

The phase identification of the materials at room temperature was carried out by X-ray powder diffraction (XRD) (Rigaku-diffractometer, Cu Ka radiation) with a scanning rate of 0.5 $^o$ $min^{-1}$ in the 2θ range of 20 $^o$ to 60 $^o$. A phase transition at high temperature was identified by in-situ XRD (Bruker D8 ADVANCE XRD). For the high temperature XRD measurements, the samples were mounted on alumina alloy and resistively heated in the temperature ranges from room temperature to 800 $^oC$ in air. The microstructures of the interface between the electrolyte and the electrode were investigated using

a field emission scanning electron microscope (SEM) (Nova SEM). Further crystal chemistry of the materials was analyzed by Rietveld refinement method using GSAS program.[1] The XRD patterns were collected with a slow scanning rate of 0.2 $^{o}$ $min^{-1}$ in the 2θ range of 20 $^{o}$ to 100 $^{o}$.

### 2.3.2. Iodometric titration

The oxygen content and average oxidation state at room temperature, composing the samples, were identified using iodometric titration. The bulk powders were dissolved in 15 mL of 10 % KI solution followed by adding 10 mL of 3.5 N HCL. The solution was stirred until the sample was completely dissolved under $N_2$ atmosphere. The clearly dissolved solution was then titrated against 0.03 N sodium thiosulfate ($Na_2S_2O_3$) solution using starch as an indicator.

### 2.3.3. Thermal analysis

Thermogravimetric analysis (TGA) was carried out by a SDT-Q600 (TA Instruments, USA) to identify the weight changes of the samples during heating and cooling processes from room temperature to 800 $^{o}$C with a heating/cooling rate of 2 $^{o}$C $min^{-1}$ in air. The variations of the oxygen content as a function of temperature were derived by the initial oxygen content values at room temperatures. The thermal expansion coefficient values (TEC) of the samples were measured from 100 to 800 $^{o}$C with a heating/cooling rate of 5 $^{o}$C $min^{-1}$. TEC values of the samples were calculated as

$$\alpha = \frac{1}{L_0}\frac{dL}{dT} \qquad (2.3.3.1)$$

where $\alpha$ represents the TEC, $L_0$ is the length of the specimen at a specific temperature, and $T$ is the absolute temperature.

### 2.3.4. Electrochemical analysis

The electrical conductivities of the samples were evaluated by a four-terminal DC arrangement and a potentiostat (BioLogic) was used to measure the current and voltage at intervals of 50 $^{o}$C at temperature ranging from 100 $^{o}$C to 750 $^{o}$C. The specific values of the electrical conductivity at a specific temperature were calculated using[2]

$$\sigma = S\left(\frac{1}{A}\right)\left(\frac{1}{R}\right) \qquad (2.3.4.1)$$

where $\sigma$ represents the electrical conductivity, $A$ is the area of cross section, $R$ is the resistance, and $S$ stands for the length of the conductor.

Electrochemical impedance spectroscopy of the materials was carried out using a symmetrical cell. The GDC electrolyte powders were pressed into pellets, and then sintered at 1350 $^{o}$C for 4h in air to obtain a dense electrolyte substrate. Slurries composed of an organic binder (Heraeus V006), the cathode and GDC powders were screen-printed onto both sides of the GDC electrolytes to form

symmetrical half-cells, followed by calcination at various temperatures (900 ~ 1050 $^{o}$C). A silver paste was used as a current collector for the electrodes. Impedance spectra were recorded under OCV in a frequency range of 1 mHz to 500 kHz with AC perturbation of 14 mV from 500 $^{o}$C to 650 $^{o}$C.

Electrochemical performance was evaluated using a Ni-GDC anode supported cell. Ag wires were attached at both electrodes of single cells using an Ag paste as a current collector. An alumina tube and a ceramic adhesive (Aremco, Ceramabond 553) were employed to fix the single cell. Humidified hydrogen (3 % $H_2O$) was applied as fuel through a water bubbler with a flow rate of 20 mL min$^{-1}$ and static air was used as an oxidant during single cell tests. *I-V* curves were examined using a BioLogicPotentiostat at operating temperature from 500 $^{o}$C to 650 $^{o}$C.

### 2.3.5. Coulometric titration

The oxygen nonstoichiometry of the materials under the oxygen partial pressures ($pO_2$) was measured by coulometric titration using yttria-stabilized zirconia (YSZ) tube (McDanel Advanced Ceramic Technologies, Z15410630) that functions as to pump oxygen out of the system and to detect the equilibrium $pO_2$ inside the tube. The samples were placed inside an oxygen ion conducting membrane of a YSZ tube. Ag paste (SPI Supplies, 05063-AB) was painted on the both outside and inside of the tube as electrodes. Platinum wire was employed as a lead wire to provide electrical connections to the instruments. After purging 5 % $O_2$–Ar gas over the sample in the tube for 12 h, $pO_2$ was determined from the open-circuit voltage (OCV). Oxygen could be added or removed from the tube by passing current through the same electrodes as used for the OCV sensor. The sample was allowed to equilibrate until the potential varied in a range of less than 1 mV h$^{-1}$. Oxygen non-stoichiometry was determined through this procedure at the temperature range from 650 to 750 $^{o}$C with 50 $^{o}$C intervals over a wide range of $pO_2$. Electrical conductivity was simultaneously measured by a four-terminal DC arrangement with a BioLogic Potentiostat.

### References

1. F. Izmi, R. A. Young, *The Rietveld Method*, Oxford University Press, Oxford (1993).

2. A. J. Bard and L. R. Faulkner, *Electrochemical Methods: Fundamentals and Applications*, New York, Jogn Wiley & Sons, New York, (2000)

## 3. Results

### 3.1. Electrochemical investigation of strontium doping effect on high performance $Pr_{1-x}Sr_xCoO_{3-\delta}$ ($x$ = 0.1, 0.3, 0.5, and 0.7) cathode for intermediate-temperature solid oxide fuel cells

The $Pr_{1-x}Sr_xCoO_{3-\delta}$ perovskite-type oxides have received extensive attention as a promising cathode material due to their favorable properties for realizing high performance intermediate temperature solid oxide fuel cells (IT-SOFCs). This study focuses on the electrical properties, electrochemical performance, and redox behavior of a perovskite oxide of $Pr_{1-x}Sr_xCoO_{3-\delta}$ ($x$ = 0.1, 0.3, 0.5, and 0.7). For $x$ = 0.1 and 0.3, the electrical conductivities increase with increasing strontium content. In the case of $x$ > 0.3, however, decreased electrical conductivity is observed with increasing $x$. The oxygen non-stoichiometry of $Pr_{1-x}Sr_xCoO_{3-\delta}$ using coulometric titration and its electrical conductivity in a wide range of oxygen partial pressure at 700 $^oC$ are also investigated. A Ni-GDC anode-supported cell is fabricated to evaluate the electrochemical performance of the $Pr_{1-x}Sr_xCoO_{3-\delta}$ cathode material. The maximum power density at 700 $^oC$ is 1.19 W $cm^{-2}$ for $x$ = 0.3, and the other samples also show high power density over 1.0 W $cm^{-2}$, except for at $x$ = 0.7. Given its high electrical conductivity and cell performance, $Pr_{0.7}Sr_{0.3}CoO_{3-\delta}$ is a favorable cathode material candidate for IT-SOFC applications.

#### 3.1.1. Introduction

Solid oxide fuel cells (SOFCs) offer numerous advantages for power generation, including high efficiency to generate electric energy from chemical energy, rapid reaction kinetics, an eco-friendly process, and efficient reclamation of waste heat. High operating temperature (800 ~ 1000 $^oC$), however, leads to high cost and undesired reactions between the electrode and electrolyte, which in turn cause electrode densification and polarization. Recently, intermediate temperature solid oxide fuel cells (IT-SOFCs) operated at 500 ~ 700 $^oC$ have been introduced to resolve the problem of high operating temperature of SOFCs, thereby allowing long-term stability and flexible choice in cell materials. The lowered operating temperature, however, causes relatively slow reaction kinetics for the oxygen reduction reaction (ORR) at the cathode, which results in considerable over-potential at the interface between the electrode and electrolyte. Therefore, the development of new cathode materials for lower operating temperature is considered an important avenue of research for IT-SOFC applications.[1-5]

The requirements of cathode materials for IT-SOFCs are high oxide ionic and electronic conductivities, lower thermal expansion, and high catalytic activity for the ORR.[6] Mixed ionic/electronic conductors (MIECs) containing Mn, Fe, Co, and/or Ni are IT-SOFC cathode materials, offering the capability to conduct oxygen ions and electrons simultaneously, leading to enlarged triple phases boundary (TPB) sites.[7-10] In particular, various MIEC oxides containing cobalt oxides, such as

$LaCoO_3$, (La, Sr)$CoO_3$, $BaCoO_3$, and (Ba, Sr)$CoO_3$, have attracted strong interest due to their high electro-catalytic activity for the ORR. Recently, Sr doped rare-earth cobalt oxides, $Ln_{1-x}Sr_xCoO_{3-\delta}$ (Ln = La, Pr, Nd, Sm, and Gd), have been extensively investigated on the basis of their good mixed conductivity and performance as IT-SOFC cathode materials.[11-15] Among them, $La_{1-x}Sr_xCoO_{3-\delta}$shows better electrical properties and higher catalytic activity, as well as good thermal stability at various temperatures and oxygen partial pressure.[16,17] $La_{1-x}Sr_xCoO_{3-\delta}$ cathodes, however, show an increased thermal expansion coefficient (TEC) caused by the increased Ln-O bond strength and the formation of oxide ion vacancies, indicating reduction of the smaller $Co^{4+}$ ions to larger $Co^{3+}$ ions.[18] In order to achieve lower thermal expansion, the La lanthanide is substituted by other smaller lanthanides to decrease the ionicity of the Ln-O bond and the electro-negativity of Ln. Among the smaller lanthanides (Pr, Nd, Sm, and Gd), Pr affords a relatively lower TEC than La and higher electrical conductivity and electrochemical performance than Nd, Sm, and Gd due to its comparatively straightened Co-O-Co bond angle approaching $180^o$ and a consequent increase in bandwidth.[11,18] Therefore, Sr doped rare-earth cobalt oxide, $Pr_{1-x}Sr_xCoO_{3-\delta}$, has been studied as a prospective cathode material for IT-SOFC applications.

This study mainly focuses on the structure, electrochemical properties, and electrical performances of $Pr_{1-x}Sr_xCoO_{3-\delta}$($x$ = 0.1, 0.3, 0.5, and 0.7) using $Ce_{0.9}Gd_{0.1}O_{1.95}$ (GDC) electrolyte to eliminate inappropriate reactions between the electrolyte and cathode. For example, the reaction between $La_{1-x}Sr_xCoO_{3-\delta}$ and yttria stabilized zirconia (YSZ) electrolyte stimulates the formation of $La_2Zr_2O_7$ and $SrZrO_3$ at high temperature.[19] Additionally, oxygen non-stoichiometry and redox properties of $Pr_{1-x}Sr_xCoO_{3-\delta}$ are measured by coulometric titration .

### 3.1.2. Results and Discussion

The XRD patterns of $Pr_{1-x}Sr_xCoO_{3-\delta}$ cathodes with various strontium content ($x$ = 0.1, 0.3, 0.5, and 0.7) are shown in Fig. 7 (a). $Pr_{1-x}Sr_xCoO_{3-\delta}$ oxides sintered at 1150 $^oC$ for 4 h show appropriate peaks, indicating that the perovskite structure is formed and there are no impurity peaks. The peaks reflect an orthorhombic perovskite GdFeO-type structure (space group Pbnm).[20] The XRD spectra of $Pr_{1-x}Sr_xCoO_{3-\delta}$-GDC powder composites calcined at 900 $^oC$ for 2 h in air are illustrated in Fig. 7 (b). There are no obvious reactions between $Pr_{1-x}Sr_xCoO_{3-\delta}$ and GDC at 900 $^oC$ and the patterns verify that all samples obtain a stable perovskite structure. Secondary phases are observed at approximately $2\theta = 32.2^o$ and indexed to a tetragonal system.[20]

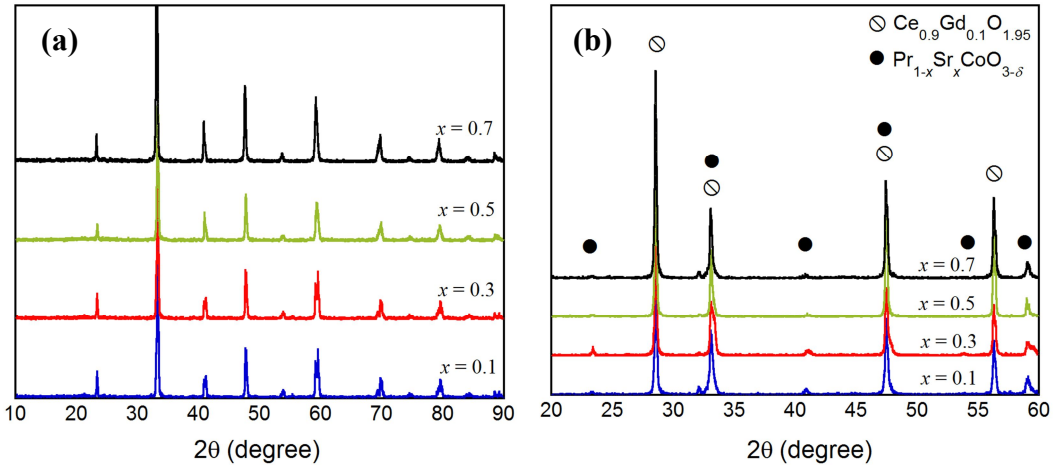


**Fig. 7.** (a) X-ray diffraction patterns of $Pr_{1-x}Sr_xCoO_{3-\delta}$ ($x$ = 0.1, 0.3, 0.5, and 0.7) sintered at 1150 $^{o}$C for 4 h. (b) X-ray diffraction patterns of $Pr_{1-x}Sr_xCoO_{3-\delta}$-GDC ($x$ = 0.1, 0.3, 0.5, and 0.7) sintered at 900 $^{o}$C for 2 h.

The microstructure of the $Pr_{1-x}Sr_xCoO_{3-\delta}$ cathode is examined by SEM image in Fig. 8. The electrode microstructure is related to the characteristics of the surface area, electrochemically active area, volume fraction of chemical phases present, and electron transport. These properties affect the reaction kinetics, charge transport, and mass transport processes, which are correlative with the fuel cell performance.[21,22] SEM images of $Pr_{1-x}Sr_xCoO_{3-\delta}$ screen printed onto the GDC electrolyte confirm good adhesion between the cathode and the GDC electrolyte, which is expected to enhance the thermal compatibility and the long-term thermal stability of the cathode/electrolyte interface. The particle size of all samples are similar except for $x$ = 0.7, where the particles are slightly larger than those of the other samples. Therefore, it is believed that the microstructure of $Pr_{1-x}Sr_xCoO_{3-\delta}$ does not significantly affect the electrochemical characteristics.

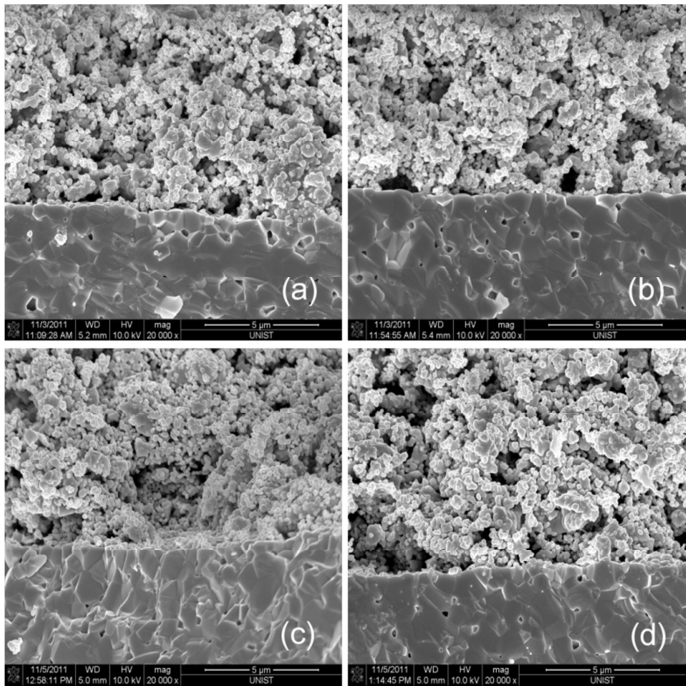


**Fig. 8.** SEM images showing the microstructure of a single cell ($Pr_{1-x}Sr_xCoO_{3-\delta}$-GDC/GDC/Ni-GDC): (a) $x = 0.1$, (b) $x = 0.3$, (c) $x = 0.5$, (d) $x = 0.7$.

Thermogravimetric analysis (TGA) data of $Pr_{1-x}Sr_xCoO_{3-\delta}$ are shown in Fig. 9. The TGA data describe the tendency of oxygen nonstoichiometry (vacancy concentration) of $Pr_{1-x}Sr_xCoO_{3-\delta}$. All samples initiate a weight change at approximately 300 °C. The magnitude of the weight change, indicating a loss of oxygen from the lattice in $Pr_{1-x}Sr_xCoO_{3-\delta}$, decreases in the order of $x = 0.7 > 0.5 > 0.1 > 0.3$. This oxygen vacancy formation can be associated with Co reduction due to the charge compensation mechanism.

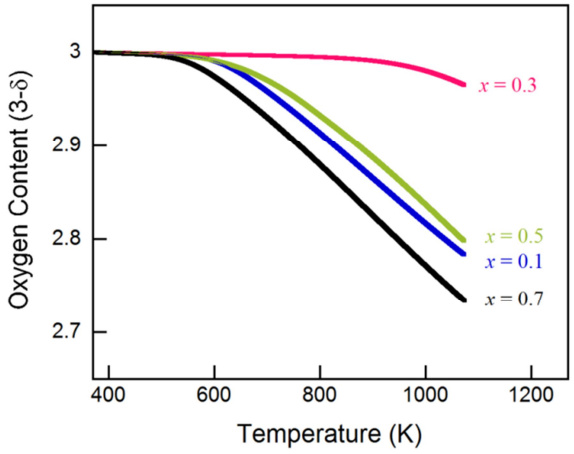


**Fig. 9.** Thermogravimetric data of $Pr_{1-x}Sr_xCoO_{3-\delta}$ ($x = 0.1$, 0.3, 0.5, and 0.7) showing the variation of oxygen content as a function of temperature in air.

The electrical conductivities of the $Pr_{1-x}Sr_xCoO_{3-\delta}$ are described by an Arrhenius plot in Fig. 10. All samples show decreased electrical conductivities with increasing temperature, indicating metallic

behavior. At higher temperatures (> 400 °C), the electrical conductivities for all samples decrease significantly with temperature; this could be due to the loss of oxygen from the lattice, as indicated by the TGA data, and a consequent decrease in the $Co^{4+}$ charge carrier concentration. As can be seen, the electrical conductivity of the sample with $x = 0.3$ reaches a maximum with a value of 2000 S $cm^{-1}$ at 700 °C in air. Therefore, in $Pr_{1-x}Sr_xCoO_{3-\delta}$, the electrical conductivity increases with the amount of strontium doping for $x \leq 0.3$ but decreases for $x > 0.3$.

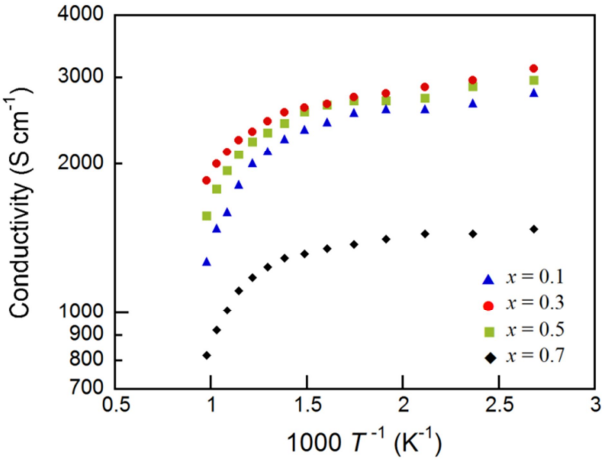


**Fig. 10.** Electrical conductivities of $Pr_{1-x}Sr_xCoO_{3-\delta}$ ($x$ = 0.1, 0.3, 0.5, and 0.7) in air as a function of temperature.

The replacement of $Pr^{3+}$ by $Sr^{2+}$ in $Pr_{1-x}Sr_xCoO_{3-\delta}$ destroys the electro-neutrality, which is mostly compensated by oxidation of $Co^{3+}$ to $Co^{4+}$ (electronic compensation) and/or the formation of oxide ion vacancies (ionic compensation).[11] Generally, the electronic compensation mechanism is dominant at high oxygen partial pressures and low temperatures while the ionic compensation mechanism conversely dominates at low oxygen partial pressures and high temperatures. The increased conductivity with increasing Sr ($Sr^{2+}$) content for $x \leq 0.3$ can be explained by the fact that the formation of $Co^{4+}$ ions prevails over the formation of oxygen vacancies to compensate the electro-neutrality. In contrast, the decreased conductivity with increasing Sr content for $x > 0.3$ indicates that the ionic compensation is dominant compared to electronic compensation. The overall electro neutrality condition can be explained by the following simplified equation:

$$[Sr'_{Pr}] = [Co^{\bullet}_{Co}] + 2[V^{\bullet\bullet}_{o}]$$

Petrov's group[23], using iodometric titration, reported that the concentration of $Co^{4+}$ in a $La_{1-x}Sr_xCoO_{3-\delta}$ system is increased with $x$, reaches a maximum at $x = 0.4$, and then decreases. In other words, the electro-neutrality is accommodated primarily by the ionic mechanism at higher doping levels ($x > 0.4$). These ionic and electronic mechanisms could be distinguished by the oxidation state of cobalt and the oxygen content.

Coulometric titration is used to examine the dependence of the oxygen deficiency of $Pr_{1-}$

$_x$Sr$_x$CoO$_{3-\delta}$ as a function of $p$(O$_2$) at 700 °C.[24] The oxygen non-stoichiometry of Pr$_{1-x}$Sr$_x$CoO$_{3-\delta}$ in Fig. 11 (a) is obtained as a function of $p$(O$_2$) at 700 °C by coulometric titration in order to characterize the redox properties. The initial oxygen content of all samples is determined as 3.0 by TGA in air at room temperature, as shown in Fig. 11 (a). The isotherms of Pr$_{1-x}$Sr$_x$CoO$_{3-\delta}$ have similar shapes, implying that they have nearly equivalent reduction mechanisms. All samples begin to decay at $10^{-4}$ atm and decomposition occurs at around $10^{-5}$ atm. The sample of $x$ = 0.5 starts to show reduction at lower $p$(O$_2$) than the other samples, and it is concluded that Pr$_{0.5}$Sr$_{0.5}$CoO$_{3-\delta}$ shows the best redox stability among Pr$_{1-x}$Sr$_x$CoO$_{3-\delta}$ series. Therefore, redox isotherm data in this study, Pr$_{1-x}$Sr$_x$CoO$_{3-\delta}$ operating at $10^{-5}$ atm at 700 °C might undergo steep oxygen non-stoichiometry gradients and corresponding structural instability.

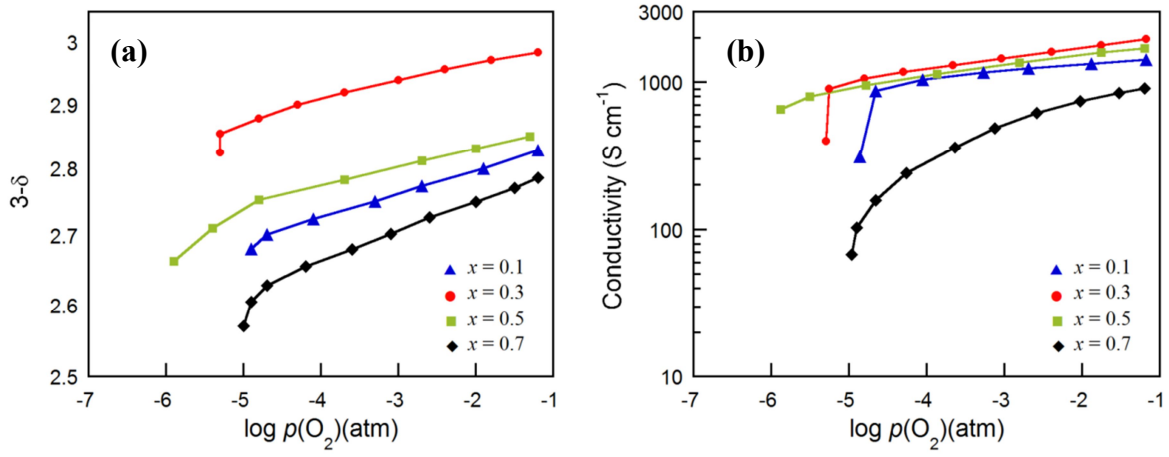


**Fig. 11.** (a) Oxygen non-stoichiometry of Pr$_{1-x}$Sr$_x$CoO$_{3-\delta}$ ($x$ = 0.1, 0.3, 0.5, and 0.7) at 700 °C by coulometric titration. (b) Electrical conductivities of Pr$_{1-x}$Sr$_x$CoO$_{3-\delta}$ ($x$ = 0.1, 0.3, 0.5, and 0.7) under various $p$(O$_2$) (atm) at 700 °C.

The 4-probe electrical conductivities of Pr$_{1-x}$Sr$_x$CoO$_{3-\delta}$ depending on the $p$(O$_2$) at 700 °C are presented in Fig. 11 (b). The electrical conductivities increase with $p$(O$_2$) in all cases, indicating that this material is a $p$-type electronic conductor under the present experimental conditions. The conductivities range from about 900 to 2000 S cm$^{-1}$ at 700 °C, which is sufficiently high for the IT-SOFC operating temperature. However, the electrical conductivities of Pr$_{1-x}$Sr$_x$CoO$_{3-\delta}$ significantly decrease at a $p$(O$_2$) of approximately $10^{-6}$-$10^{-5}$ atm at 700 °C. This suggests that the electrical properties are closely related with the decomposition of the material, which can be speculated from the oxygen non-stoichiometry in the isotherm data.

The electrochemical performances of the Pr$_{1-x}$Sr$_x$CoO$_{3-\delta}$ using a Ni-GDC anode supported cells are presented in Fig. 12 with humidified H$_2$ (3% H$_2$O) as a fuel and static ambient air as an oxidant in a temperature range of 500 ~ 700 °C. The OCV for all samples is approximately 0.8 V at 700 °C and increases with decreasing temperature. Generally, high oxygen vacancy concentration in a perovsikte

type leads to an increase in the kinetics of oxygen exchange and diffusion of oxide ions in cathode materials, which in turn results in increased electrochemical performance.[18] The electrochemical performance trend of $Pr_{1-x}Sr_xCoO_{3-\delta}$, however, follows that of the electrical conductivity instead of the concentration of oxygen vacancy. Therefore, the effect of electronic charge compensation might overwhelm the oxygen ionic compensation. The maximum power density is 1.19 W $cm^{-2}$ for $x = 0.3$ at 700 °C. The other samples also show excellent power density, 1.16, 1.05, 0.92 W $cm^{-2}$ for $x = 0.5$, 0.1, and 0.7, respectively.

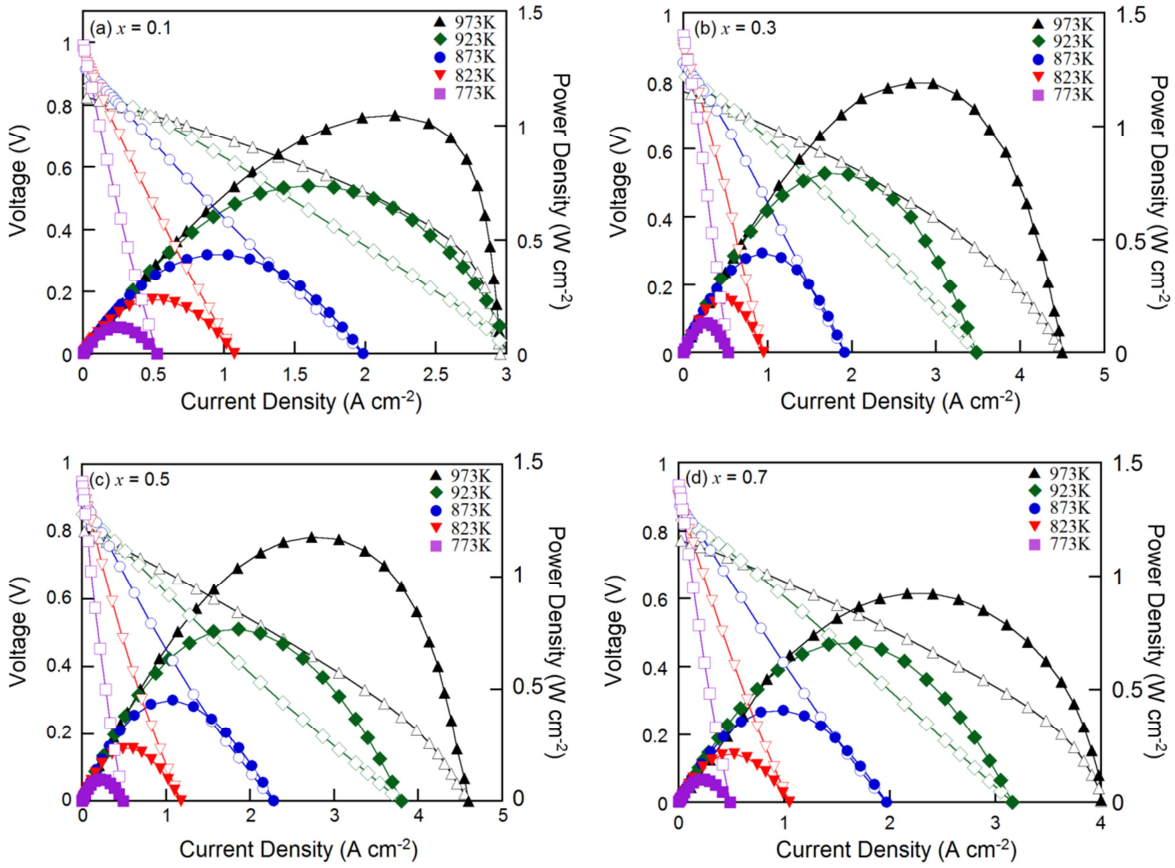


**Fig. 12.** *I-V* curves and corresponding power density curves of a single cell ($Pr_{1-x}Sr_xCoO_{3-\delta}$-GDC /GDC/Ni-GDC) under various temperatures: (a) $x = 0.1$, (b) $x = 0.3$, (c) $x = 0.5$, (d) $x = 0.7$.

The corresponding impedance spectra of $Pr_{1-x}Sr_xCoO_{3-\delta}$-GDC /GDC/Ni-GDC at 650 °C are illustrated in Fig. 13. In these spectra, the intercepts with the real axis at low frequency indicate the total resistance of the cell, and the value at high frequency is the ohmic resistance of the cell. The variation between the two values on the real axis indicates the sum of electrode-electrolyte interface resistance and electrode reactions, which is identified as the non-ohmic resistance of the cell.[25] The increase in operating temperature results in a considerable reduction of the non-ohmic resistance due to the faster oxygen reduction kinetics at higher temperatures. The minimum non-ohmic resistance is 0.023 Ω $cm^2$ at 700 °C for $x = 0.3$, *i.e.*, $Pr_{0.7}Sr_{0.3}CoO_{3-\delta}$.

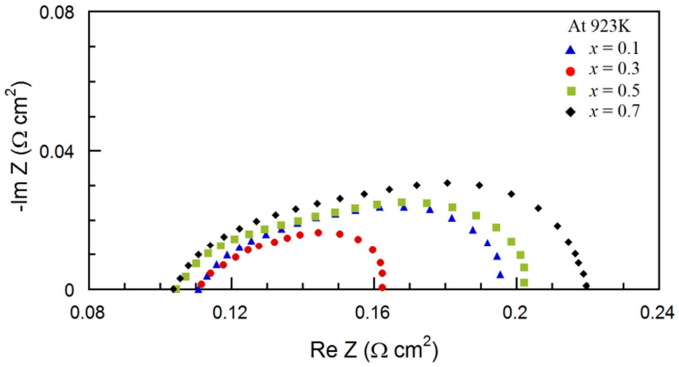


**Fig. 13.** Impedance spectra of the single cell ($Pr_{1-x}Sr_xCoO_{3-\delta}$-GDC/GDC/Ni-GDC) measured under OCV using $H_2$ as fuel and ambient air as oxidant at 650 $^oC$.

### 3.1.3. Conclusions

$Pr_{1-x}Sr_xCoO_{3-\delta}$ ($x$ = 0.1, 0.3, 0.5, and 0.7) perovskite oxides have been studied as a cathode material for IT-SOFCs. The $Pr_{1-x}Sr_xCoO_{3-\delta}$ powders are prepared by the Pechini method and the glycine-nitrate-process (GNP) method. The electrical conductivity of $Pr_{1-x}Sr_xCoO_{3-\delta}$ measured by a four-terminal DC arrangement increases with increasing Sr content but decreases at a high Sr doping range ($x$ > 0.3) in air. For the samples with $x$ = 0.1 and 0.3, $Co^{4+}$ ions, which indicate the formation of electronic holes, maintain the electro-neutrality dominantly with strontium addition and result in higher electrical conductivity. On the other hand, the decreased electrical conductivity with higher Sr content for $x$ > 0.3 is mostly caused by the formation of oxygen vacancies and a consequently decreased amount of $Co^{4+}$ ions. The redox properties of $Pr_{1-x}Sr_xCoO_{3-\delta}$ are evaluated by coulometric titration, and electrical conductivity depending on $p(O_2)$ is measured simultaneously. All samples show similar isotherm shapes and start to decompose at around $10^{-5}$ atm at 700 $^oC$. The sample of $x$ = 0.5 shows reduction at lower $p(O_2)$ than the other samples (at approximately $10^{-6}$ atm). The electrical performances of $Pr_{1-x}Sr_xCoO_{3-\delta}$ are evaluated using an anode-supported cell based on a GDC electrolyte with humidified $H_2$ (3% $H_2O$). The maximum power density is 1.19 W $cm^{-2}$ for $x$ = 0.3 at 700 $^oC$. The other samples also show good performance above 1.0 W $cm^{-2}$, except for $x$ = 0.7. These results are explained by the higher electrical conductivity of the $Pr_{0.7}Sr_{0.3}CoO_{3-\delta}$, possibly due to the higher concentration of holes caused by electronic compensation rather than ionic compensation. Therefore, $Pr_{0.7}Sr_{0.3}CoO_{3-\delta}$ is a more suitable candidate cathode material for IT-SOFCs in terms of electrical conductivity and electrochemical performance.

**References**


1. Z. P. Shao, S. M. Haile, J. Ahn, P. D. Ronney, Z. L. Zhan, S. A. Barnett, *Nature* 435 (2005) 795-798.
2. A. J. Jacobson, *Chem. Mater.* **22** (2010) 660.
3. B. C. H. Steele, A. Heinzel, *Nature* **414** (2001) 345.
4. S. D. Park, J. M. Vohs, R. J. Gorte, *Nature* **404** (2000) 265.
5. S. H. Choi, J. Y. Shin, G. Kim, *J. Power Sources* **201** (2012) 10.
6. W. Zhou, R. Ran, Z. Shao, *J. Power Sources* **192** (2009) 231.
7. J. Peña-Martínez, D. Marrero-López, D. Pérez-Coll, J. C. Ruiz-Morales, P. Núñez, *Electrochim. Acta* **52** (2007) 2950.
8. J. Wan, J. B. Goodenough, J. H. Zhu. *Solid State Ionics* **178** (2007) 281.
9. Z. Shao, S. M. Haile, *Nature* **431** (2004) 170.
10. J. M. Ralph, C. Rossignol, R. Kumar, *J. Electrochem. Soc.* **150** (2003) A1518.
11. K. T. Lee, A. Manthiram, J. Electrochem. Soc. **152(1)** (2005) A197.
12. S. H. Choi, S. Yoo, J. Y. Shin, G. Kim, *J. Electrochem. Soc.* **158(8)** (2011) B995.
13. Y. Guo, H. Shi, R. Ran, Z. Shao, *Int. J. Hydrogen Energy* **34** (2009) 9496.
14. S.W. Baek , J. Bae , Y. S. Yoo, *J. Power Sources* **193** (2009) 431.
15. M. Koyama , C. J. Wen , T. Masuyama, J. Otomo , H. Fukunaga , K. Yamada , K. Eguchi , H. Takahashi, *J. Electrochem. Soc.* **148** (2001) A795.
16. Y. L. Yang, C. L. Chen, S. Y. Chen, C. W. Chu, A. J. Jacobson, *J. Electrochem. Soc.* 147 (2000) 4001.
17. S. B. Adler, J. A. Lane, B. C. H. Steele, *J. Electrochem. Soc.* **143** (1996) 3554.
18. K. T. Lee, A. Manthiram, *J. Electrochem. Soc.* **153(4)** (2006) A794.
19. L. Dieterle, D. Bach, R. Schneider, H. Störmer, D. Gerthsen, U. Guntow, E. Ivers-Tiffée, A. Weber, C. Peters, H. Yokokawa. *J. Mater. Sci.* **43** (2008) 3135.
20. G. C. Kostogloudis, N. Vasilakos, C. Ftikos, *Solid State Ionics* **106** (1998) 207.
21. M. Andersson, J. Yuan, B. Sunden, *J. Appl. Energy* **87** (2010) 1461.
22. J. H. Nam, D. H. Jeon, *Electrochim. Acta* **51** (2006) 3446.
23. A. N. Petrov, O. F. Kononchuk, A. V. Andreev, V. A. Cherepanov, P. Kofstad, *Solid State Ionics* **80** (1995) 189.
24. S. Sengodan, J. H. Kim, J. Y. Shin, G. Kim, *J. Electrochem. Soc.* **158(11)** (2011) B1373.
25. S. Adler, J. A. Lane, B. C. H. Steele, *J. Electrochem. Soc.* **143** (1996) 3554.

### 3.2. Strontium Doping Effect on high-performance $PrBa_{1-x}Sr_xCo_2O_{5+\delta}$ as a cathode material for IT-SOFCs

Layered perovskite-type oxides have received extensive attention as a promising cathode material because of their faster diffusion coefficient and transport kinetics of oxygen even at low temperature (300~500°C) compared to those of perovskite-type oxides. This study focuses on the strontium effect in $PrBa_{1-x}Sr_xCo_2O_{5+\delta}$ ($x$ = 0, 0.25, 0.5, 0.75, and 1.0) oxides by investigating their structural characteristics, electrical properties, and electrochemical performance. The electrical conductivities increase with increasing strontium content owing to the higher coordination number and oxygen content due to the smaller size difference between $Pr^{3+}$ and $Sr^{2+}$. The area specific resistances (ASRs) of $PrBa_{1-x}Sr_xCo_2O_{5+\delta}$ are measured on $Ce_{0.9}Gd_{0.1}O_{1.95}$ (GDC) and the minimum ASR values are observed at $x$ = 0.5 and 0.75. We also investigate the electrochemical performance of a $PrBa_{1-x}Sr_xCo_2O_{5+\delta}$ cathode material using a Ni-GDC anode-supported cell. The maximum power density is 1.08 W $cm^{-2}$ at 600°C for $x$ = 0.5 and 0.75. The other samples also show high power density over 0.9 W $cm^{-2}$ at 600°C, but with a sudden drop at $x$ = 1.0. The structure of $x$ = 1.0 suddenly changes to a perovskite according to the Rietveld refinement, which could affect electrical properties and electrochemical performance.

#### 3.2.1. Introduction

Fuel cells are gaining increasing recognition as a source of low-emission power generation. Solid oxide fuel cells (SOFCs) are considered promising energy conversion devices, offering an environmentally-friendly process, excellent fuel flexibility, and high efficiency among various fuel cells. Despite their many advantages, they require high operating temperature (>1000°C), which causes degradation of cell components resulting from high temperature oxidation, corrosion, chemical inter-diffusion and reaction, and structural failure.[1-4] As a solution to this problem, intermediate temperature solid oxide fuel cells (IT-SOFCs) operating in a temperature range of 500~700°C have been introduced, providing attractive properties such as high oxygen ion diffusivity and a high surface exchange coefficient.[5] The main obstacle impeding practical use of IT-SOFCs is the poor activity of traditional cathode materials for electrochemical reduction of oxygen. Therefore, the development of a new cathode material with high electro-catalytic activity could be a major step toward the commercialization of IT-SOFCs.

The perovskite oxides, particularly mixed ionic/electronic conductors (MIECs) containing Mn, Fe, Co, and/or Ni, have been extensively investigated as IT-SOFC cathode materials. Cobalt containing oxides such as $Ba_{0.5}Sr_{0.5}Co_{0.8}Fe_{0.2}O_{3-\delta}$, $Pr_{1-x}Sr_xCoO_3$, $Sm_{0.5}Sr_{0.5}CoO_3$, $La_{1-x}Sr_xCo_{1-y}Fe_yO_{3-\delta}$, and $Ba_{0.6}La_{0.4}CoO_3$ have attracted much interest due to their high electro-catalytic activity for the oxygen reduction reaction (ORR) at the cathode.[5-11] Recently, many researchers have focused on

layered perovskite oxides based on their much higher chemical diffusion and surface exchange coefficient relative to those of $ABO_3$-type perovskite oxides. The layered perovskite oxides can be attributed with the general formula $AA'B_2O_{5+\delta}$, with the A-site being a rare earth element, the A′ site an alkaline earth element, and the B-site a transition element. These oxides consist of sequential layers $[BO_2]$-[AO]-$[BO_2]$-[A′O] stacked along the *c*-axis.[12] This layered structure reduces the oxygen bonding strength in the [AO] layer and provides a disorder-free channel for ion motion, which enhances oxygen diffusivity.[13]

Based on these promising properties, several groups have studied the layered perovskite oxide $LnBaCo_2O_{5+\delta}$ (LnBCo) (Ln=La, Pr, Nd, Sm, Gd, and Y) and demonstrated their potential for application as IT-SOFC cathode materials.[14-23] Kim et. al.[15] reported that $PrBaCo_2O_{5+\delta}$ has unusually rapid oxygen ion diffusion and surface exchange kinetics even at low temperature (300~500$^oC$). These properties are related to the very low ASR values of electrodes. This compound can be theoretically described with the stacking sequence … $|BaO|CoO_2|PrO_x|CoO_2$… ; when $x < 1$, ordered A-cations localizing oxygen vacancies appear within the rare earth layers.[24]

Some researchers have investigated strontium doped $AA'B_2O_{5+\delta}$ with partial substitution of the A′ site by strontium, which could potentially improve the conductivity of layered perovskite oxides with good aspects of $LnBaCo_2O_{5+\delta}$ oxides.[11,25-28] These studies, however, focused on only the composition of $x = 0.5$ in $PrBa_{1-x}Sr_xCo_2O_{5+\delta}$ and did not provide a systematic investigation of the strontium effect. Therefore, the present work focuses on the effects of strontium doping on the electrical properties and electrochemical performances of $PrBa_{1-x}Sr_xCo_2O_{5+\delta}$ ($x$ = 0, 0.25, 0.5, 0.75, and 1.0) in terms of its application as an IT-SOFC cathode material.

### 3.2.2. Results and Discussion

The XRD patterns of $PrBa_{1-x}Sr_xCo_2O_{5+\delta}$ are presented in Fig. 14 and structural data are given in Table 3. The samples for $x \leq 0.75$ in $PrBa_{1-x}Sr_xCo_2O_{5+\delta}$ exhibit a pure layered perovskite phase. The peaks at $x = 0.5$ and 0.75 reflect a tetragonal perovskite structure, suggesting ordering between $Pr^{3+}$ and $Ba^{2+}$ ions along the *c*-axis, whereas the samples for $x < 0.5$ show an orthorhombic lattice geometry.[29,30] The reflection of $x = 1.0$ sample, however, changes to an $ABO_3$-type perovskite structure with the space group *Pbnm*. The unit cell volume indicated in Table 3 decreases with increasing strontium content in $PrBa_{1-x}Sr_xCo_2O_{5+\delta}$ due to the substitution of smaller $Sr^{2+}$ for $Ba^{2+}$. As a result of refinement, the experimental XRD data, calculated profile, and the difference between the experimental and calculated profiles are presented in Fig. 15 for $x = 0.5$.

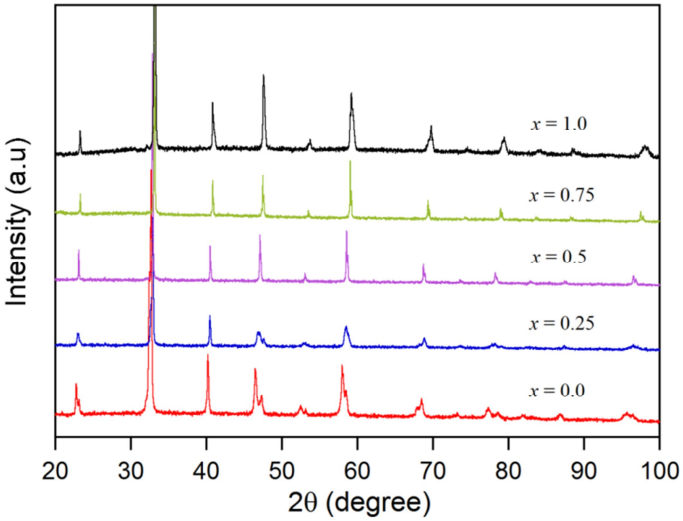


**Fig. 14.** X-ray diffraction patterns of $PrBa_{1-x}Sr_xCo_2O_{5+\delta}$ ($x$ = 0, 0.25, 0.5, 0.75, and 1.0) sintered at1100$^{o}$C for 12h.

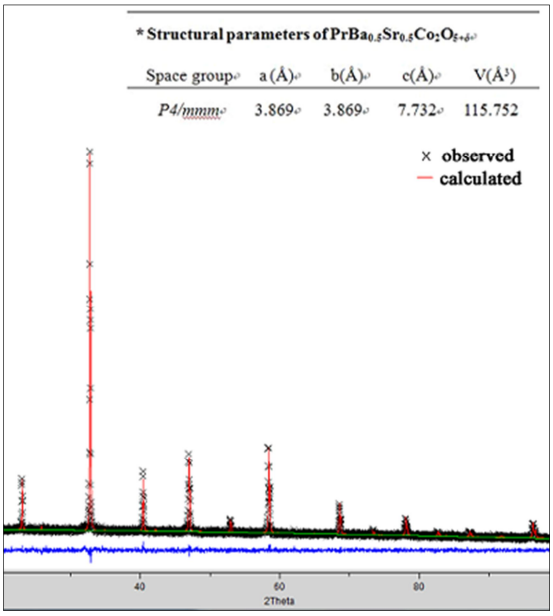


**Fig. 15.** XRD pattern, calculated profile, peak position and the difference between observed and calculated profiles for the $PrBa_{0.5}Sr_{0.5}Co_2O_{5+\delta}$.

**Table 3.** Structural parameters and chemical analysis data of $PrBa_{1-x}Sr_xCo_2O_{5+\delta}$

| $x$ | Space group | a (Å) | b(Å) | c(Å) | V(Å$^3$) | Oxygen content (5+δ) | Oxidation state of Co |
|---|---|---|---|---|---|---|---|
| 0.0 | *Pmmm* | 3.915 | 3.902 | 7.699 | 117.631 | 5.78 | 3.28 |
| 0.25 | *Pmmm* | 3.897 | 3.879 | 7.682 | 116.126 | 5.79 | 3.29 |

| | | | | | | | |
|---|---|---|---|---|---|---|---|
| 0.5 | *P4/mmm* | 3.869 | 3.869 | 7.732 | 115.752 | 5.84 | 3.34 |
| 0.75 | *P4/mmm* | 3.842 | 3.842 | 7.677 | 113.271 | 5.90 | 3.40 |
| 1.0 | *Pbnm* | 5.437 | 5.403 | 7.642 | 112.246 | 6.00 | 3.50 |

**Table 4.** Ionic-radii of the lanthanide and alkaline earth ions.

| Ion | Ionic radius (Å) |
|---|---|
| $Ba^{2+}$ | 1.60 |
| $Sr^{2+}$ | 1.44 |
| $Pr^{3+}$ | 1.30 |

In the layered perovskites, the phase reaction between the electrode and the electrolyte could cause the formation of an undesired insulating layer at the interface, which would block oxide-ionic and electronic transport.[31] The reactivity between the $PrBa_{1-x}Sr_xCo_2O_{5+\delta}$ cathode and GDC electrolyte is examined by mixing the corresponding powders in a 6:4 weight ratio followed by calcination at 1000°C for 4h. The corresponding XRD patterns are shown in Fig. 16. All the diffraction patterns could be indexed well based on physical mixtures of $PrBa_{1-x}Sr_xCo_2O_{5+\delta}$ and GDC. No serious reaction is detected in the binary-mixed $PrBa_{1-x}Sr_xCo_2O_{5+\delta}$-GDC upon sintering at 1000°C for 4h.

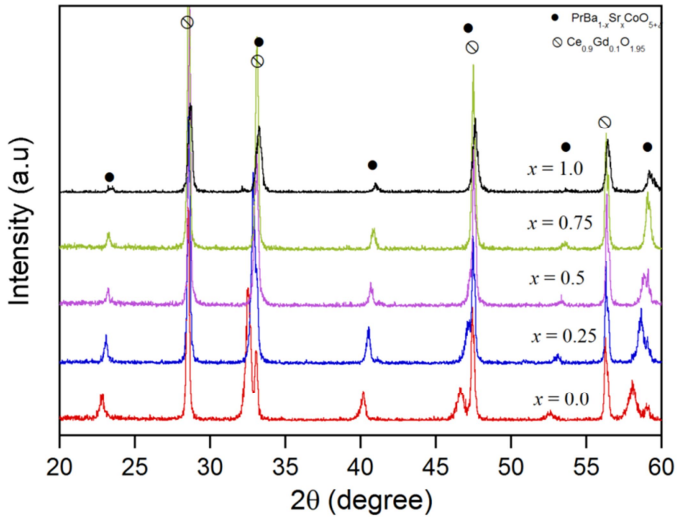


**Figure 16.** X-ray diffraction patterns of $PrBa_{1-x}Sr_xCo_2O_{5+\delta}$-GDC($x$ = 0, 0.25, 0.5, 0.75, and 1.0) sintered at 1000°C for 4h.

The microstructure of the $PrBa_{1-x}Sr_xCo_2O_{5+\delta}$ cathodes is examined by a SEM image, as presented in Fig. 17. The GDC electrolyte with 20 μm thickness adheres very well to the cathode and

anode layer without cracks, indicating good compatibility between the electrolyte and the electrode. The bottom of the micrograph in Fig. 17 (f) indicates a well sintered dense GDC electrolyte and the upper portion shows porous $PrBa_{1-x}Sr_xCo_2O_{5+\delta}$-GDC composite cathodes. The electrode and GDC electrolyte layers are approximately 20 μm in thickness. There is no obvious difference in grain size for all $PrBa_{1-x}Sr_xCo_2O_{5+\delta}$ composite cathodes sintered at 1000°C for 4h.

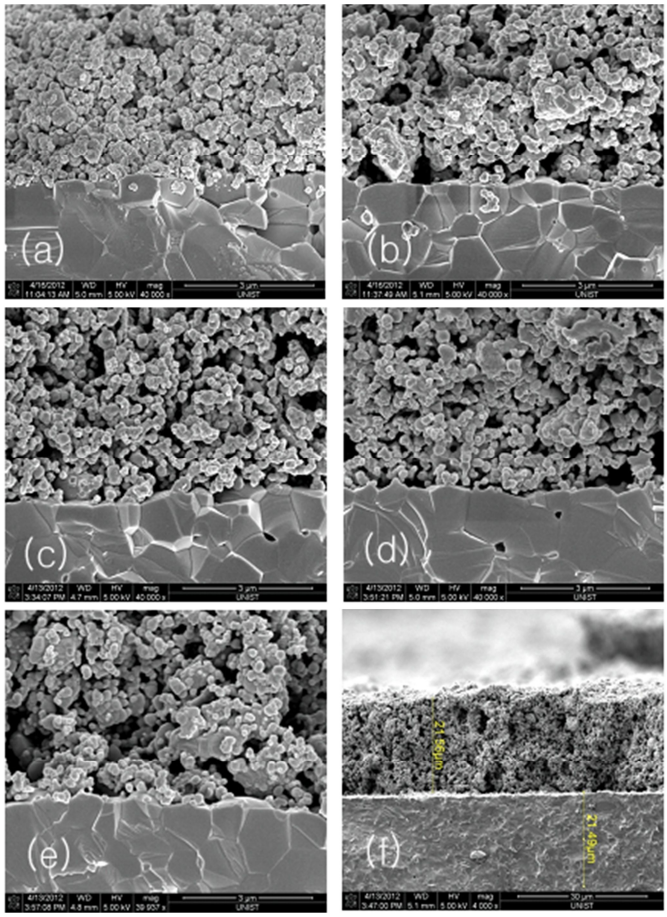


**Fig. 17.** The cross sectional SEM images $PrBa_{1-x}Sr_xCo_2O_{5+\delta}$-GDC cathodes/GDC electrolyte interface: (a) $x$ = 0, (b) $x$ = 0.25, (c) $x$ = 0.5, (d) $x$ = 0.75, (e) $x$ = 1.0, and (f) the cross-section of a single cell with approximately 20μm-thick GDC membrane.

The thermogravimetric data of $PrBa_{1-x}Sr_xCo_2O_{5+\delta}$ in air are illustrated in Fig. 18. The initial room-temperature oxygen contents are determined by iodometric titration. The samples begin to lose oxygen at approximately 200 °C due to the loss of interstitial oxygen from the lattice, as indicated in Fig. 18. The initial oxygen content at room temperature increases with strontium content. A smaller size difference between the $Sr^{2+}$ and $Pr^{3+}$ ions and consequent perturbation of the ordering between the Ba and Pr layers result in increasing coordination number and oxygen content values. [32]

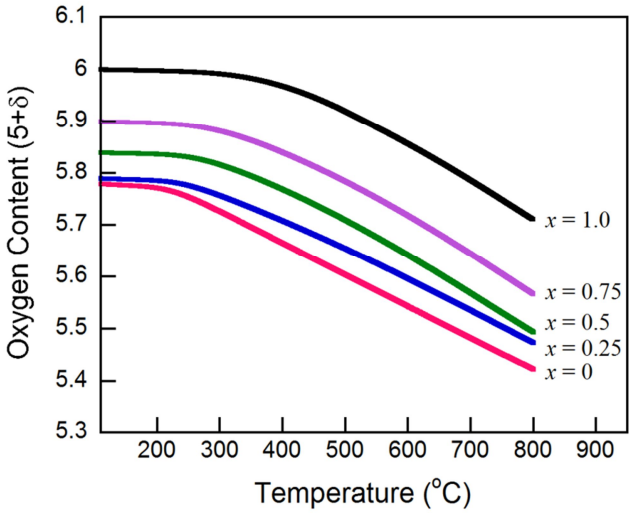


**Fig. 18.** Thermogravimetric data of $PrBa_{1-x}Sr_xCo_2O_{5+\delta}$ ($x$ = 0, 0.25, 0.5, 0.75, and 1.0) showing the variation of oxygen content as a function of temperature in air.

Fig. 19 presents the variation of electrical conductivity with temperature for $PrBa_{1-x}Sr_xCo_2O_{5+\delta}$ samples in air. All samples show a decrease in electrical conductivity with increasing temperature, which is categorized as metallic conduction behavior. They begin to decrease markedly at about 150°C due to such lattice defects breaking the Co-O-Co bonds, resulting in a loss of oxygen atoms from the lattice and reduction of $Co^{4+}$ to $Co^{3+}$.[15,22] The conductivity values of the samples containing strontium are much higher than that of $PrBaCo_2O_{5+\delta}$ and gradually increase with higher strontium content, reaching a maximum at $x$ = 1.0. This is likely due to the increased coordination number and oxygen content values arising from the smaller size difference between the $Sr^{2+}$ and $Pr^{3+}$ ions and consequent ordering between the Ba and Pr layers. The specific ionic-radius values are listed in Table 4.[33] The general required value of electrical conductivity for a cathode material is about 100 S $cm^{-1}$ at the specified operating temperature.[34] The electrical conductivities of $PrBa_{1-x}Sr_xCo_2O_{5+\delta}$ range from 300 to 3000 S $cm^{-1}$ in all temperature regions, which is acceptable for IT-SOFC cathode materials.

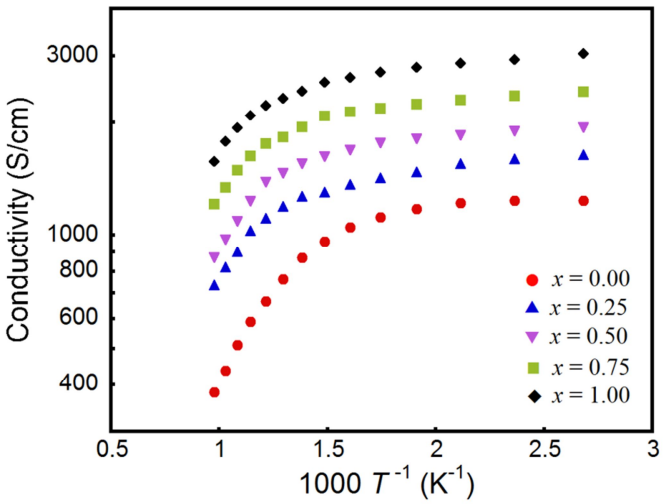


**Fig. 19.** Electrical conductivities of $PrBa_{1-x}Sr_xCo_2O_{5+\delta}$ ($x$ = 0, 0.25, 0.5, 0.75, and 1.0) in air as a function of temperature.

The area specific resistance (ASR) of $PrBa_{1-x}Sr_xCo_2O_{5+\delta}$ is obtained by AC impedance spectroscopy using $PrBa_{1-x}Sr_xCo_2O_{5+\delta}$-GDC/GDC/$PrBa_{1-x}Sr_xCo_2O_{5+\delta}$-GDC symmetrical cells, where the electrolyte is ~ 1.0 mm in thickness. The ASR values are determined by the impedance intercept between high frequency and low frequency with the real axis of the Nyquist plot, and typical impedance spectra are presented in Fig. 20 (a). In these spectra, the intercepts with the real axis at low frequency indicate the total resistance of the single cell, and the intercept at high frequency is the ohmic resistance of the cell. The difference between the two values on the real axis indicates the sum of the electrode-electrolyte interface resistance and the polarization resistance, which is identified as the non-ohmic resistance of the cell.[35] An increase in operating temperature results in a considerable reduction of the ohmic and non-ohmic resistances because of the faster oxygen reduction kinetics. The temperature dependence of the $PrBa_{1-x}Sr_xCoO_{5+\delta}$ ($x$ = 0, 0.25, 0.5, 0.75, and 1.0)-GDC composite cathode polarization is illustrated by an Arrhenius plot in Fig. 20 (c). The minimum ASR value is shown as 0.073 ~ 0.076 Ω cm$^2$ at 600 $^o$C for $x$ = 0.5 and 0.75, which is substantially lower than those presented in earlier reports.[25-28]

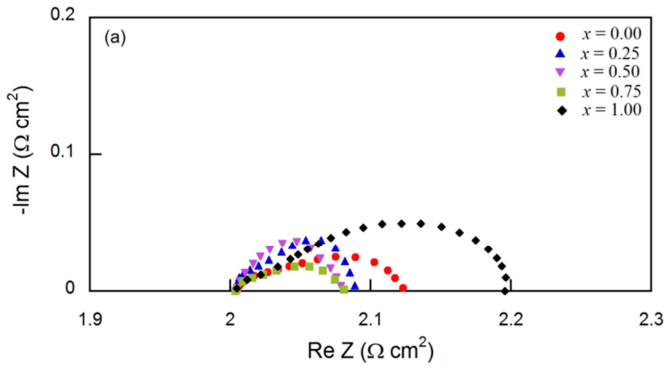

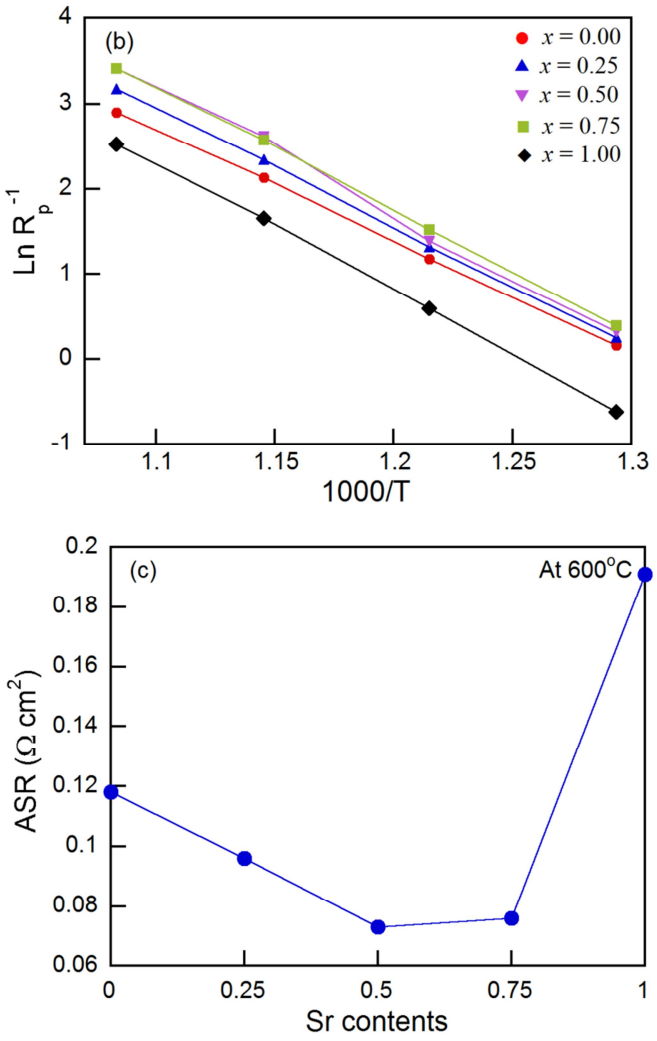


**Fig. 20.** (a) Impedance spectra of $PrBa_{1-x}Sr_xCo_2O_{5+\delta}$ ($x$ = 0, 0.25, 0.5, 0.75, and 1.0)-GDC composite cathodes on GDC symmetrical cells measured at 600°C under OCV. (b) Temperature dependence of the $PrBa_{1-x}Sr_xCo_2O_{5+\delta}$ ($x$ = 0, 0.25, 0.5, 0.75, and 1.0)-GDC composite cathodes polarization conductance by Arrhenius plots. (c) ASRs of $PrBa_{1-x}Sr_xCo_2O_{5+\delta}$ ($x$ = 0, 0.25, 0.5, 0.75, and 1.0)-GDC composite cathodes on GDC electrolyte in symmetrical cells measured at 600°C in air.

Fig. 21 shows the power density and voltage as a function of current density for Ni-GDC/GDC/$PrBa_{1-x}Sr_xCo_2O_{5+\delta}$-GDC cells using humidified $H_2$ (3% $H_2O$) as a fuel and static ambient air as an oxidant in a temperature range of 500~650°C. The fuel cell performances for $x \leq 0.75$ are enhanced with increasing strontium content in $PrBa_{1-x}Sr_xCo_2O_{5+\delta}$ oxides. The maximum power density is about 1.08 W $cm^{-2}$ at both $x$ = 0.5 and 0.75, which is clear evidence of a strontium effect in $PrBa_{1-x}Sr_xCo_2O_{5+\delta}$ layered perovskites. The strontium contents at $x$ = 0.5 and 0.75 in $PrBa_{1-x}Sr_xCo_2O_{5+\delta}$ reflects a tetragonal lattice geometry while an orthorhombic geometry is obtained at $x$ = 0.0 and 0.25 with the layered perovskite structures. Generally, a tetragonal structure exhibits faster oxygen

transport in the bulk and surface and higher catalytic activity for the oxygen reduction reaction as compared to an orthorhombic structure.[15,19,36] The enhanced catalytic activity at $x = 0.5$ and 0.75 could be related to faster oxygen transport compared to that in the other samples. A sudden drop in electrochemical performance, however, is observed at $x = 1.0$ and is ascribed to a structural change to an $ABO_3$-type simple perovskite. This can be explained by much higher chemical diffusion, and the higher surface exchange coefficient of the layered perovskite oxides originates from the reduced oxygen bonding strength in the [AO] layer and a disorder-free channel for ion motion relative to those of $ABO_3$-type perovskite oxides.[13,15]

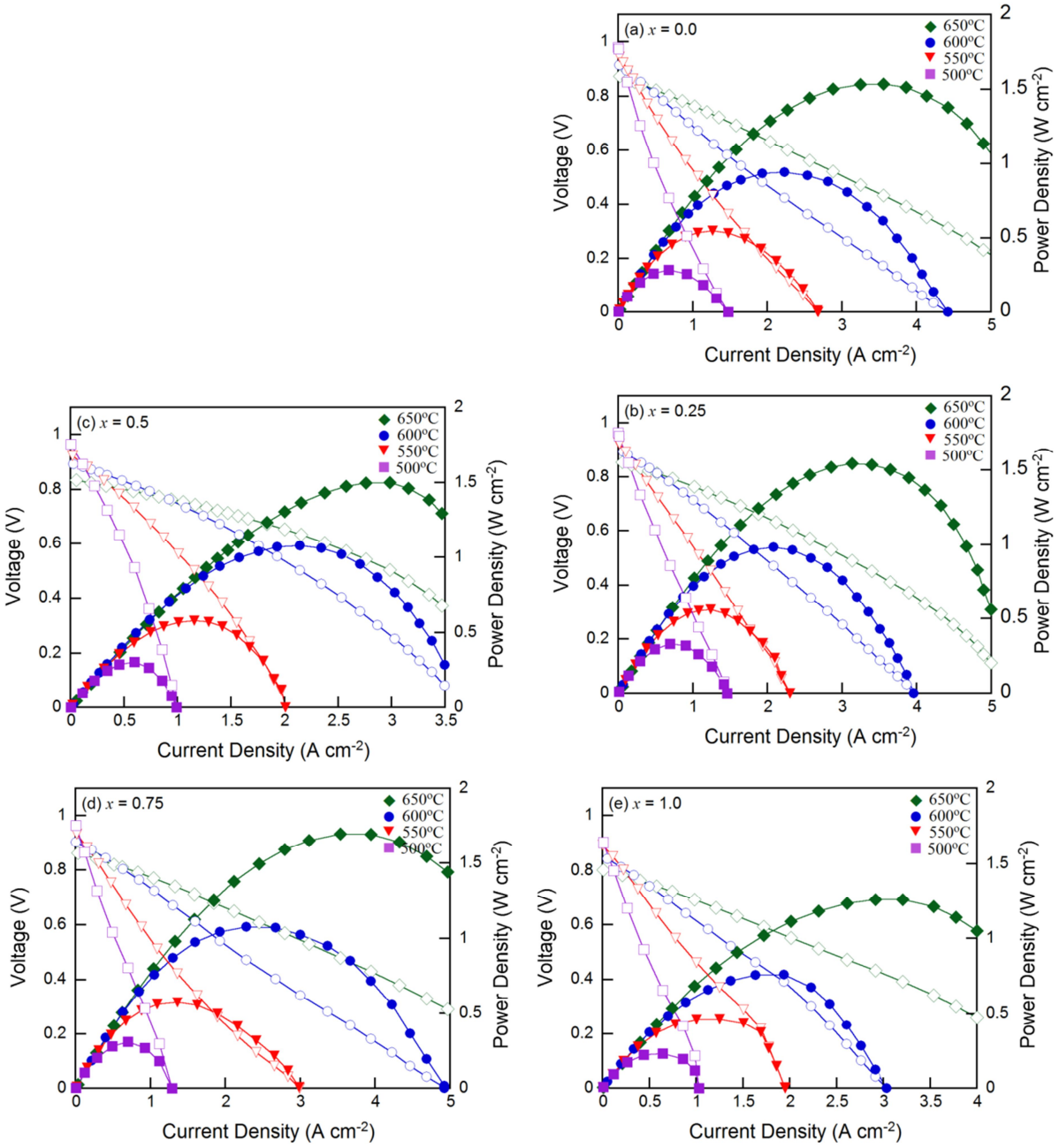

**Fig. 21.** *I-V* curves and corresponding power density curves of a single cell ($PrBa_{1-x}Sr_xCo_2O_{5+\delta}$-GDC /GDC/Ni-GDC) under various temperatures: (a) $x = 0$, (b) $x = 0.25$, (c) $x = 0.5$, (d) $x = 0.75$, and (e) $x = 1.0$.

### 3.2.3. Conclusion

$PrBa_{1-x}Sr_xCo_2O_{5+\delta}$ ($x$ = 0, 0.25, 0.5, 0.75 and 1.0) oxides are considered a promising cathode material for IT-SOFCs. $PrBa_{1-x}Sr_xCo_2O_{5+\delta}$ powders are prepared by the Pechini method. The electrical conductivities of $PrBa_{1-x}Sr_xCo_2O_{5+\delta}$ in air increase with increasing Sr content because of the higher coordination number and oxygen content followed by the smaller size difference between $Pr^{3+}$ and $Sr^{2+}$.

The area specific resistances based on GDC symmetrical cells decrease with strontium doping in $PrBa_{1-x}Sr_xCo_2O_{5+\delta}$ oxides. The ASR value of $x = 1.0$, however, increases due to its structural change to a simple perovskite system (space group *Pbnm*). The electrochemical performances of $PrBa_{1-x}Sr_xCo_2O_{5+\delta}$ are evaluated using an anode-supported cell based on a GDC electrolyte with humidified $H_2$ (3% $H_2O$). The maximum power density is approximately 1.08 W $cm^{-2}$ for $x = 0.5$ and 0.75 at 600°C. The other samples also show good performance of almost 1.0 W $cm^{-2}$, except for $x = 1.0$, where the performance is 0.73 W $cm^{-2}$. The maximum power density might be explained by the high electrical conductivity, fast oxygen transport in the bulk and surface, and high catalytic activity for the ORR. Therefore, the samples with $x = 0.5$ and 0.75 in $PrBa_{1-x}Sr_xCo_2O_{5+\delta}$ oxides are more suitable cathode candidate materials for IT-SOFCs in terms of electrochemical performance.

**References**


1. Y. H. Huang, R. I. Dass, Z. L. Xing, J. B. Goodenough, *Science* **312** (2006)254.
2. B.C.H.Steele, A. Heinzel, *Nature* **414** (2001)345.
3. S. D. Park, J. M. Vohs, and R. J. Gorte, *Nature* **404** (2000)265.
4. Z. P. Shao, S. M. Haile, J. Ahn, P. D. Ronney, Z. L. Zhan, and S. A. Barnett, *Nature* **435** (2005) 795.
5. Z. P. Shao, S. M. Haile, *Nature* **431** (2004) 170.
6. S. H. Park, S. H. Choi, J. Y. Shin, G. Kim, *J. Power Sources* **210** (2012)172.
7. X. Y. Xu, C. R. Zia, S. G. Huang, D. K. Peng, *Ceram. Int*. **31** ( 2001)1060.
8. S. Souza, S. J. Bisco, L. C. Jonghe, *J. Electrochem. Soc.* **144** (1997) L35.
9. O. Buchler, J. M. Serra, W. A. Meulenberg, D. Sebold, H. P. Buchkremer, *Solid State Ionics* **178** (2007) 91.
10. T. Ishihara, S. Fukui, H. Nishiguchi, Y. Takita, *J. Electrochem. Soc*. **149** (2002) A823.
11. J. H. Kim, M. Cassidy, J. T. S. Irvine, J. Bae, *Chem.Mater.*, **22** (2010) 883.
12. D. J. Chen, R. Ran, K. Zhang, J. Wang, Z. P. Shao, *J. Power Sources* **188** (2009) 96.
13. A. A Taskin, A. N. Lavrov, Y. Ando, *Progress in Solid State Chem.* **35** (2007) 481.
14. A. M. Chang, S. J. Skinner, J. A. Kilner, *Solid State Ionics* **177** (2006) 2009.
15. G. Kim, S. Wang, A. J. Jacobson, L. Reimus, P. Brodersen, C. A. Mims, *J. Mater Chem.* **17** (2007) 2500.
16. A. Tarancon, S. J. Skinner, R. J. Chater, F. H. Ramirez, J. A. Kilner, *J. Mater. Chem.* **17** (2007) 3175.
17. A. Tarancon, A. Morata, G. Dezanneau, S. J. Skinner, J. A. Kilner, S. Estrade, F. H. Ramirez, F. Peiro, J. R. Morante, *J. Power Sources*, **174** (2007) 255.
18. N. Li, Z. Lu, B. Wei, X. Q. Huang, K. F. Chen, Y.H. Zhang, W. H. Su, *J. Alloy Compounds* **454** (2008) 274.
19. J. H. Kim, A. Manthiram, *J. Electrochem. Soc.* **155 (4)** (2008) B385.
20. B. Lin, S. Zhang, L. Zhang, L. Bi, H. Ding, X. Liu, J. Gao, G. Meng, *J. Power Sources* **177** (2008) 330.
21. Q. Zhou, T. He, Y. Ji, *J. Power Sources* **185** (2008) 754.
22. K. Zhang, L. Ge, R. Ran, Z. Shao, S. Liu, *Acta Mater.* **56** (2008) 4876.
23. S. H. Choi, J. Y. Shin, G. Kim, *J. Power Sources* **201** (2012) 10.
24. C. Frontera, J. L. G.Munoz, A. Llobet, L. Manosa, M. A. G. Aranda, *J. Solid State Chem*. **171** (2003) 349.
25. F. Zhao, S. Wang, K. Brinkman, F. Chen, *J. Power Sources* **195** (2010) 5468.
26. H. Ding, X. Xue, *Electrochim. Acta* **55** (2010) 3812.

27. S. Lu, G. Long, X. Meng, Y. Ji, B. Lu, H. Zhao, *Int. J. Hydrogen Energy* **37** (2012) 5914.
28. A. K. Azad, J. H. Kim, J. T. S. Irvine, *J. Power Sources* **156** (2009) B682.
29. A. Maignan, C. Martin, D. Pelloquin, N. Nguyen, B. Raveau, *J. Solid State Chem.* **142** (1999) 247.
30. C. Martin, A. Maignan, D. Pelloquin, N. Nguyen, B. Raveau, *Appl. Phys. Lett.* **71** (1997) 1421.
31. C. Rossignol, J. M. Ralph, J. M. Bae, J. T Vaughey, *Solid State Ionics* **175** (2004) 59.
32. J. H. Kim, F. Prado, A. Manthiram, *J. Electrochem. Soc*. **155** (2008) B1023.
33. J. A. Dean (Editor), *Lange's Handbook of Chemistry* ($5^{th}$ edition), McGraw-Hill Inc., New York (1999) pp. 4.30-4.34.
34. E. Boehm, J. M. Bassat, M. C Steil, P. Dordoe, F. Mauvy, J. C. Grenier, *Solid State Society* **5** (2003) 973.
35. S. Adler, J. A. Lane, B. C. H. Steele, *J. Electrochem. Soc.* **143** (1996) 3554.
36. A. Tarankon, S. J. Skinner, R. J. Chater, F. H. Ramirez, J. A. Kilner, *J. Mater. Chem.* **17** (2007) 3175.

### 3.3. A collaborative study of sintering and composite effects for $PrBa_{0.5}Sr_{0.5}Co_{1.5}Fe_{0.5}O_{5+\delta}$ IT-SOFC cathode

Recently, a novel cathode material $PrBa_{0.5}Sr_{0.5}Co_{1.5}Fe_{0.5}O_{5+\delta}$ (PBSCF) has been proposed as a solution to overcome the drawbacks of a conventional cathode for intermediate-temperature solid oxide fuel cells (IT-SOFCs). Here we report systematic procedures to optimize the sintering temperature and the composite for PBSCF as an IT-SOFC cathode. For optimization of the heat treatment conditions for PBSCF composite cathode, the effects of sintering temperature on the microstructure and electrical transport properties of the material are examined. We also suggest the optimization processes to effectively expand the electrochemical reaction zone based on a combination of a mixed ionic and electronic conductor (MIEC) electrode and an ionically conducting phase (PBSCF-$Ce_{0.9}Gd_{0.1}O_{1.95}$ (GDC)$x$, $x$ = 0, 20, 40, 50, and 60 wt%). The optimal intersection point between these two processing systems is revealed to be 50 wt% of GDC containing composite cathode sintered at 950 $^{o}$C for 4 h. The area specific resistance (ASR) of PBSCF-GDC50 sintered at 950 $^{o}$C for 4 h reaches a minimum value of 0.052 Ω cm$^2$ at 600 $^{o}$C, which is consistent with the electrochemical performance results representing peak power density of ~ 2.0 W cm$^{-2}$ at 600 $^{o}$C.

#### 3.3.1. Introduction

Recent interest in a hydrogen-based energy economy has refocused attention on solid oxide fuel cells (SOFCs) as an alternative energy source to fossil fuels. SOFCs are electrochemical energy conversion devices that directly convert the chemical energy in fuel to electricity with high conversion efficiency and low pollution emission.[1-3] Notwithstanding these advantages, the high operating temperature of conventional SOFCs (~ 1000 $^{o}$C) leads to some problems, including material compatibility challenges and high costs. In this respect, recent research has been aimed at developing intermediate temperature SOFCs (IT-SOFCs) operating from 500 to 700 $^{o}$C. However, there are major obstacles to the practical use of IT-SOFCs, including poor oxide-ion conductivity and inadequate catalytic activity of the conventional cathodes stemming from the reduced operating temperature.[4-6] In the field of IT-SOFC research and development, considerable efforts have therefore been invested in the following two areas crucial to the successful performance of IT-SOFCs: enhancing the ionic conductivity of electrolytes and reducing the polarization resistance of electrodes.[7]

These two approaches are frequently adopted to raise the ionic conductivity using alternative electrolytes, such as $Ce_{0.8}Sm_{0.2}O_{1.9}$ (SDC) and $Ce_{0.9}Gd_{0.1}O_{1.95}$ (GDC), as well as the catalytic activity of the cathode.[8,9] One strategy for raising the catalytic activity of the cathode is to utilize mixed ionic and electronic conductivity (MIEC) materials containing Mn, Fe, Co, and/or Ni with perovskite structures, such as $Ba_{0.5}Sr_{0.5}Co_{0.8}Fe_{0.2}O_{3-\delta}$ (BSCF), $Pr_{1-x}Sr_xCoO_3$(PSC) , $Sm_{0.5}Sr_{0.5}CoO_3$(SSC), and $La_{1-x}Sr_xCo_{1-y}Fe_yO_{3-\delta}$ (LSCF).[10-13] These MIEC materials not only possess high oxygen permeability and

electro-catalytic activity but also help extend the three-phase boundary (TPB) to the entire cathode-gas interface, which leads to dramatically improved cathode electrochemical performance.[14,15]

Many groups have recently studied layered perovskite oxides having the general formula $AA'B_2O_{5+\delta}$ because they offer much higher chemical diffusion and surface exchange coefficients relative to those of $ABO_3$-type simple perovskite oxides.[16,17] This layered structure reduces the oxygen bonding strength in the [AO] layer and provides crystalline channels for ion motion, which enhance oxygen ion diffusion and surface oxygen exchange. $LnBaCo_2O_{5+\delta}$ (Ln = La, Pr, Nd, Sm, and Gd) (LnBCO) compounds are well known layered perovskite oxides with high mixed ionic and electronic conductivity and faster oxygen transport, even at temperatures below 500 $^oC$, which afford high catalytic activity for the oxygen reduction reaction (ORR).[18] The high concentration of mobile oxygen species may be responsible for the high diffusivity of oxide ions in the bulk and the enhanced surface activity toward the ORR.[16,19-21] Recently, Choi *et al.* proposed a novel cathode material, $PrBa_{0.5}Sr_{0.5}Co_{1.5}Fe_{0.5}O_{5+\delta}$ (PBSCF).[22] The partial co-substitution of Ba and Co by Sr and Fe, respectively, improves not only electrical conductivity and also chemical and thermal compatibility of the material.[22-28] Particularly, Fe substitution of Co enhances the oxygen ion diffusivity, ORR activity, and stability of the cathodes due to increased 3d metal-oxygen bonding energy and also decreases thermal expansion.[29-31] Accordingly, optimized co-substitution of PBSCF, rather than sole substitution, could lead to synergistic effects with respect to the electrochemical properties and long-term thermal stability of the cathode material.[22]

With the aim of effectively expanding the electrochemical reaction zone, composite cathodes that include a mixture of a cathode and an ionic conducting material, such as PBSCO-GDC, $SmBa_xSr_{1-x}Co_2O_{5+\delta}$ (SBSCO)-GDC, $NdBa_{0.5}Sr_{0.5}Co_2O_{5+\delta}$ (NBSCO)-GDC, SSC-SDC, and $La_{0.5}Sr_{0.5}MnO_3$(LSM)-yttria stabilized zirconia (YSZ),[23,24,28,32,33] have recently gained widespread interest. The combination of an ionically conducting phase and MIEC electrode may boost the electrochemical reaction by providing additional TPB sites for the ORR. Kim *et al.* have reported that a composite cathode consisting of NBSCO and GDC exhibits lower interfacial polarization resistances, as compared with those of pure NBSCO.[24] The authors provide the mechanisms of the ORR for an electronic conducting cathode, MIEC cathode, and MIEC-GDC composite cathode. The electrochemically active areas of composite cathodes can be divided into three pathways: the TPB point where the electrolyte, cathode, and gas are in contact, the 2PB point on the surface of the pure MIEC cathode, and the extended TPB point by the addition of GDC into the cathode.[24]

Sintering is also an important processing parameter that influences microstructure evolution, grain growth, and densification of a material. Generally, sintering at high temperature increases the grain size of an electrode, which in turn decreases the surface area-gas solid interface (TPB), consequently resulting in a high polarization resistance.[34] The electrode particles, however, require

adequate sintering temperature (typically at least 800 °C) to strongly adhere to the electrolyte surface.[35] Therefore, obtaining fine particles of the cathode and proper adhesion to the electrolyte are in a tradeoff relationship with respect to the sintering temperature.

In this work, the optimization processes for heat treatment of PBSCF-GDC50 and proportional addition of GDC to PBSCF (PBSCF-GDC*x*, *x* = 0, 20, 40, 50, and 60 wt %) are systematically investigated to evaluate their potential as cathode materials for IT-SOFCs based on structural characteristics and electrochemical properties of these materials.

### 3.3.2. Results and Discussions

**The effects of sintering temperature variations on microstructure and electrical transport**

Fig.22 shows the XRD patterns of PBSCF-GDC50 obtained after heat treatment at various temperatures from 900 to 1050 °C with 50 °C intervals for 4h in air. Generally, a phase reaction between the electrode and the electrolyte can result in the formation of an undesired insulating layer at the interface, which hinders the oxide-ionic and electronic transport.[36] Therefore, the chemical compatibility between PBSCF and GDC should be investigated as a preliminary study. Fig. 22(a) confirms that a pure layered perovskite phase is obtained with the diffraction peaks indexed in a tetragonal structure (space group *P*4/*mmm*) after heat treatment at 1150 °C for 12 h.[22] For a comparison, the XRD pattern of GDC powder is also presented in Fig. 22 (b). All the peaks presented in Fig. 22 (c) to (f) can be attributed to either PBSCF and GDC, indicating that PBSCF is chemically compatible with GDC under the given circumstances, even at temperatures much higher than IT-SOFC operating temperature (~ 700 °C). Moreover, the peak intensities of PBSCF-GDC50 become more intense and sharp with increasing sintering temperature due to well crystallized phases.[37]

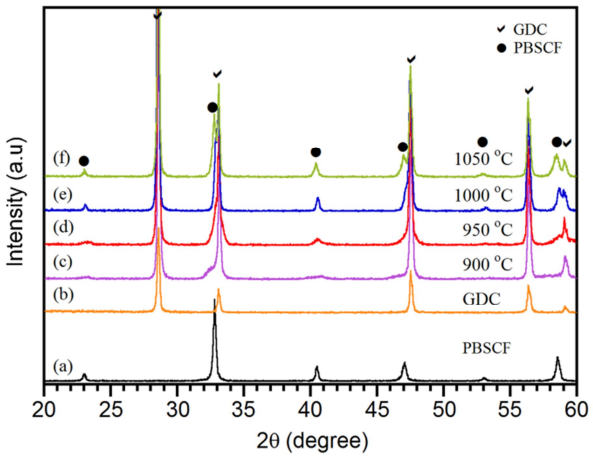


**Fig. 22.** X-ray diffraction patterns of (a) $PrBa_{0.5}Sr_{0.5}Co_{1.5}Fe_{0.5}O_{5+\delta}$ sintered at 1150 °C for 12 h, (b) $Ce_{0.9}Gd_{0.1}O_{1.95}$ (GDC) sintered at 1350 °C for 4 h, and $PrBa_{0.5}Sr_{0.5}Co_{1.5}Fe_{0.5}O_{5+\delta}$-GDC50 sintered at (c) 900 °C, (d) 950 °C, (e) 1000 °C, and (f) 1050 °C for 4h.

Fig. 23 presents SEM images of PBSCF-GDC50 sintered at different temperatures. Fig. 23 (a) indicates that there is an uneven distribution of grains as well as poorer porosity and insufficient adhesion to the GDC electrolyte, likely due to insufficient heat treatment. The powders can be regarded as raw materials that are not fully reacted until 900 $^{o}$C. From Figs. 23 (b) to (d), the progress of grain growth with increasing sintering temperature is observed. The particles are faceted and the size distribution is wider when they are produced at higher temperatures. Fig. 23 (b) reveals homogeneously distributed particles and relatively small grain size with good connectivity between the electrode and electrolyte as well as reasonable porosity, which ensures effective gas diffusion. Figs. 23 (c) and (d) present much larger grain size and agglomerations of particles, possibly due to excessive heat treatment, which may decrease the electrochemically active surface area. These results demonstrate that the microstructure of the PBSCF-GDC50 composite cathode sintered at 950 $^{o}$C for 4h in air can considered optimal.

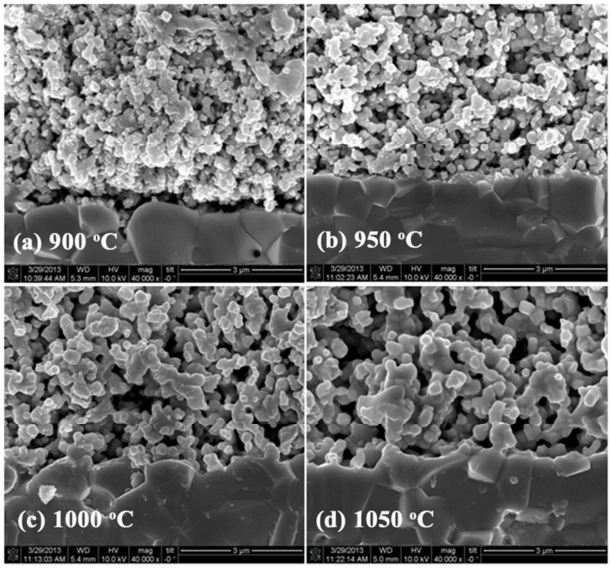


**Fig. 23.** Cross-sectional SEM images of $PrBa_{0.5}Sr_{0.5}Co_{1.5}Fe_{0.5}O_{5+\delta}$-GDC50 cathode/GDC electrolyte interface sintered at (a) 900 $^{o}$C, (b) 950 $^{o}$C, (c) 1000 $^{o}$C, and (d) 1050 $^{o}$C.

To assess the electro-catalytic activity of PBSCF-GDC50 sintered at various temperatures, the impedance spectroscopy of the symmetrical cell was investigated under open circuit voltage (OCV) conditions. For comparison, Nyquist plots of PBSCF-GDC50/GDC/PBSCF-GDC50 sintered at various temperatures are shown in Fig. 24 (a) with the specific area specific resistance (ASR) values at 600 $^{o}$C, defined as ASR = ($R_p$ x 0.36 cm$^2$)/2, provided in the inset. The intercept on the real axis at high frequency corresponds to the ohmic-resistance of the cell ($R_{ohm}$) whereas the low frequency intercept gives the total resistance ($R_{ohm}$+$R_p$). Therefore, the ASR values are determined by the impedance intercept between high frequency and low frequency with the real axis of the Nyquist plot.

The minimum ASR value reaches 0.053 Ω $cm^2$ at 600 °C, obtained from the PBSCF-GDC50 sample sintered at 950 °C, which is much lower value than ASR values of the other samples, as listed in the inset of Fig. 24 (a). These data indicate that PBSCF-GDC50 sintered at 950 °C may have the smallest polarization resistance as well as the best electrochemical performance. One possible origin of the lower ASR value of the material sintered at 950 °C could be micro-structural enhancement, as mentioned above. Over the investigated temperature range, 950 °C can be considered the optimal sintering temperature for the PBSCF-GDC50 composite cathode in terms of microstructure and electro-catalytic activity. The temperature dependence of the polarization resistance for the PBSCF-GDC50 electrode on the GDC electrolyte with various heat treatments is illustrated by an Arrhenius plot in Fig. 24 (b). The apparent Ea values of PBSCF-GDC50 cathodes sintered at different temperatures are also shown in the inset of Fig. 24 (b). The relatively lower Ea value of PBSCF-GDC50 sintered at 950°C may suggest a lower chemical barrier for oxygen reduction compared to that of the other samples, subsequently resulting in high electro-catalytic activity.[38-40]

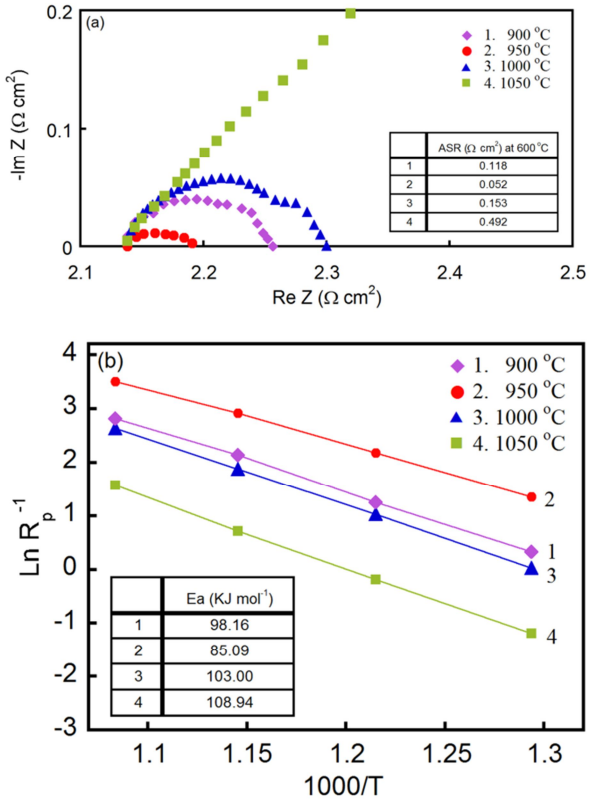


**Fig. 24.** (a) Impedance spectra of $PrBa_{0.5}Sr_{0.5}Co_{1.5}Fe_{0.5}O_{5+\delta}$-GDC50 composite cathodes on GDC symmetrical cells sintered at various temperatures and measured at 600 °C under OCV. (b) Temperature dependence of polarization resistance for $PrBa_{0.5}Sr_{0.5}Co_{1.5}Fe_{0.5}O_{5+\delta}$-GDC50 composite cathodes on GDC electrolyte sintered at various temperatures by Arrhenius plots.

**The effects of GDC variations on micro-structural and electrochemical properties**

Based on the preliminary study to determine the optimal sintering temperature, we present the systematic variation of the GDC ratio in PBSCF to identify optimized two-phase composite cathodes. To further investigate the effects of GDC on the micro-structural properties of PBSCF-GDC*x* (*x* = 0, 20, 40, 50, and 60 wt%) composite cathodes, typical SEM images of PBSCF-GDC*x* are shown in Fig. 25. For a primary powder, with smaller particle size, accordingly larger surface area is obtained, increasing the amount of reactant exposed for the reaction.[34] Larger particles and severe coalescence of powder bonded with grains are observed in Fig. 25 (a). An increase in the amount of GDC, however, gradually mitigates these agglomerations and homogeneously disperses the particles of the PBSCF-GDC*x* electrode. Meanwhile, the composite cathodes containing 40, 50, and 60 wt% of GDC display similar microstructure, showing well-bonded porous networks, which facilitate oxygen transport to the activated the TPB sites. Fig. 25 (f) presents a cross-sectional view of a single cell consisting of Ni-GDC as an anode, GDC as an electrolyte, and a PBSCF-GDC*x* composite cathode sintered at 950 $^{o}$C. The thickness of both the dense GDC electrolyte and the porous cathode of a single cell is approximately 15 μm.

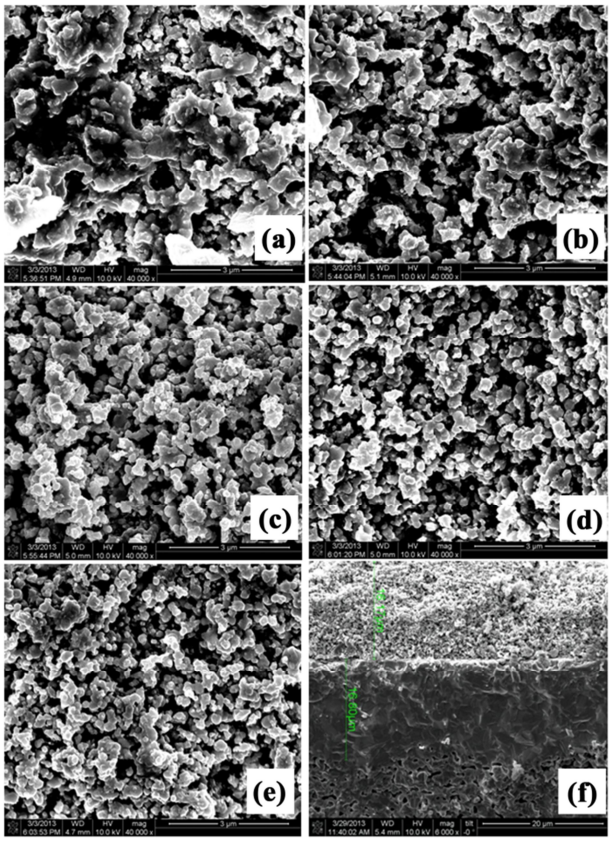


**Fig. 25.** SEM images of $PrBa_{0.5}Sr_{0.5}Co_{2-x}Fe_xO_{5+\delta}$–GDC*x*/GDC/Ni-GDC: (a) *x* = 0 wt%, (b) *x* = 20 wt%, (c) *x* = 40 wt%, (d) *x* = 50 wt%, (e) *x* = 60 wt%, and (f) the cross-section of a single cell with an approximately 15 μm-thick GDC membrane.

The impedance responses on the PBSCF-GDC*x*/GDC/PBSCF-GDC*x* symmetrical cells are characterized by two arcs at high-frequency and low-frequency, indicating that there might be at least two electrode processes which limit the ORR on PBSCF-GDC*x* composite cathodes. Fig. 26 (a) shows the experimental electrochemical impedance spectroscopy patterns at 600 $^{o}$C, simulated with the equivalent circuit model illustrated in the inset of Fig. 26 (a) from 0 to 60 wt% of GDC. The impedance analysis results using the model circuit are also listed in Table 5. The real axis values at the high frequency intercepts, $R_1$, mainly correspond to the electrolyte resistance and wires. In the Nyquist plots, high-frequency arcs are equivalent to $R_2$, which is caused by charge transfer during the migration and diffusion of oxygen ions from the TPB into electrolyte lattice. Meanwhile, low-frequency arcs correspond to $R_3$, which is associated with adsorption/desorption of the molecular oxygen and bulk or surface oxygen diffusion.[15,41] For comparison, the specific values of $R_2$ and $R_3$ are plotted in Fig. 26 (b). The polarization resistance $R_p$ is defined as the sum of two resistances ($R_2$ and $R_3$). It is obvious that the addition of the ionically conducting phase GDC to the PBSCF cathode results in a significant reduction of non-charge transfer resistance ($R_3$) while $R_2$ is nearly unchanged up to 50 wt% of GDC, which consequently decreases the total polarization resistance ($R_p = R_2 + R_3$). These results might be attributed to the predominant non-charge transfer contribution to the electrode polarization resistance, likely due to the extended electrochemical reaction zone with the addition of GDC into PBSCF, where the reaction rate of the composite electrodes would be the sum of those on the 2PB sites (the surface of MIEC) and those on the TPB sites (all interface boundaries between PBSCF and GDC that are exposed to oxygen gas).[24] This characteristic of the composite cathode could lead to many more ORR sites than those of a single electronic conductor or MIEC. At 60 wt% of GDC, however, a sudden increase in both $R_2$ and $R_3$ is observed due to a reduction of effective electron-conducting paths by the excessive amount of GDC particles.[24] The constant phase element (CPE) represents a non-ideal capacitor and indicates the similarity of the CPE to a true capacitor. The capacitance (C) values of the electrodes are also provided in Table 5 obtained from the following equation (1), where n is an empirical constant. [42-44]:

$$C = \frac{1}{R}(RQ)^{1/n} \qquad (1)$$

Fig. 26 (c) shows an Arrhenius plot of $R_p$ at 600 $^{o}$C for PBSCF-GDC*x*, and the calculated values of activation energy are also shown in the inset of Fig. 26 (c). The specific ASR values of PBSCF-GDC*x* are 0.106, 0.083, 0.057, 0.052, and 0.174 Ω cm$^2$ at 600 $^{o}$C for $x$ = 0, 20, 40, 50, and 60 wt% of GDC, respectively.

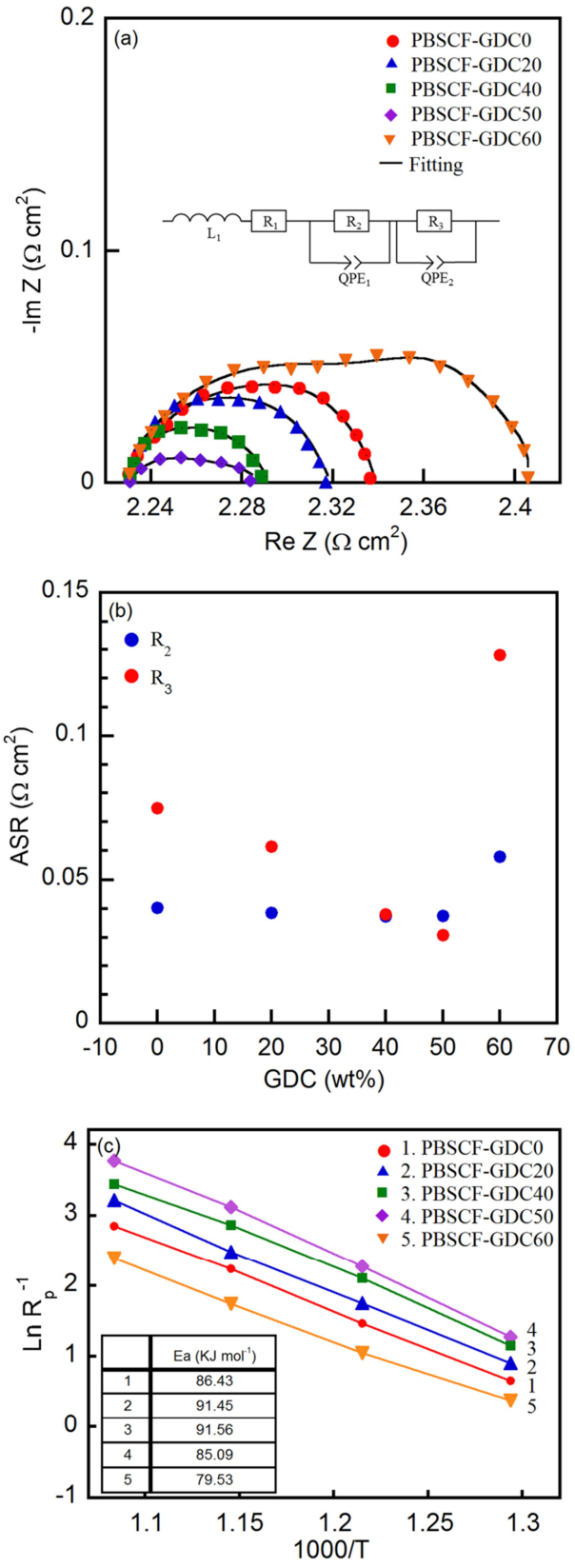


**Fig. 26.** (a) Experimental and simulated impedance plots of $PrBa_{0.5}Sr_{0.5}Co_{1.5}Fe_{0.5}O_{5+\delta}$–GDC*x*/GDC/Ni-GDC by the equivalent circuit shown as an inset. (b) Comparison of $R_2$ and $R_3$ for

$PrBa_{0.5}Sr_{0.55}Co_{1.5}Fe_{0.5}O_{5+\delta}$–GDC*x*/GDC/Ni-GDC. (c) Temperature dependence of polarization resistance for $PrBa_{0.5}Sr_{0.5}Co_{1.5}Fe_{0.5}O_{5+\delta}$-GDC*x* (*x* = 0, 20, 40, 50, and 60 wt%) composite cathodes on GDC electrolyte sintered at 950 °C for 4 h by Arrhenius plots.

**Table 5.** Electrochemical impedance spectroscopy fitting results of $PrBa_{0.5}Sr_{0.5}Co_{1.5}Fe_{0.5}O_{5+\delta}$-GDC*x* measured at 600 °C in air.

| *x* | $R_1$ ($\Omega$ cm$^2$) | $R_2$ ($\Omega$ cm$^2$) | $R_3$ ($\Omega$ cm$^2$) | $R_p$ ($\Omega$ cm$^2$) | $CPE_2$-Q (F cm$^{-2}$) | $CPE_3$-Q (F cm$^{-2}$) | $C_2$ (F cm$^{-2}$) | $C_3$ (F cm$^{-2}$) |
|---|---|---|---|---|---|---|---|---|
| 0 | 2.1052 | 0.0403 | 0.0747 | 0.1150 | $9.88\times10^{-2}$ | $3.70\times10^{-1}$ | $4.38\times10^{-4}$ | $1.37\times10^{-2}$ |
| 20 | 2.2403 | 0.0385 | 0.0613 | 0.0998 | $6.56\times10^{-2}$ | $3.47\times10^{-1}$ | $4.09\times10^{-4}$ | $2.42\times10^{-2}$ |
| 40 | 2.1658 | 0.0379 | 0.0374 | 0.0753 | $8.25\times10^{-2}$ | $5.65\times10^{-1}$ | $2.45\times10^{-4}$ | $8.78\times10^{-3}$ |
| 50 | 2.0605 | 0.0376 | 0.0309 | 0.0685 | $5.21\times10^{-2}$ | $9.40\times10^{-1}$ | $3.94\times10^{-4}$ | $1.89\times10^{-2}$ |
| 60 | 2.3051 | 0.0580 | 0.1280 | 0.1860 | $9.49\times10^{-2}$ | $9.41\times10^{-1}$ | $3.11\times10^{-4}$ | $2.35\times10^{-1}$ |

Fig. 27 presents the power density and voltage as a function of the current density for Ni-GDC/GDC/PBSCF-GDC*x* cells using humidified $H_2$ (3% $H_2O$) as a fuel and static ambient air as an oxidant in a temperature range from 500 to 650 °C. The fuel cell performance increases with increasing amount of GDC in the PBSCF-GDC*x* composite cathode up to *x* = 50 wt%. The maximum power density at 600 °C reaches about 2.0 W cm$^{-2}$at *x* = 50 wt% whereas a sudden drop in performance (~1.3 W cm$^{-2}$) occurs at *x* = 60 wt%. These results can be inferred from the symmetrical cell impedance. As mentioned above, the extended TPB sites obtained by introducing the composite cathode might enhance the ORR activities, which would be a leading factor for the optimal electrochemical performances of PBSCF-GDC50.

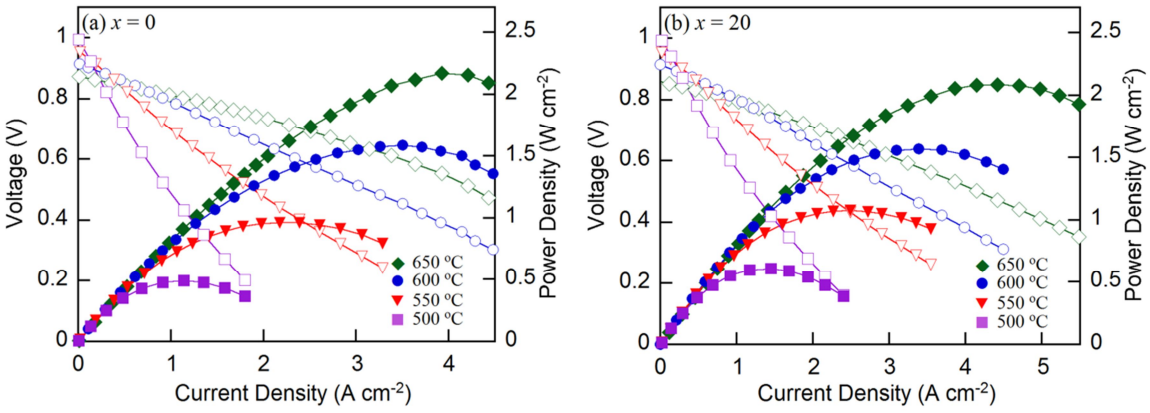

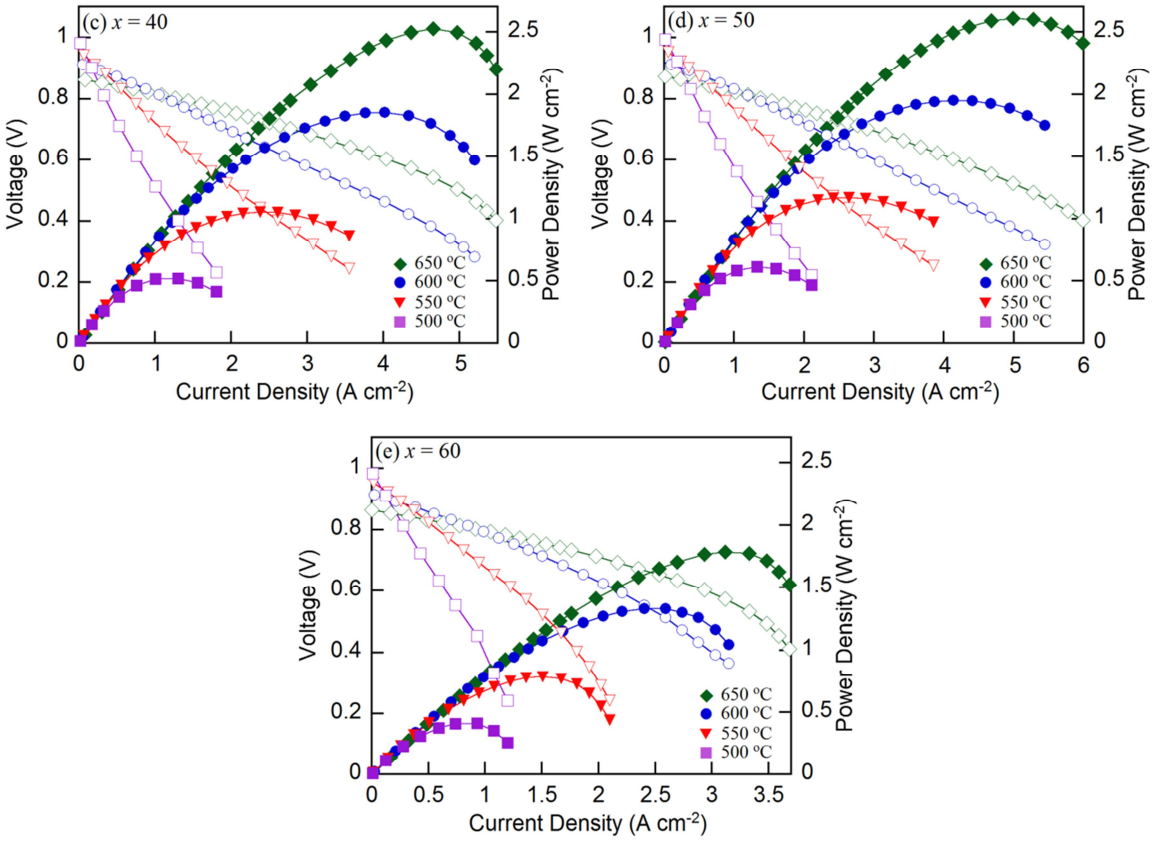


**Fig. 27.** *I-V* curves and corresponding power density curves of a single cell ($PrBa_{0.5}Sr_{0.5}Co_{1.5}Fe_{0.5}O_{5+\delta}$-GDC*x*/GDC/Ni-GDC) under various temperatures: (a) $x$ = 0, (b) $x$ = 20, (c) $x$ = 40, (d) $x$ = 50, and (e) $x$ = 60 wt%.

### 3.3.3. Conclusion

The sintering process is an important parameter that influences microstructure evolution, grain growth, and densification of a material. For PBSCF-GDC50 sample, the optimal sintering temperature with the smallest polarization resistance was revealed to be 950 °C, and is attributed to enhanced micro-structural evolution under the given processing conditions. Different wt% GDC-containing composite cathodes (PBSCF-GDC*x*) were investigated in order to induce the desired properties of a high ORR rate. The performances of PBSCF-GDC*x* composite electrodes in terms of ASR and power density gradually improved with an increasing amount of GDC up to $x$ = 50 wt%. This can be explained by the optimized ORR mechanisms by the addition of the ionically-conducting GDC phase that extends the TPB (all interface boundaries between PBSCF and GDC). At $x$ = 60 wt%, however, the performance of the composite cathode begins to deteriorate due to a reduction of effective electron-conducting paths by the immoderate amount of GDC.

**References**


1. B. C. H. Steele, A. Heinzel, *Nature*, **414** (2001) 345.
2. S. D. Park, J. M. Vohs, R. J. Gorte, *Nature* **404** (2000) 265.
3. N. P. Brandon, S. Skinner, B. C. H. Steele, *Ann. Rev. Mater. Res* **33** (2003) 183.
4. Z. P. Shao, S. M. Haile, J. Ahn, P. D. Ronney, Z. L. Zhan, S. A. Barnett, *Nature* **435**, (2005) 795.
5. A. Lashtabeg, S. J. Skinner, *J. Mater. Chem* **16** (2006) 3161.
6. E. V. Tsipis, V. V. Kharton, *J. Solid State Electrochem.* **12** (2008) 1367.
7. A. Aguadero, L. Fawcett, S. Taub, R. Wooley, K. T. Wu, N, Xu, *J. Mater. Sci.* **47** (2012)3925.
8. J. W. Fergus, *J. Power Sources* **162** (2006) 30.
9. J. Richer, P. Holtappels, T. Graule, T. Nakamura, L. J. Gauckler, *Monatsh. Chem.* **140** (2009) 985.
10. S. H. Park, S .H. Choi, J. Y. Shin, G. Kim, *J. Power Sources* **210** (2012) 172.
11. T. Ishihara, S. Fukui, H. Nishiguchi, Y. Takita, *J. Electrochem. Soc.* **149** (2002) A823.
12. J. H. Kim, M. Cassidy, J. T. S .Irvine, J. Bae, *Chem.Mater*. **22** (2010) 883.
13. S. H. Choi, J. Y. Shin, K. M. Ok, G. Kim, *Electrochim. Acta* **81** (2012) 217.
14. J. M. Ralph, C. Rossignol, R. Kumai, *J. Electrochem. Soc.* **150** (2003) A1518.
15. X. Ding, X. Kong, J. Jiang, C. Cui, L. Guo, *Int. J. Hydrogen Energy* **35** (2010)1742.
16. G. Kim, S. Wang, A. J. Jacobson, L. Reimus, P. Brodersen and C. A. Mims, *J. Mater. Chem.* **17** (2007) 2500.
17. K. Zhang, L. Ge, R. Ran, Z. P. Shao, S. M. Liu, *Acta Materialia* **56** (2008) 4876.
18. A. A. Taskin, A. N. Lavrov, Y. Ando, *Appl. Phys. Lett.* **86** (2005) 091910.
19. J. H. Kim, A. Manthiram, *J. Electrochem. Soc.* **155** (2008) 358.
20. A. J. Jacobson, *Chem. Mater.* **22** (2010) 660.
21. A. Taracon, S. J. Skinner, R. J. Chater, F. Hernandez-Ramirez, J. A. Kilner, *J. Mater. Chem.* **17** (2007) 3175.
22. S. Choi, S. Yoo, J. Kim, S. Park, A. Jun, S. Sengodan, J. Y. Kim, J. Shin, H. Jeong, Y. Choi, M. Liu, G. Kim, *Scientific Reports* **3** (2013) 2426:1.
23. A. R. Jun, J. Y. Kim, J .Y. Shin, G. Kim, *Int. J. Hydrogen Energy* **37** (2012) I8381.
24. J. Y. Kim, W. Y. Seo, J. Y. Shin, M. Liu, G. Kim, *J. Mater. Chem.A* **1** (2013) 515.
25. H. Ding, X. Xue, *Electrochim. Acta* **55** ( 2010) 3812.
26. J. H. Kim, F. Prada, A. Manthiram, *J. Electrochem. Soc.* **155** (2008) B1023.
27. J. H. Kim, M. Cassidy, J. T. S. Irvine, J. M. Bae, *J. Electrochem. Soc.* **156** (2009) B682.
28. S.H. Park, S.H. Choi, J.Y. Kim, J.Y. Shin, G. Kim, *Electrochemistry Letters* **1** (2012) F29-F32.
29. D. S. Tsvetkov, I. L. Ivanov, A. V. Zeuv, *Thermochim. Acta* **519** (2011) 12.
30. S. Choi, J. Shin, G. Kim, *J. Power Sources* **201** (2012) 10.
31. S. H. Jo, P. Muralidhara, D. K. Kim, *Electrochem. Comm.* **11** (2009) 2085.

32. J. Piao, K. Sun, N. Zhang, S. Xu, *J. Power Sources* **175** (2008) 288.
33. C. Zhu, X. Liu, D. Xu, D. Wang, D. Yan, L. Pei, T. Lu, W. Su *J. Power Sources* **185** (2008) 212.
34. C. J. Fu, K. Sun, N. Q. Zhang, X. B. Chen, D. R. Zhou, *Electrochim. Acta* **52** (2007) 4589.
35. C. R. K. Mohan, P. K. Bajpai, *Physica B* **403** (2007) 2173.
36. C. Rossignol, J. M. Ralph, J. M. Bae, J. T. Vaughey, *Solid State Ionics* **175** (2004) 59.
37. A. Mitterdorfer, L. J. Gauckler, *Solid State Ionics* **111** (1998) 185.
38. S. B. Adler, *Chem. Rev* **401** (2004) 4791.
39. Z. Zhan, D. Han, T. Wu, X. Ye, S. Wang, T. Wen, S. Cho, S. A. Barnett, *RSC Adv.* **2** (2012) 4075.
40. S.-H. Park and H.-I.Yoo, *Solid State Ionics* **176** (2005) 1485.
41. J. D. Kim, G. D. Kim, J. W. Moon, Y. Park, W. H. Lee, K. Kobayashi, M. Nagai, C. E. Kim, *Solid State Ionics* **143** (2001) 379.
42. M. J. Esucudero, A. Aguadero, J. A. Alonso, L. Daza, *J. Electroanal. Chem.* **134** (2007) 107.
43. E. Barsoukov, J. R. MacDonald, *Impedance Spectroscopy: Theory, Experiments and Applications*, John Wiley & Sons, Inc., New York (2005) pp 27-128.
44. D. Chen, R. Ran, K. Zhang, J. Wang, Z. Shao, *J. Power Sources* **188** (2009) 96.

### 3.4. Tradeoff optimization of electrochemical performance and thermal expansion for Co-based cathode material for intermediate-temperature solid oxide fuel cells

Layered perovskite oxides have received extensive attention as promising cathode materials because of their faster diffusion coefficient and transport kinetics of oxygen compared to those of $ABO_3$-type perovskite oxides. With the goals of lowering the thermal expansion coefficient (TEC) and maximizing electrochemical properties, this study focuses on the copper (Cu) effect in $PrBa_{0.5}Sr_{0.5}Co_{2-x}Cu_xO_{5+\delta}$ ($x$ = 0, 0.5, and 1.0) layered perovskite oxides by investigating their structural characteristics, electrical properties, and electrochemical performance. The electrical conductivity decreases with increasing Cu content, mainly due to the decreasing amount of $Co^{3+/4+}$. The average TEC values are also identified and the substitution of Cu for Co is beneficial to lower the TEC by suppression of the spin state transitions of $Co^{3+}$ and reduction of $Co^{4+}$. To better understand the thermodynamic behavior of the materials while checking redox stability, coulometric titration experiment is performed. We also investigate the electrochemical performance of $PrBa_{0.5}Sr_{0.5}Co_{2-x}Cu_xO_{5+\delta}$ cathode materials using a Ni-GDC anode-supported cell. All samples show sufficiently high power density around over 1.0 W $cm^{-2}$ at 600 $^oC$.

#### 3.4.1. Introduction

The development of hydrogen technology as an alternative energy source to fossil fuels, with the key benefit of no greenhouse gases or other pollutants, has been accelerated. Solid oxide fuel cells (SOFCs) are among the hydrogen-based electrochemical devices that convert chemical energy to electrical energy directly. Features that make them attractive include their high efficiency, fuel flexibility, and low emission of pollutants stemming from high operating temperature (800 ~ 1000 $^oC$).[1-4] Despite these excellent advantages, conventional high operating temperature gives rise to material compatibility challenges and high costs. These problems have spurred efforts to lower the operating temperature to 500 ~ 800 $^oC$, and intermediate temperature solid oxide fuel cells (IT-SOFCs) have accordingly been introduced. The major obstacles to IT-SOFCs, however, are poor oxide-ion conductivity and inadequate catalytic activity of the conventional cathode.[5-7] Therefore, the development of a new cathode material with high electro-catalytic activity could be a key step toward the commercialization of IT-SOFCs.

In this regard, mixed oxide-ion and electronic conducting (MIEC) oxides containing Mn, Fe, Co, and/or Ni with perovskite structures have been widely investigated as alternative cathode materials. Specifically, cobalt containing oxides, such as $Ba_{0.5}Sr_{0.5}Co_{0.8}Fe_{0.2}O_{3-\delta}$, $Pr_{1-x}Sr_xCoO_3$, $Sm_{0.5}Sr_{0.5}CoO_3$, and $La_{1-x}Sr_xCo_{1-y}Fe_yO_{3-\delta}$ have attracted intense interest due to their high electro-catalytic activity for the oxygen reduction reaction (ORR).[8-11] Recently, many groups have studied layered perovskite oxides, because they offer much higher chemical diffusion and a high

surface exchange coefficient relative to those of $ABO_3$-type perovskite oxides. The layered perovskite oxides can be described with the general formula $AA'B_2O_{5+\delta}$, consisting of sequential layers $[BO_2]$-[AO]-$[BO_2]$-[A′O] stacked along the *c*-axis.[12] This layered structure reduces the oxygen bonding strength in the [AO] layer and provides a disorder-free channel for ion motion, which enhances oxygen diffusivity.[13] On the basis of these advantages, a large volume of work has suggested that the layered perovskite oxide $LnBaCo_2O_{5+\delta}$ (Ln = La, Pr, Nd, Sm, and Gd) could be a potential cathode material for IT-SOFCs.[14-23] Kim meanwhile found that a $PrBaCo_2O_{5+\delta}$ layered perovskite exhibits unusually higher activity for oxygen activation and mobility even at low temperature (300 ~ 500 $^oC$), which result in relatively low area specific resistance of electrodes.[23]

In spite of their excellent properties, cobalt-containing cathodes exhibit high thermal expansion coefficients (TECs) and easy evaporation of cobalt.[24,25] In perovskites, cobalt is predominantly present in the form of $Co^{3+}$cations in low-spin (LS, $t^6_{2g}e^0_g$), intermediate-spin (IS, $t^5_{2g}e^1_g$), and high-spin (HS, $t^4_{2g}e^2_g$) states. At low temperatures, the LS and IS states are more energetically favorable. Raising the temperature, however, may cause LS → IS and IS → HS transitions of $Co^{3+}$ ions, which brings about high TEC values due to the larger ionic radius of HS compared to LS or IS.[26-30] Moreover, the formation of oxide ion vacancies accompanied by reduction of the transition metal ions accounts for high TEC values.[31]

This incompatibility in thermal expansion can cause thermal stress in operating SOFCs and thus result in poor long-term thermal stability. Hence, to optimize cobalt-based cathode systems, partial substitution of the cobalt element with other elements could potentially mitigate these disadvantages while retaining adequate electrochemical activity of the cobalt-containing cathode materials. As a method to lower TECs, Cu-doped $LnBaCo_2O_{5+\delta}$ (Ln=La, Pr, Nd, Sm, and Gd) has been introduced and researchers have reported considerable findings on the effect of Cu doping on the Co site including their thermal expansion behaviors.[32-37] Furthermore, studies on partial substitution for Ba in $LnBaCo_2O_{5+\delta}$ (Ln=La, Pr, Nd, Sm, and Gd) have been conducted with the aim of further enhancing the electrochemical properties.[38,39] For instance, Park et. al. recently reported that partial substitution of the Ba site by Sr in $PrBaCo_2O_{5+\delta}$ layered perovskite oxides can potentially improve the electrical conductivity.[38]

Based on these findings, we present here Cu doped $PrBa_{0.5}Sr_{0.5}Co_2O_{5+\delta}$ with the aims of stabilizing thermal properties and maximizing electrochemical properties. This study focuses on the effects of Cu doping on the structural characteristics, electrical properties, thermodynamic behavior with the redox stability, and electrochemical performances in terms of its application as an IT-SOFC cathode material. The fixed strontium composition of $x = 0.5$ in $PrBa_{1-x}Sr_xCo_2O_{5+\delta}$ has been verified to give optimum performance in our previous work.[38]

### 3.4.2. Results and discussion

Fig. 28 gives the Rietveld refinement data of $PrBa_{0.5}Sr_{0.5}Co_{2-x}Cu_xO_{5+\delta}$ samples for $0 \leq x \leq 1.0$. Each composition is prepared at different temperatures to obtain a single phase, as mentioned in the experimental section. All samples exhibit a single phase and the crystal structure could be indexed with a layered perovskite structure. For $x \leq 0.5$, the XRD patterns reflect a tetragonal structure with the space group *P*4/*mmm* whereas the sample of $x = 1.0$ shows an orthorhombic lattice geometry (space group *Pmmm*). The room-temperature cell volumes are nearly constant at low Cu concentration

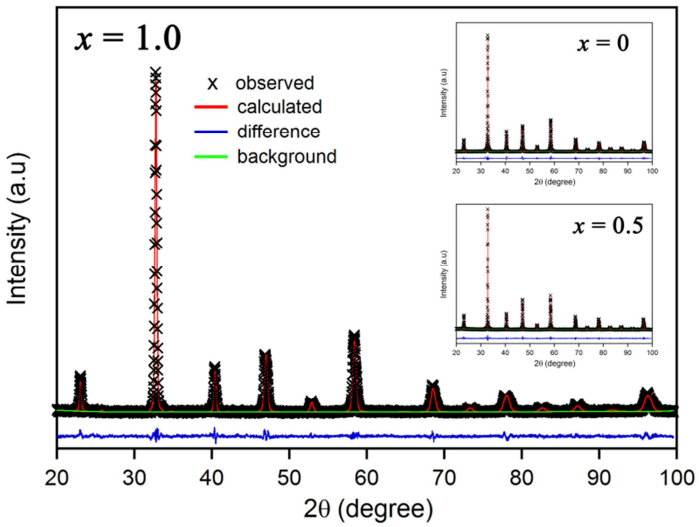


**Fig. 28.** XRD patterns, calculated profiles, peak positions and the differences between observed and calculated profiles for $PrBa_{0.5}Sr_{0.5}Co_{2-x}Cu_xO_{5+\delta}$ ($x$ = 0, 0.5, and 1.0) from 2 θ = 20 to 100 °.

($x$ = 0 and 0.5) but a sudden increase in cell volume is observed at high Cu content ($x$ = 1.0) as listed in Table 6. This could be explained by the predominant existence of $Cu^{2+}$ with higher Cu concentration as follows. In the perovskite-related oxides, Cu can exist simultaneously as the two main valence states of $Cu^{2+}$ and $Cu^{3+}$.[40-43,45] The oxygen content and oxidation state of Co and Cu suggest that Cu may coexist as $Cu^{2+}$ and $Cu^{3+}$ in similar proportions at low Cu concentration while the predominant formation of $Cu^{2+}$ rather than $Cu^{3+}$ overwhelms Cu sites at high Cu content. This predominant presence of $Cu^{2+}$ ions at high Cu concentrations increases the unit cell volume due to the larger size of $Cu^{2+}$ compared to the other ions, as listed in Table 7. It has also been reported, in the $YBaCo_{2-x}Cu_xO_{5+\delta}$ system for example, that copper primarily exhibits a $Cu^{2+}$ valence state with increasing Cu content, which leads to reduced oxygen content while increasing the average Co valence.[41,42]

**Table 6.** Structural parameters and chemical analysis data of $PrBa_{0.5}Sr_{0.5}Co_{2-x}Cu_xO_{5+\delta}$

| $x$ | Space group | a (Å) | b(Å) | c(Å) | V(Å$^3$) | Oxygen content ($5+\delta$) |
|---|---|---|---|---|---|---|
| 0.0 | *P*4/*mmm* | 3.861 | 3.861 | 7.704 | 114.846 | 5.84 |
| 0.5 | *P*4/*mmm* | 3.865 | 3.865 | 7.734 | 115.532 | 5.80 |
| 1.0 | *Pmmm* | 3.879 | 3.881 | 7.805 | 117.499 | 5.62 |

The phase evolution of $PrBa_{0.5}Sr_{0.5}Co_{2-x}Cu_xO_{5+\delta}$ with respect to the temperature is examined based on in situ XRD measurements. Fig. 29 depicts the in situ XRD patterns of $PrBa_{0.5}Sr_{0.5}Co_{2-x}Cu_xO_{5+\delta}$ obtained in the temperature ranges between room temperature and 800 $^oC$ in air. All samples show no chemical or structural changes and are thermodynamically stable under investigated conditions. As expected, unit cell volumes monotonically increase upon increasing temperature as shown in the insets of Fig. 29, even though there are some fluctuations in a/c values. Moreover, the substitutions of Cu for Co increase the distance between B-site cations due to the larger ionic radius of Cu than that of Co as well as enlarge lattice sizes.[41-44]

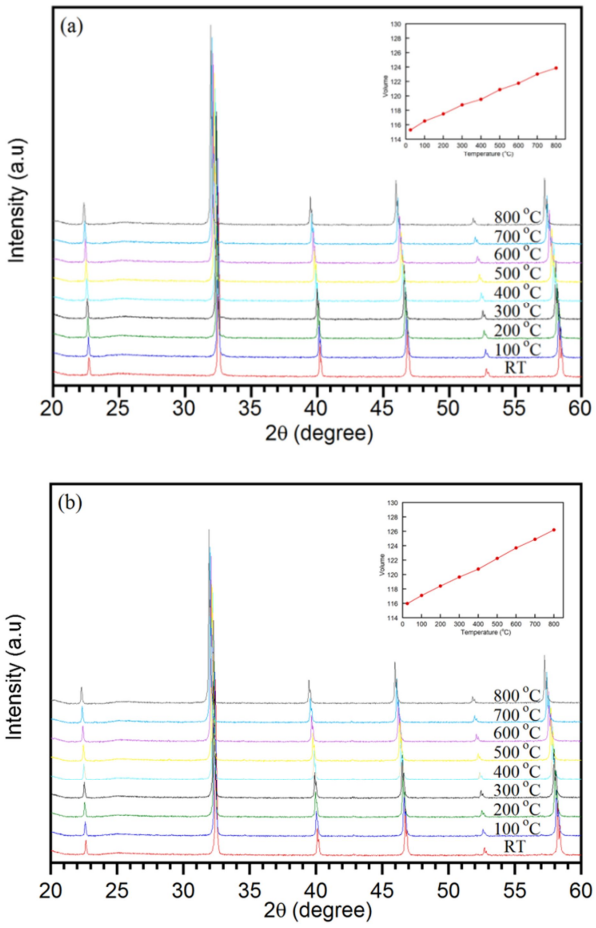

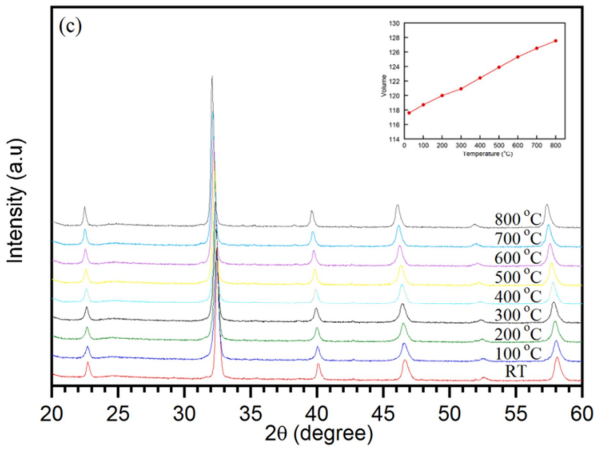


**Fig. 29.** In situ XRD patterns of $PrBa_{0.5}Sr_{0.5}Co_{2-x}Cu_xO_{5+\delta}$ for (a) $x$ = 0, (b) 0.5, and (c) 1.0 in the temperature range between room temperature and 800 °C in air.

**Table 7.** Ionic-radii of the lanthanide, alkaline earth ions, and transition metals.

| Ion | Ionic radius (Å) |
|---|---|
| $Ba^{2+}$ | 1.60 |
| $Sr^{2+}$ | 1.44 |
| $Pr^{3+}$ | 1.30 |
| $Cu^{2+}$ | 0.730 |
| $Cu^{3+}$ | 0.540 |
| $Co^{3+}$ (Low spin) | 0.545 |
| $Co^{3+}$ (High spin) | 0.610 |
| $Co^{4+}$ | 0.530 |

It is also necessary to investigate the chemical compatibility between the $PrBa_{0.5}Sr_{0.5}Co_{2-x}Cu_xO_{5+\delta}$ cathode and GDC electrolyte. Generally, the phase reaction between the electrode and the electrolyte could cause the formation of an undesired insulating layer at the interface, which would block oxide-ionic and electronic transport.[45] The chemical reactivity of the $PrBa_{0.5}Sr_{0.5}Co_{2-x}Cu_xO_{5+\delta}$–GDC is confirmed after calcinations at 1000 °C for 4 h by mixing the corresponding powders in a weight ratio of 6:4, respectively. As indicated in Fig. 30, there are no obvious reactions between $PrBa_{0.5}Sr_{0.5}Co_{2-x}Cu_xO_{5+\delta}$ and GDC upon sintering at 1000 °C, and the patterns verify that all samples obtain a stable layered perovskite structure.

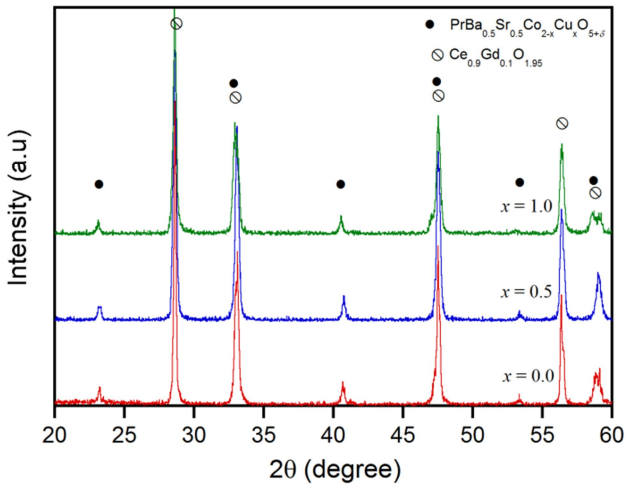


**Fig. 30.** X-ray diffraction patterns of $PrBa_{0.5}Sr_{0.5}Co_{2-x}Cu_xO_{5+\delta}$–GDC ($x$ = 0, 0.5, and 1.0) sintered at 1000 $^{o}$C for 4 h.

SEM images of the $PrBa_{0.5}Sr_{0.5}Co_{2-x}Cu_xO_{5+\delta}$-GDC composite cathodes are illustrated in Fig. 31. As seen in Fig. 31, the dense GDC electrolyte adheres very well to the porous composite cathode layer without cracks, indicating good compatibility between the electrolyte and electrode. All samples show similar micrographs and both the cathode and electrolyte layers are approximately 20 μm in thickness.

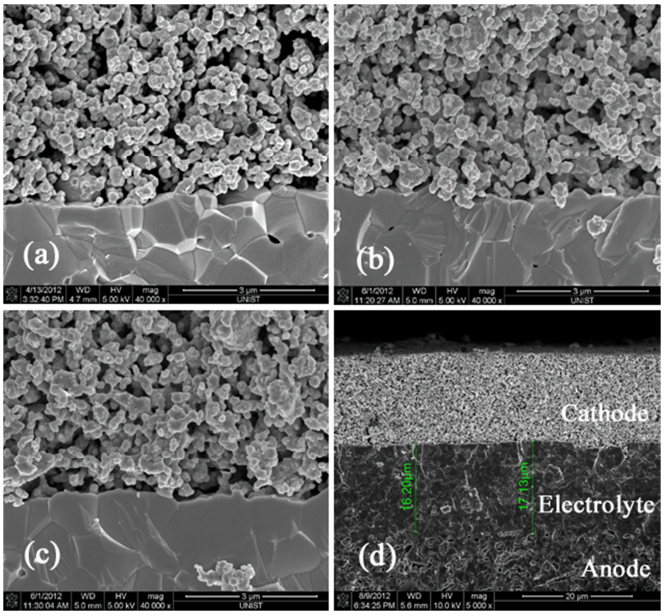


**Fig. 31.** The cross sectional SEM images $PrBa_{0.5}Sr_{0.5}Co_{2-x}Cu_xO_{5+\delta}$–GDC cathodes/GDC electrolyte interface: (a) $x$ = 0, (b) $x$ = 0.5, (c) $x$ = 1.0, and (d) the cross-section of a single cell with approximately 20μm-thick GDC membrane.

Fig. 32 compares the TGA plots of the $PrBa_{0.5}Sr_{0.5}Co_{2-x}Cu_xO_{5+\delta}$ samples recorded from 100 to 800 $^{o}$C in air. All the samples experience weight loss above about 300 $^{o}$C due to the oxygen loss from

the lattice. The oxygen loss decreases with increasing Cu content due to the stronger Cu-O bonds compared to Co-O bonds.[46] A similar trend has also been observed in other reports.[37,46]

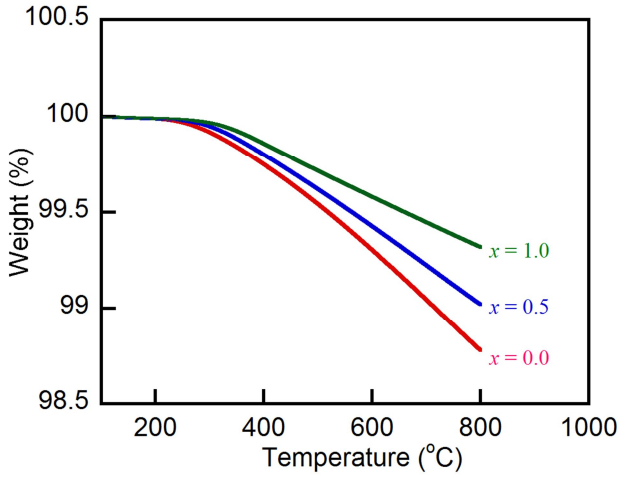


**Fig. 32.** Thermogravimetric analysis of $PrBa_{0.5}Sr_{0.5}Co_{2-x}Cu_xO_{5+\delta}$ ($x$ = 0, 0.5, and 1.0) showing the weigh change (%) as a function of temperature in air.

The thermal expansion behaviors of $PrBa_{0.5}Sr_{0.5}Co_{2-x}Cu_xO_{5+\delta}$ are shown in Fig. 33. The average TEC values at 100 ~ 800 °C decrease with increasing Cu content (inset in Fig. 33). Generally, cobalt is predominantly present in the form of $Co^{3+}$ cations in low-spin (LS, $t^6_{2g}e^0_g$), intermediate-spin (IS, $t^5_{2g}e^1_g$), and high-spin (HS, $t^4_{2g}e^2_g$) states in a perovskite structure. At low temperatures, the LS and IS states are more energetically favorable. Raising the temperature, however, may cause LS → IS and IS → HS transitions of $Co^{3+}$ ions, which brings about high TEC values due to the larger ionic radius of HS compared to LS or IS.[27-30] Furthermore, the reduction of $Co^{4+}$ to $Co^{3+}$ that is caused by a loss of oxygen also leads to high TECs due to the larger ionic size of $Co^{3+}$ relative to that of $Co^{4+}$. Thus, minimizing oxygen loss and decreasing concentration of Co are keys toward stabilizing thermal expansion behavior. In a $PrBa_{0.5}Sr_{0.5}Co_{2-x}Cu_xO_{5+\delta}$ system, however, the oxygen loss with increasing Cu content would be accompanied by the predominant formation of $Cu^{2+}$ rather than the reduction of $Co^{4+}$ ions. Therefore, the substitution of Cu for Co is beneficial to lower the TEC by suppressing the spin state transitions of $Co^{3+}$ and reduction of $Co^{4+}$.

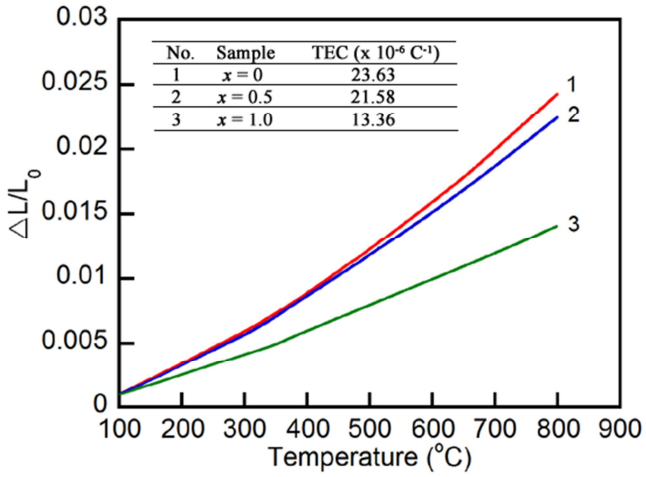


**Fig. 33.** Thermal expansion ($\Delta L/L_0$) curves of the $PrBa_{0.5}Sr_{0.5}Co_{2-x}Cu_xO_{5+\delta}$ ($x$ = 0, 0.5, and 1.0) specimens in the temperature range of 100 ~ 800 °C.

The $pO_2$ dependence of oxygen non-stoichiometry for $PrBa_{0.5}Sr_{0.5}Co_{2-x}Cu_xO_{5+\delta}$ at 700 °C is presented in Fig. 34 (a). All samples show similar shapes of isotherms, implying that they have nearly equivalent reduction mechanisms.[6] As the concentration of Cu increases, the decomposition $pO_2$, at which the oxygen nonstoichiometry changes abruptly and can be assimilated by a vertical line, becomes lower and the isotherms are extended to the left accompanying the increases in oxygen vacancies. For example, the decomposition $pO_2$ of $x$ = 1.0 reaches approximately $10^{-8}$ atm while the sample of $x$ = 0 shows a vertical drop in oxygen content at the decomposition $pO_2$ of about less than $10^{-7}$ atm at 700 °C. This suggests that the Cu rich compound for $x$ = 1.0 shows the higher thermo-chemical stability which can be a key factor to achieve stable electrochemical properties of a cathode material for IT-SOFCs. The $pO_2$ dependence of electrical conductivity for $PrBa_{0.5}Sr_{0.5}Co_{2-x}Cu_xO_{5+\delta}$ at 700 °C is simultaneously measured as shown in Fig. 34 (b). The electrical conductivity of $PrBa_{0.5}Sr_{0.5}Co_{2-x}Cu_xO_{5+\delta}$ increases with $pO_2$, indicating that these materials are a p-type electronic conductor under the given circumstances. All samples provide sufficiently high electrical conductivity in overall ranges of $pO_2$ for IT-SOFC cathode materials. At lower $pO_2$ around $10^{-7}$ ~ $10^{-8}$ atm, however, there is a clear tendency; the dramatic decrease in the electrical conductivity. This demonstrates the close interrelation between the electrical properties and the decomposition of the material, which can be speculated from the oxygen non-stoichiometry in the isotherm data.

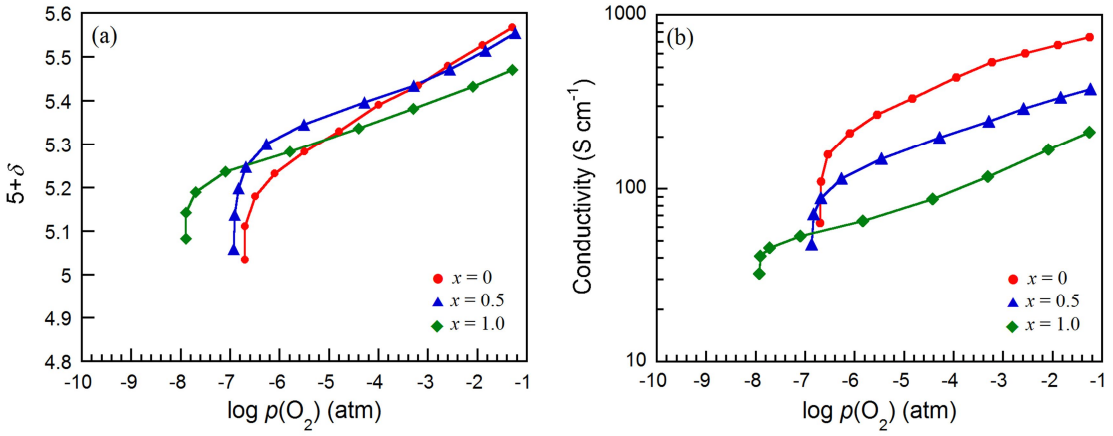


**Fig. 34.** (a) Oxygen non-stoichiometry of $PrBa_{0.5}Sr_{0.5}Co_{2-x}Cu_xO_{5+\delta}$ ($x$ = 0, 0.5, and 1.0) as a function of $pO_2$ at 700 °C. (b) The $pO_2$ dependence of the electrical conductivity of $PrBa_{0.5}Sr_{0.5}Co_{2-x}Cu_xO_{5+\delta}$ ($x$ = 0, 0.5, and 1.0) at 700 °C.

The temperature dependence of electrical conductivity for $PrBa_{0.5}Sr_{0.5}Co_{2-x}Cu_xO_{5+\delta}$ is illustrated in Fig. 39. The electrical conductivity decreases with substitution of Cu for Co at all temperature regions mainly due to decreasing $Co^{3+/4+}$ which is consistent with previous findings.[36,37] A decrease in the electrical conductivity of $PrBa_{0.5}Sr_{0.5}Co_{2-x}Cu_xO_{5+\delta}$ also could be derived from its crystal structure. In the crystal structure of a $PrBa_{0.5}Sr_{0.5}Co_{2-x}Cu_xO_{5+\delta}$ layered perovskite, $Pr^{3+}$ and $Ba^{2+}$ or $Sr^{2+}$ ions occupy alternate layers of the perovskite lattice along the *c*-axis. The oxide ion vacancies are exclusively located in the $Pr^{3+}$ layers due to the smaller size of $Pr^{3+}$ ions compared to those of $Ba^{2+}$ or $Sr^{2+}$ ions, resulting in the formation of $CoO_5$ square pyramids and $CoO_6$ octahedral chains.[19] The increasing concentration of Cu and a consequent change of oxygen content will break this original alternation of $CoO_5$ pyramidal and $CoO_6$ octahedral planes along the *a* and *b* directions, and in turn hampers hole creation (charge carriers).[41] In other words, greater oxygen loss and the demolished alternation of $CoO_5$ pyramidal and $CoO_6$ octahedral planes with increasing Cu content induce the formation of oxygen vacancies and a consequent decrease in charge carriers, which lowers electrical conductivity. The samples with $x$ = 0 and 0.5 exhibit metallic behavior at all measured temperatures while a semi-conducting behavior is observed at $x$ = 1.0 around 500 °C which is possibly attributed to the lattice oxygen loss.[47]

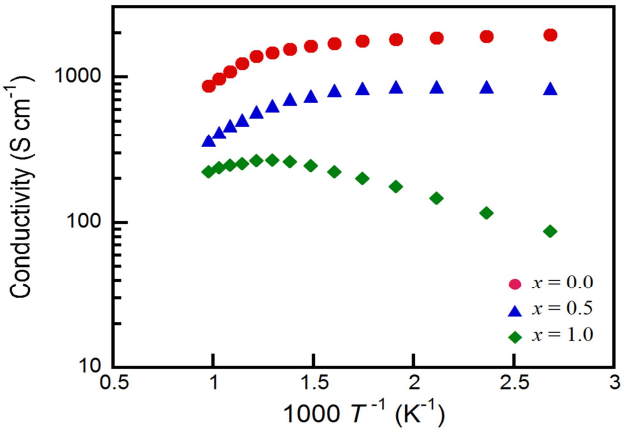


**Fig. 39.** Electrical conductivities of $PrBa_{0.5}Sr_{0.5}Co_{2-x}Cu_xO_{5+\delta}$ ($x$ = 0, 0.5, and 1.0) in air as a function of temperature.

The area specific resistance (ASR) of $PrBa_{0.5}Sr_{0.5}Co_{2-x}Cu_xO_{5+\delta}$ is obtained at 600 °C by AC impedance spectroscopy with $PrBa_{0.5}Sr_{0.5}Co_{2-x}Cu_xO_{5+\delta}$-GDC/GDC/$PrBa_{0.5}Sr_{0.5}Co_{2-x}Cu_xO_{5+\delta}$-GDC symmetrical cells, where the electrolyte has ~1.0 mm thickness. The ASR values are determined by the impedance intercept between high frequency and low frequency with the real axis of the Nyquist plot, and typical impedance spectra are presented as an inset in Fig. 40 (a). The temperature dependence of ASR with the $PrBa_{0.5}Sr_{0.5}Co_{2-x}Cu_xO_{5+\delta}$ ($x$ = 0, 0.5, and 1.0)-GDC composite is illustrated by an Arrhenius plot in Fig. 40 (b). The specific ASR values are 0.093, 0.106, and 0.124 Ω cm$^2$ at 600 °C for $x$ = 0, 0.5, and 1.0, respectively. These results give reasonable explanation to the electrochemical performance data in Fig. 40. The apparent activation energy values are evaluated as 107, 119, and 136 kJ mol$^{-1}$ for $x$ = 0, 0.5, and 1.0, respectively.

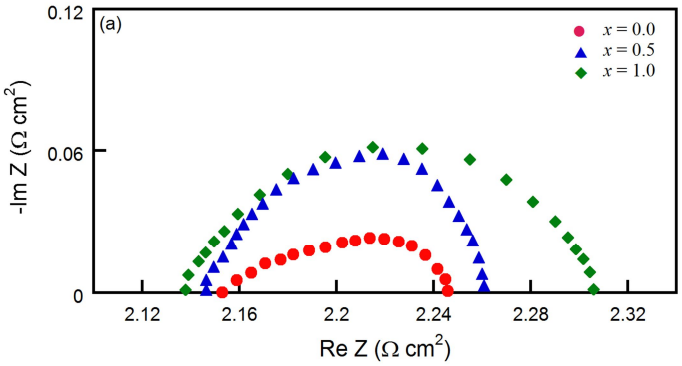

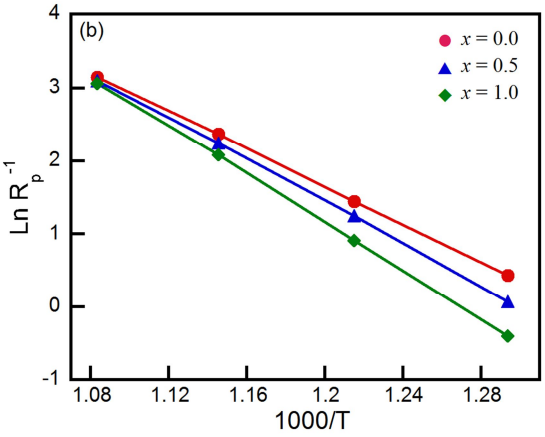


**Fig. 40.** (a) Impedance spectra of $PrBa_{0.5}Sr_{0.5}Co_{2-x}Cu_xO_{5+\delta}$ ($x$ = 0, 0.5, and 1.0)-GDC composite cathodes on GDC symmetrical cells measured at 600 °C under OCV condition. (b) Temperature dependence of the $PrBa_{0.5}Sr_{0.5}Co_{2-x}Cu_xO_{5+\delta}$ ($x$ = 0, 0.5, and 1.0)-GDC composite cathodes polarization conductance by Arrhenius plots.

Fig. 41 represents the power density and voltage as a function of the current density for Ni-GDC/GDC/$PrBa_{0.5}Sr_{0.5}Co_{2-x}Cu_xO_{5+\delta}$-GDC cells using humidified $H_2$ (3% $H_2O$) as a fuel and static ambient air as an oxidant in a temperature range from 500 to 650 °C. The fuel cell performance decreases with increasing Cu content in $PrBa_{0.5}Sr_{0.5}Co_{2-x}Cu_xO_{5+\delta}$, consistent with the trend of enhanced ASR and electrical conductivity. The maximum power density reaches 1.22 W $cm^{-2}$ for $x$ = 0 at 600 °C. The Cu-doped $PrBa_{0.5}Sr_{0.5}Co_2O_{5+\delta}$ samples also achieve good performance of 1.10 and 0.96 W $cm^{-2}$ for $x$ = 0.5 and 1.0 at 600 °C, respectively, representing substantially high performance. Therefore, Cu-doped $PrBa_{0.5}Sr_{0.5}Co_2O_{5+\delta}$ can be considered sufficiently acceptable as an IT-SOFC cathode material in terms of thermal behaviors and electrochemical performances of the materials.

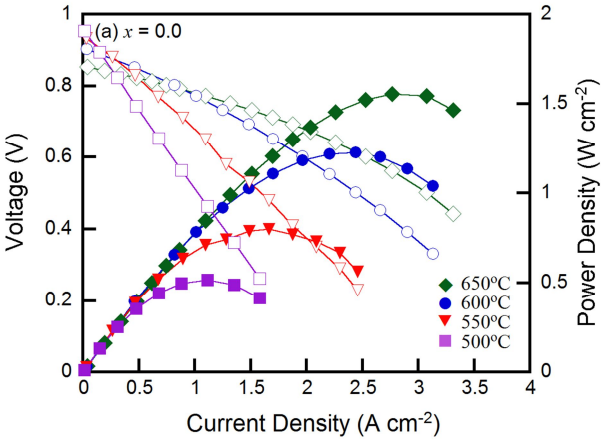

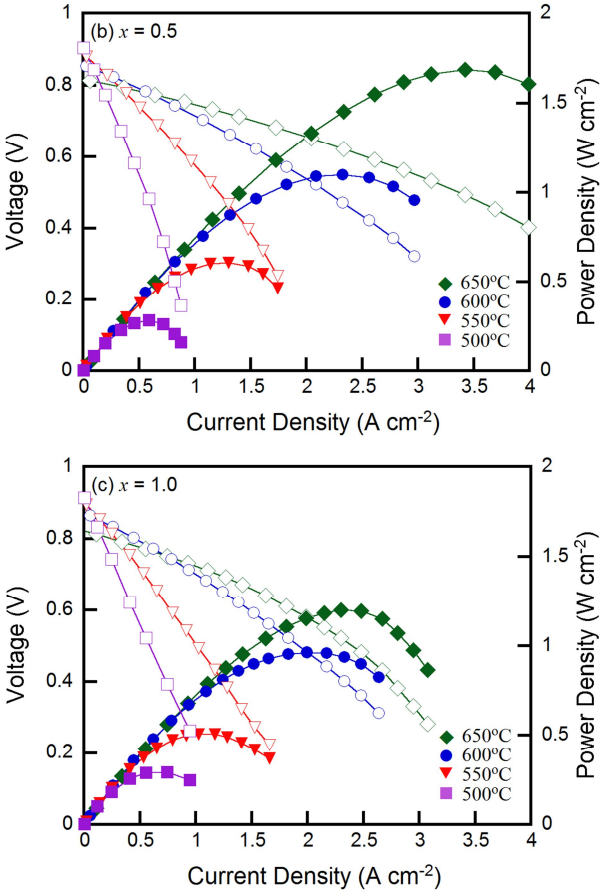


**Fig. 41.** *I-V* curves and corresponding power density curves of a single cell ($PrBa_{0.5}Sr_{0.5}Co_{2-x}Cu_xO_{5+\delta}$-GDC /GDC/Ni-GDC) under various temperatures: (a) $x = 0$, (b) $x = 0.5$, and (c) $x = 1.0$.

### 3.4.3. Conclusion

The effects of partial substitution of Cu for Co in $PrBa_{0.5}Sr_{0.5}Co_2O_{5+\delta}$ layered perovskite oxide on structural characteristics, thermal expansion, electrical conductivity, electrochemical properties, and thermodynamic behavior are investigated. The in situ XRD spectra recorded from room temperature to 800 °C demonstrate that all samples show no structural changes and are thermodynamically stable under investigated conditions. The temperature dependence of the electrical conductivity for $PrBa_{0.5}Sr_{0.5}Co_{2-x}Cu_xO_{5+\delta}$ ($x = 0$, 0.5, and 1.0) reaches the general required value of a cathode material. The TEC values decrease with the substitution of Cu for Co by suppression of the spin state transitions of $Co^{3+}$ and reduction of $Co^{4+}$ which would be beneficial for a long-term stability. Although Cu-doped samples show a slight degradation in electrochemical performances, they are almost comparable to or slightly lower than that of Co-rich compound. Moreover, the isotherms of $PrBa_{0.5}Sr_{0.5}Co_{2-x}Cu_xO_{5+\delta}$ ($x = 0$, 0.5, and 1.0) obtained from the coulometric titration experiment reveal the higher redox stability at lower $pO_2$ with the higher amount of Cu doping. The achieved

power density and reduced TEC demonstrate that the tradeoff optimization could be obtained by introducing adequate substitution of Cu for Co in cobalt-based cathodes for IT-SOFCs.

**References**


1. B. C. H. Steele, A. Heinzel, *Nature* **414** (2001) 345.
2. S. D. Park, J. M. Vohs, R. J. Gorte, *Nature* **404** (2000) 265.
3. N. P. Brandon, S. Skinner, B. C. H Steele, *Ann. Rev. Mater Res.* **33** (2003) 183.
4. Z. P. Shao, S. M. Haile, J. Ahn, P. D. Ronney, Z. L. Zhan, S.A. Barnett, *Nature* **435** (2005) 795.
5. A. J. Jacobson, *Chem. Mater.* **22** (2010) 660.
6. S. Yoo, T. H. Lim, J. Y. Shin, G. Kim, *J. Power Sources* **226** (2013) 1.
7. Y. Y. Huang, J. M. Bohs, R. J. Gorte, *J. Electrochem. Soc.* **151** (2004) A646.
8. S. Park, S. H. Choi, J. Y. Shin, G. Kim, *J. Power Sources* **210** (2012) 172.
9. T. Ishihara, S. Fukui, H.Nishiguchi, Y.Takita, *J. Electrochem. Soc.* **149** (2002) A823.
10. J. H. Kim, M. Cassidy, J. T. S. Irvine, J. Bae, *Chem. Mater.* **22** (2010) 883.
11. S. H. Choi, J. Y. Shin, K. M. Ok, G. Kim, *Electrochim. Acta* **81** (2012) 217.
12. D .J. Chen, R. Ran, K. Zhang, J. Wang, Z. P. Shao, *J. Power Sources* **188** (2009) 96.
13. A. A.Taskin, A. N. Lavrov, Y. Ando, *Progress in Solid State Chemistry* **35** (2007) 481.
14. A. M. Chang, S. J. Skinner, J. A. Kilner, *Solid State Ionics* **177** (2006) 2009.
15. S. H. Choi, J. Y. Shin, G. Kim, *J. Power Sources* **201** (2012) 10.
16. J. Y. Kim, W. Y. Seo, J. Y. Shin, M. Liu, G. Kim, *J. Mater. Chem. A* **1** (2013) 515.
17. A. Tarancon, A. Morata, G. Dezanneau, S.J. Skinner, J.A. Kilner, S. Estrade, F.H. Ramirez, F. Peiro, J.R. Morante, *J. Power Sources* **174** (2007) 255.
18. N. Li, Z. Li, B. Wei, X. Q. Huang, K.F. Chen, Y. H. Zhang, W. H. Su, *J. Alloys Compd.* **454** (2008) 274.
19. J. H. Kim, A. Manthiram, *J. Electrochem. Soc.* **155 (4)** (2008) B385.
20. B. Lin, S. Zhang, L. Zhang, L. Bi, H. Ding, X. Liu, J. Gao, G. Meng, *J. Power Sources* **177** (2008) 330.
21. Q. Zhou, T. He, Y. Ji, *J. Power Sources* **185** (2008) 754.
22. K. Zhang, L. Ge, R. Ran, Z. Shao, S. Liu, *Acta Materialia* **56** (2008) 4876.
23. G. Kim, S. Wang, A. J. Jacobson, L. Reimus, P. Brodersen, C.A. Mims, *J. Mater. Chem.* **17** (2007) 2500.
24. H. H. Wang, C. Tablet, A. Feldhoff, J. Caro, *Adv. Mater* **17** (2005) 1785.
25. O. Yamamoto, Y. Takeda, R. Kanno, N. Noda, *Solid State Ionics* **22** (1987) 241.
26. L. Ruiz-Gonzalez, K. Boulahya, M. Parras et al, *Chemistry-A European Journal* **8** (2002) 5694.
27. I. O. Troyanchuk, N. V. Kasper, D. D. Khalyavin, H. Szymczak, R. Szymczak, M. Baran, *Phys. Rev. B: Condensed Matter and Materials Physics* **58** (1998) 2418.
28. M. A. Senaris-Rodriguez, J. B. Goodenough, *J. Sold State Chemistry* **118** (1995) 323.
29. K. Huang, H.Y. Lee, J.B. Goodenough, *J. Electrochem. Soc.* **145** (1998) 3220.

30. L. W. Tai, M. M. Nasrallah, H. U. Anderson, D. M. Sparlin, S. R. Sehlin, *Solid State Ionics* **76** (1995) 259.
31. M. Mori, N.M. Sammes, *Solid State Ionics* **146** (2002) 301.
32. Q. Zhou, Y. Zhang, Y. Shen, T. He, *J. Electrochem. Soc.* **157** (2010) B628.
33. Q. Zhou, Y. Li, Y. Shi, X, Zhang, T. Wei, S. Guo, D. Huang, *Mater. Res. Bull.* **47** (2012) 101.
34. Q, Nian, L. Zaho, B. He, B. Lin. R. Peng, G. Meng, X. Liu, *J. Alloys Compd.* **492** (2010) 291.
35. S. Lu, G. Long, Y. Ji, X, Meng, H. Zhao, C. Sun, *J. Alloys Compd.* **509** (2011) 2824.
36. L. Zhao, Q. Nian, B. He, B. Lin, H. Ding, S. Wang, R. Peng, G. Meng, X. Liu, *J. Power Sources* **195** (2010) 453.
37. Y. N. Kim, A. Manthiram, *J. Electrochem. Soc.* **158** (2011) B276.
38. S. Park, S. H. Choi, J. Y. Kim, J. Y. Shin, G. Kim, *ECS Electrochemistry Letters* **1** (2012) F29.
39. A. R. Jun, J. Y. Kim, J. Y. Shin, G. Kim, *Int. J. Hydrogen Energy* **37** (2012) I8381.
40. S. Yoo, J. Y. Shin, G. Kim, *J. Mater. Chem.* **21** (2011) 439.
41. X. Zhang, H. Hao, X. Hu, *Physica B: Condensed Matter (Amsterdam, Netherlands)* **403** (2008) 3406.
42. L. Barbey, N. Nguyen, V. Caignaert, F. Studer, B. Raveau, *J. Solid State Chemistry* **112** (1994) 148.
43. W. I. F. David, W. T. A. Harrison, J. M. F. Gunn, O. Moze, A. K. Soper, P. Day, J. D. Jorgensen, D. G. Hinks, M. A. Beno, L. Soderholm, I. D. W. Capone, I. K. Schuller, C. U. Segre, K. Zhang, J. D. Grace, *Nature* **327** (1987) 310.
44. H. Steinfink, J. S. Swinnea, Z. T. Sui, H. M. Hsu, J. B. Goodenough, *J. Am. Chem. Soc.* **109** (1987) 3348.
45. C. Rossignol, J. M. Ralph, J.M. Bae, J. T. Vaughey, *Solid State Ionics* **175** (2004) 59.
46. K. T. Lee, A. Manthiram, *Solid State Ionics* **178** (2007) 995.
47. Y. S. Wang, H. W. Nie, S. R. Wang, T. L. Wen, U. Guth, V. Valshook, *Materials Letters* **60** (2006) 1174.

# Acknowledgements

Completion of this master dissertation was possible with the support of several people. I would like to express my sincere gratitude to all of them.

I would like to gratefully and sincerely appreciate my advisor, Prof. Guntae Kim, for his valuable guidance, scholarly inputs, and consistent encouragement I received throughout the research work during my graduate school at UNIST. He has always made himself available to clarify my doubts despite his busy schedules and I consider it as a great opportunity to do my master program under his guidance and to learn from his research expertise. Thank you, Sir for all your help and support.

I am also grateful to the members of my committee, Prof. Soojin Park and Prof. Jin Young Kim. I was so inspired from their insightful comments and hard questions based on their expertise and theoretical basics and learned the topic of electrochemistry relevant to my research field, solid oxide fuel cell (SOFC).

I thank Prof. Jeeyoung Shin for his academic support and encouragements when facing difficulties. His guidance helped me in all the time of the research and writing of the papers.

I'd like to express my thanks to the lab members of GUNS LAB, Seonyoung Yoo, Sivaprakashi Sengodan, Sihyuk Choi, Areum Jun, Junyoung Kim, Seona Kim, and Ohoon Kwon, for their many helps during my studies. I wish to thank in particular Sihyuk who opened the way for me to complete my graduate studies. His insights and comments were invaluable and stimulated my desire to achieve better results over the years, and I look forward to a continuing collaboration with him in the future.

Last but not the least, I would like to thank my family, my parents, for giving birth to me at the first place and supporting me spiritually throughout my life. They instilled in me confidence and a drive for pursuing my M. S. D.

# List of publications

1. **Seonhye Park**, Sihyuk Choi, Jeeyoung Shin, Guntae Kim* "Tradeoff optimization of electrochemical performance and thermal expansion for Co-based cathode material for IT-SOFCs" ***Electrochimica Acta*** Submitted.
2. **Seonhye Park**, Sihyuk Choi, Jeeyoung Shin, Guntae Kim* "A collaborative study of sintering and composite effects for $PrBa_{0.5}Sr_{0.5}Co_{1.5}Fe_{0.5}O_{5+\delta}$ IT-SOFC cathode" ***RSC Advances*** 4 (2014) 1775.
3. Jiyoun Kim, Sihyuk Choi, **Seonhye Park**, Changmin Kim, Jeeyoung Shin,Guntae Kim*"Effect of Mn on the electrochemical properties of a layered perovskite $NdBa_{0.5}Sr_{0.5}Co_{2-x}Mn_xO_{5+\delta}$ ($x$ = 0, 0.25, and 0.5) for intermediate-temperature solid oxide fuel cells" ***Electrochimica Acta*** 112 (2013) 712.
4. Sihyuk Choi, Seonyoung Yoo, Jiyoun Kim, **Seonhye Park**, Areum Jun, Sivaprakash Sengodan, Junyoung Kim, Jeeyoung Shin, Hu Young Jeong, Yong Man Choi, Guntae Kim*, Meilin Liu* "Highly efficient and robust cathode materials for low-temperature solid oxide fuel cells: $PrBa_{0.5}Sr_{0.5}Co_{2-x}Fe_xO_{5+\delta}$" ***Scientific Reports*** 3 (2013) 2426.
5. Sihyuk Choi, **Seonhye Park**, Junyoung Kim, Tak-Hyoung Lim, Jeeyoung Shin, Guntae Kim* "Electrochemical Properties of an Ordered Perovskite $LaBaCo_2O_{5+\delta}$-$Ce_{0.9}Gd_{0.1}O_{2-\delta}$Composite Cathode with Strontium Doping for Intermediate-Temperature Solid Oxide Fuel Cells" ***Electrochemistry Communications*** 34 (2013) 5.
6. **Seonhye Park**, Sihyuk Choi, Junyoung Kim, Jeeyoung Shin, Guntae Kim* "Strontium Doping Effect on High-Performance $PrBa_{1-x}Sr_xCo_2O_{5+\delta}$ as a Cathode Material for IT-SOFCs" ***ECS Electrochemistry Letters*** 1 (2012) F29.
7. **Seonhye Park**, Sihyuk Choi, Jeeyoung Shin, Guntae Kim* "Electrochemical investigation of strontium doping effect on high performance $Pr_{1-x}Sr_xCoO_{3-\delta}$ ($x$ = 0.1, 0.3, 0.5, and 0.7) cathode for intermediate-temperature solid oxide fuel cells" ***Journal of Power sources*** 210 (2012) 172.